Experimental study on the flow boiling critical heat flux of narrow channels heat sinks for power electronics

Hugo Alejandro Pozo Saravia

Scuola di ingegneria industriale e dell'informazione
Politecnico di Milano

A thesis submitted for the degree of
Master of Science in Energy Engineering
Milan 2022

Experimental study on the flow boiling critical heat flux of narrow channels heat sinks for power electronics

Master thesis
Submitted on March 31th, 2021
at

POLITECNICO DI MILANO

For the master's degree in Energy Engineering

By
Hugo Alejandro Pozo Saravia

Student ID: 927127
Academic year: 2020-2021

Supervisors:

Professor Luigi Pietro Maria Colombo, (POLIMI) main supervisor
Associate Professor Wiebke Brix Markussen (DTU), external main supervisor
Senior Researcher Martin Ryhl Kærn (DTU), external co-supervisor

POLITECNICO
MILANO 1863

To my family,
Though I couldn’t see you when I wrote this,
you were on every page.

Psalm 139:9-12

Abstract

The present need for innovative and sustainable solutions in the current energy transition caused the continuous miniaturization of electronic components and the need for more energy-efficient solutions for the thermal management of power electronics. Flow boiling of refrigerants in microscale channels has gained increasing attention as a long-term solution over the conventional single-phase cooling systems to effectively meet the high heat flux demand in new power electronics. The experimental study investigated narrow and high aspect ratio multi-microchannels that were micromachined in copper with thin separating walls during saturated flow boiling of refrigerants. Three different test samples with different sidewalls – straight, sinusoidal wavy, and diverging – were manufactured with 25 channels, each with 200 µm wide, 1200 µm high, and 200 µm separating walls, and in the case of the diverging test sample, the separating walls were 200 µm wide at the inlet and 60 µm wide at the outlet of the channels. The total footprint area of the samples was 1 cm^2 and the equivalent diameter ranged between 338 to 343 µm. The investigation adopted a low-GWP fluid (R1234yf) and the conventional R134a. The measurements resulted in a large data bank with 216 data points covering a wide range of mass flux between 320 kg/m^{2}s to 1200 kg/m^{2}s, at different inlet subcooling, and the saturation temperature was 30 °C and 40 °C. An infrared camera was employed with a resolution of 221 x 221 pixels and high-speed visualization was used to support the investigation with flow pattern analysis and verify the absence of relevant flow instabilities.

The investigation presents a comparative analysis of the flow boiling in microchannels with geometries that can increase the critical heat flux with low pressure drop and support the future development of thermal management systems. The highest footprint critical heat flux was 852.1 W/cm^2 which was notoriously higher compared to previous investigations in the literature. In general, the critical heat flux with the wavy sidewall was consistently higher than the other test samples, while the diverging channels presented the lowest pressure drop. The effect of mass flux and saturation temperature is demonstrated according to the literature. However, inconsistencies are found in the effect of subcooling which is evident in the straight and the diverging channels, while it was negligible in the sinusoidal wavy which was attributed to the high mixing and secondary flows in corrugated walls. The sinusoidal wavy wall enhanced the critical heat flux up to 60% because of the continuous development of the liquid layer which delays dryout, while the diverging channel design reduced the pressure drop up to 80% due to the gradient pressure at its inlet. Lastly, the statistical comparison showed a mean average percent error below 20% for some of the correlations, however, they did not capture completely the observed critical heat flux.

Keywords: Critical heat flux, Microchannels Flow boiling, Electronics cooling

Sommario

La necessità di soluzioni innovative e sostenibili nell'attuale transizione energetica impone la continua miniaturizzazione dei componenti elettronici e la necessità di soluzioni più efficienti dal punto di vista energetico per la gestione termica dell'elettronica di potenza. I flussi bifase di refrigeranti in microcanali hanno guadagnato una crescente attenzione come soluzione a lungo termine rispetto ai tradizionali sistemi di raffreddamento monofase per soddisfare efficacemente la necessità di raffreddamento della nuova elettronica di potenza. Questo studio sperimentale ha considerato microcanali soggetti a flussi bifase di refrigeranti. Sono stati prodotti tre diversi sezioni di prova con pareti laterali diversamente conformati – piana, ondulata sinusoidalmente e divergente con un totale di 25 canali, ciascuno con larghezza di 200 µm e profondità di 1200 µm, e nel caso del campione di prova con pareti divergenti, le pareti divisorie erano 200 µm di larghezza all'ingresso e 60 µm all'uscita dei canali. L'area di base totale dei canali è di 1 cm^2 e il diametro equivalente varia tra 338 e 343 µm. Lo studio ha riguardato un fluido a basso GWP (R1234yf) accando al convenzionale R134a. Le misurazioni hanno prodotto una vasta banca dati di 216 punti dati che coprono un'ampia gamma di flussi di massa tra 320 kg/m^{2}s e 1200 kg/m^{2}s, a diversi gradi di sottoraffreddamento in ingresso, e due livelli di temperatura di saturazione: 30 °C e 40 °C. È stata usata anche una termocamera con una risoluzione di 221 pixel × 221 pixel come ausilio alla visualizzazione del flusso bifase per verificare l'assenza di instabilità.

Lo studio presenta un'analisi comparativa sui flussi bifase in microcanali con geometrie in grado di aumentare il flusso termico critico pur in presenza di limitate cadute di pressione e così supportare lo sviluppo futuro dei sistemi di smaltimento della potenza termica. Il flusso termico critico più alto è stato di 852,1 W/cm2, valore notevolmente superiore rispetto alle precedenti indagini in letteratura. In generale, il flusso termico critico con la parete laterale ondulata è risultato costantemente maggiore rispetto agli altri campioni di prova, mentre i canali divergenti hanno presentato la caduta di pressione più bassa. L'effetto del flusso di massa e della temperatura di saturazione è stato trovato conforme alla letteratura. Tuttavia, si riscontrano incongruenze nell'effetto del sottoraffreddamento, che è evidente nei canali piani e divergenti mentre è risultato trascurabile negli ondulati sinusoidali. Questo particolare comportamento potrebbe attribuirsi all'elevata miscelazione e ai flussi secondari nelle pareti ondulate. I microcanali con parete ondulata sinusoidalmente hanno mostrato un incremento del valore del flusso termico critico fino al 60% a causa del continuo sviluppo dello strato liquido che ritarda il dryout, mentre l'effetto dell'allargamento della sezione di passaggio nei canali divergenti ha contribuito a ridurre la caduta di pressione fino all'80%. Infine, il confronto statistico ha mostrato un errore percentuale medio inferiore al 20% per alcune delle correlazioni presenti nella letteratura corrente, le quali, tuttavia, non sono in grado di predire correttamente il valore del flusso termico critico.

Parole chiave: Flusso termico critico, flusso bifase in microcanali, Raffreddamento di dispositivi elettronici

Acknowledgments

Being an international student is an incredible experience that comes with different and very difficult challenges, but also with life-changing events that surely will endure during my entire life. This thesis was the result of the support of many people, and although some contributions may have seemed small to some of them, they were invaluable to me.

I owe my supervisors Luigi Colombo, Wiebke Brix Markussen, and Martin Ryhl Kærn a debt of gratitude for their support, guidance, and encouragement during all stages of the project. I thank you for allowing me to develop this project and be welcomed at DTU. Without their indispensable help, this work could not have been possible. Thank you for this life-changing experience.

I am grateful to Professor Luigi Colombo for his incredibly constant availability and the enormous encouragement that I received during the entire project. His help and guidance, and his words of support were truly invaluable. Thank you for your kind support and encouragement.

I am grateful to Professor Wiebke Brix Markussen for letting me have the opportunity to develop this project. I am thankful for her support, encouragement, guidance, and help to quickly start the project at DTU. Thank you for your remarkable charisma and ability to listen and help.

I am grateful to Martin Ryhl Kærn for his relentless help, great enthusiasm, and amazing collaboration during the entire project. I enormously enjoyed every discussion that shaped this thesis. Thank you for providing a stimulating atmosphere filled with enthusiasm and for your inspiring friendship.

I am especially thankful to Gennaro Criscuolo, who originally presented this project to me and encouraged me to follow it. Certainly, this was an unexpected experience that would change my life. Thank you for your support and the best pandoro I had during my stay in Denmark.

I want to thank my friends in Denmark and Italy, for the enjoyable moments and laughs we shared. In particular, I want to thank Giulia and Pietro for their intermittent company at the office, and the free coffee during my stay at DTU. I am also most grateful to the staff of the Thermal Energy Section of DTU for creating a pleasant work environment and for their aid with this project's needs.

I want to thank my loving family whom I miss. For your constant support, your encouragement, and your love. I am thankful for having you in my life, and for every single moment that I spent with you which is precious to me. Finally, I want to thank my wife, Suellen, for her support and understanding even in the most stressful moments of this thesis. Looking back on our lives, the unbelievable is that, despite all things, we still managed to meet at the perfect moment. Thank you for your kindness and for bringing me so much joy. I feel the love of God for me through you.

Contents

Nomenclature

Abbreviations

CAD	Computer-Aided Design
CHF	Critical Heat Flux
CNC	Computer Numerical Control
GWP	Global Warming Potential
LED	Light Emitting Diode
PEEK	PolyEtherEtherKetone
px	Pixels
ROI	Region Of Interest
RTD	Resistance Thermal Detector

Greer letters

Δh_{fg}	Enthalpy of vaporization
Δp	Pressure drop
Δp_{diff}	Pressure drop measured by the differential pressure transducer
ΔT	Temperature drop
ΔT_{H-A}	Average temperature difference between the ambient and the microheater
δ	Flow area variation
η	Fin efficiency parameter
η_{ave}	Fin efficiency with average width
ρ_l	Density of liquid phase
ρ_v	Density of vapor phase
ρ	Density
σ	Surface tension or standard deviation

Latin Letters

$\dot{m}$	Refrigerant mass flow rate
$\dot{Q}_{amb}$	Heat rate lost to the ambient
Q_{fp}	Heat rate at footprint of channels
$\overline{W}$	The average width of channels
A_{fp}	Channel footprint area
D_h	Hydraulic diameter
DT_{cal}	Calibration adjustment for the thermal map
g	Gravitational acceleration
H_{ch}	Height of the channels
h_{corr}	Flow-wise heat transfer coefficient predicted by the correlation
h_{loc}	Flow-wise local heat transfer coefficient
h_{tc}	Average heat transfer coefficient
h	Enthalpy
I	Microheater current
k	Thermal conductivity
L_{ch}	Length of the channels
L_{fin}	Length of the fin
m_{ave}	Fin parameter with an average width
m_{mean}	Fin parameter with mean fin parameter
m_i	Discretized fin parameter
m	Fin parameter
N	Number of channels
n	Number of variables or generic exponent
p	Pressure
q_{av}	Average heat flux on the heated perimeter
q_{fp}	Heat flux at the channel footprint
q_w	Heat flux at the channel wall
Re	Reynolds number
ss	Type A uncertainty
T_h	Temperature of the heater
T_{sat}	Saturation temperature
T_w	Temperature at the channel wall
T	Temperature
t	Thickness of layer
u	Uncertainty
V	Microheater voltage
v	Velocity
W	Width of channels
W_i	The average width of the discretized channel

1

Introduction

1.1. MOTIVATION

The current awareness in an increasingly warming world has paved the way for innovative and sustainable solutions in the current energy transition. According to the US National Aeronautics and Space Administration, 2020 was the hottest year on record [15] with the average global temperature around 1.3 °C higher than in the last decades. With the growing demand for electrification and the market penetration of renewable energy, the increasing demand for high-density power electronics has become a firm manifest of where the world is heading to. Power electronics is a core component of many strategic technologies for the sustainable development of our society, such as wind turbines and electric vehicles. Current targets in carbon neutrality together with new energy policies, call for highly efficient solutions. The energy efficiency, weight, and reliability of the power electronics systems are of utmost importance to minimize the impact on the available energy of the vehicle on EVs. The demand for higher installed electricity capacity has made offshore wind farms operate in the deep sea with floating foundations, where high voltage direct current HVDC converter stations rely on high-reliability and high-density power electronics. Heat flux dissipation of these systems has been increasing over the years making the thermal management of power electronics a fundamental subject.

Flow boiling of refrigerants in microscale channels has gained increasing attention as a long-term solution over the conventional single-phase cooling systems to effectively meet the high heat flux demand in new power electronics. Compared to the conventional single-phase cooling systems, cooling by flow boiling in microchannels utilizes the latent heat of vaporization, leading to significantly higher heat transfer during boiling. The miniaturization of channels conceives a large surface-area-to-volume ratio of microchannel geometries requiring a smaller flow rate and limited pressure drop. Subsequently, the potential for reduction of the pumping power is one of the most promising features of flow boiling in microchannels, which directly leads to the reduction in energy consumption of thermal management systems. Additionally, flow boiling in microchannels results in uniform wall temperatures, reducing the thermal gradients and decreasing the thermo-mechanical stresses of the cooled components leading to higher reliability and longer life cycles. In this context, the critical heat flux (CHF) becomes arguably the most important limit in the design of two-phase flow cooling systems. Understanding the limit of heat flux under which a thermal management system can operate instigates the decrease in risk of failures, i.e., burnout in engineering applications. However, the current prediction of the critical heat flux (CHF) presents significant scientific challenges that arise due to the several inconsistencies in current research between different authors. With the growing interest in the design of flow boiling heat sinks, better prediction methods are required to meet the high heat flux demand while keeping high reliability during operating conditions under safe limits. Consequently, the endeavor to develop comprehensive characterizations of the complex channel interactions, conjugate effects, and instabilities is needed.

1.2. OBJECTIVES OF THE STUDY

The present thesis aims to contribute to the general discussion on CHF in microchannels and the effects of the main parameters of interest in flow boiling by using saturated flow boiling of refrigerants in narrow high aspect ratio microchannels with thin separating walls, and different wall geometries. The investigation hypothesizes is that CHF in narrow channels can achieve high CHF, and alternative wall geometries can delay the CHF and decrease the pressure drop. To confirm the hypothesis, three different microchannels test samples were manufactured in copper with 25 channels, each with 200 µm wide, 1200 µm high, and 200 µm separating walls, and in the case of the diverging test sample, the separating walls were 200 µm wide at the inlet and 60 µm wide at the outlet of the channels. The total footprint area of the samples was 1 cm^2 and the equivalent diameter ranged between 338 to 343 µm. The scope of the investigation extends to the comparative analysis of CHF experimental results with and without inlet restrictions, and the general description of the effect of the main parameters of interest in CHF in microchannels. The novelty of the present study consisted in performing a comparative analysis of the CHF effect by different wall geometries, such as diverging and sinusoidal wavy channel designs compared to the conventional straight channels. The investigation adopted a low-GWP fluid (R1234yf) and the conventional R134a serving as a benchmark to contribute to the general discussion on its phase-out and replacement with low-GWP alternatives. Lastly, an evaluation of the current prediction methods was performed with the experimental points obtained during the test runs. The measurements were supported with IR thermal maps and high-speed image visualization. The objectives of the thesis were formulated as follows:

- Document experimental data on the critical heat flux (CHF) of R1234yf and R134a in three narrow channel heat sinks with different geometries at several mass fluxes, inlet subcooling, and two saturation temperatures.
- Perform a comparative analysis on the critical heat flux (CHF) with and without inlet restrictions (orifices) with the test samples.
- Study the effect of the main operating parameters (mass flux, inlet subcooling, saturation temperature, fluid) on the critical heat flux (CHF).
- Provide a comparative analysis of the effect of different wall geometries (diverging, sinusoidal wavy, straight channels) on the wall critical heat flux.
- Assess the applicability of existing empirical methods for the prediction of the critical heat flux in the investigated narrow and high aspect ratio channels with low-GWP refrigerant R1234yf and R134a.

1.3. THESIS OUTLINE

The thesis presents 7 chapters and 1 appendix. The content is as follows:

- Chapter 1: is the introduction which contains the motivation of the research work, the hypothesis, and the main objectives of the thesis.
- Chapter 2: contains a description of the two-phase flow in microchannel and the critical heat flux considerations found in literature concerning conventional straight channels, and alternative geometries such as diverging and sinusoidal wavy. The chapter also reports the research questions addressed by the thesis.
- Chapter 3: describes the experimental methods employed for the investigation. The description includes the test rig, the test sections, and the test samples.
- Chapter 4: describes the methods employed in the data reduction and the uncertainty evaluation. The chapter also contains the experimental methodology.
- Chapter 5: presents the experimental results of the investigation and the discussion of the results.
- Chapter 6: contains an assessment of the prediction accuracy of CHF correlations from the literature.
- Chapter 7: presents the conclusion of the study and recommendations for future works.

2

Background

2.1. CRITICAL HEAT FLUX

The growing importance of high-density power electronics and the demand for sustainable cooling systems in modern microelectronics applications present flow-boiling in microchannels as a long-term solution with great potential to meet the maximum heat flux targets with minimum pressure losses. Critical heat flux (CHF) is indisputable the most relevant limit in the design of such cooling systems, as the high-heat flux targets need to be met while the temperature of the material is excluded from the risk of *burnout*. As is well known, the critical heat flux is the maximum heat flux achievable before a severe increase of the heated surface temperature caused by a heavy deterioration of the heat transfer. Compared to the conventional single-phase cooling systems, flow boiling in microchannels presents the main three advantages: (1) the latent heat of vaporization leading to very high heat transfer during boiling, (2) the large surface area to volume ratio of microchannel geometries, and (3) smaller flow rate and more uniform wall temperature [23],[21]. CHF occurs in subcooled or saturated conditions, and two basic mechanisms of thermal crisis are commonly associated with the two cases. Subcooled CHF occurs when the thermodynamic vapor quality is lower than zero (x_{out} < 0) and the bulk temperature is subcooled at the outlet of the channels. The subcooled CHF mechanism is associated with the liquid replenishment that is hindered by the vapor formation during nucleate boiling (departure from nucleate boiling, DNB), and generally arises at very high mass velocities and short lengths compared to the hydraulic diameter. In saturated CHF, the flow boiling vapor quality is higher than zero (x_{out} > 0) at the outlet of the channels. For the case of saturated flow boiling, the large increase in void fraction triggers annular flow in the channels, where the dryout of the liquid film is the main CHF mechanism [26],[23]. Flow instabilities are inherently present in two-phase microchannels due to the relationship between heat transfer, pressure drop, and vapor generation and they present a major interest in investigations on CHF. In the case of microchannels, a considerable number of observations concerning flow instability present the description of upstream compressible volume instability, excursive instability, or parallel channel instability [39],[5]. Particularly, parallel channel interaction often leads to vapor backflow which can be identified by the presence of vapor bubbles in the inlet plenum. The vapor presence inhibits the incoming liquid flow from replenishing the thin liquid film layer [17]. Therefore, in the presence of instabilities or vapor backflow, the critical heat flux may be triggered earlier, a phenomenon referred to as premature critical heat flux PCHF, due to a premature drying of the heat transfer surfaces [5],[23]. Because the CHF in these conditions is lower than the one obtained in stable boiling flow, understanding how to avoid such instabilities is of utmost importance in the design of microchannels [29]. These instabilities are generally more evident at low mass fluxes when the momentum of the bulk liquid flow entering the channel may be comparable to the force of the disturbance generated by the pressure build-up during nucleation [5], and at low inlet subcooling, and they may be suppressed using upstream throttling valve, and especially inlet flows restrictions at the microchannel inlet like orifices [23],[39],[5]. Nonetheless, comparative studies on CHF with and without inlet restrictions are scarce.

The investigations concerning saturated CHF in multi-microchannels that are aligned with the scope of the thesis are summarized in Table 2.1. The investigations in single-channel CHF and using water as the working fluid have been omitted since water presents the risk of freeze in cooling applications of power electronics, and single channels flow instability differs from those that arise in multi-microchannels. The studies summarized cover shallow ($H_{ch}/W_{ch} < 1$) and narrow ($H_{ch}/W_{ch} > 1$) rectangular multi-channels, as well as investigations on diverging and wavy wall design. The operational conditions cover a large range of saturation temperatures, mass fluxes, and inlet subcooling and the heated equivalent diameters (based on 3-sided heating for the rectangular channels) range from 22 µm to 2. mm with most values below 1 mm. The heated length ranges from 10 mm to 120 mm and results in length-to-diameter ratios from 12 to 345, with most values concentrated in the range from 10 to 60. The working fluids reported include a single Fluorinert electronic coolant, ethanol, acetone, and several refrigerants where some of which were phased out or are planned to be phased out in the coming years due to their high global warming potential (GWP) or Ozone Depletion Potential (ODP). The maximum CHF at the footprint level is presented as well, and in the investigations where only the CHF at the channel walls was reported, the maximum footprint CHF has been obtained by assuming a fin efficiency of 0.9 and marked with an asterisk "$*$". Most of the investigations in Table 2.1. did not always attempt to achieve high CHF, as pointed out by Park and Thome [32] nonetheless, it is important to point out that the maximum footprint CHF in these studies is only partly covering current targets for power electronics in electric vehicles.

2.2. EFFECT OF MAIN PARAMETERS

The CHF in microchannels is affected by several parameters regarding the channel geometry and fluid conditions. As far as the fluid condition is concerned, the mass velocity, the saturation temperature, the inlet subcooling, and fluid properties are some of the parameters of major interest. The observations indicate that the increase of mass flux consistently increases the CHF. However, some inconsistencies are found in the subcooling effect. The CHF either increases or is unaffected by the level of inlet subcooling. Bowers and Mudawar [6] attributed the independence of inlet subcooling to the short distance of the subcooled region in their heated section. Later, Qu and Mudawar [36] observed similar independence in their multi-channel experiments with water. They attributed the independence of inlet subcooling to the instability present in parallel channels, where regardless of how subcooled the inlet liquid was, the periodic vapor backflow into the inlet plenum mixed with the incoming liquid flow bringing it close to the saturation temperature. However, even in single microchannel CHF investigations adopting an upstream stabilizing valve, the inlet subcooling was found to be independent [48],[31],[45]. Park and Thome [32] found the inlet subcooling effect to be moderate for their larger diameter multi-channels, while for their smaller diameter channels it was negligible. Mauro et al. [29] found that when using the same smaller diameter channels and adopting a liquid supply split system that reduced the heated length to half, increasing subcooling did have an increasing effect on the CHF for refrigerant R134a and R236fa, but no effect was observed for R245fa. In a recent study by Kærn et al. [19], the subcooling effect on the CHF was evident, especially at large mass fluxes for his narrow channels with short heated-length and inlet restriction to stabilize the flow. The presented results could suggest that the inlet subcooling effect on the CHF is highly related to the flow instabilities in multi-channels, the channel size, the heated length, and the fluid. Some of the main conclusions regarding the effect of these parameters are also included in Table 2.1.

Similarly, some inconsistencies are found in the literature concerning the effects of saturation temperature on the CHF. The increase in saturation temperature could either increase or decrease the CHF depending on the fluid and the reduced pressure. Koşar and Peles [24] observed increasing and decreasing trends in a wide range of saturation temperatures, indicating the presence of a peak CHF. Park and Thome [32] found increasing and decreasing trends for their larger diameter channels and their smaller diameter channels, respectively, however, these effects were described as insignificant. Dalkılıç et al. [12] found a decrease in CHF with increasing saturation temperature, while Agostini et al. [2] and Mastrullo et al. [28] found an insignificant effect or a slightly increasing and decreasing trend. Mauro and Thome [29] found that the saturation effect was significant with R134a and R236fa, but R245fa showed no effect at all. The increasing and decreasing trend is commonly explained by the counteracting effects of the refrigerant properties with increasing saturation temperature. On one hand, the increased vapor to liquid density ratio ρ_v/ρ_l tends to stabilize the liquid film during annular flow leading to an increase in the CHF. On the other hand, the latent heat of vaporization Δh_{gf} reduces the CHF achievable, and the surface tension σ decreases as well increasing the susceptibleness of the liquid film to be torn apart [28].

Concerning the geometric parameters, it is difficult to make a direct comparison regarding the CHF in multi-channels since most studies involve only a single test sample, and the wall thickness and channel number in the samples employed varies among different authors. Most studies evince the CHF dependence on the heated equivalent diameter and the heated length. Bowers and Mudawar [6] and Park and Thome [32], indicate that the channel wall CHF increases with an increasing diameter at constant mass flux. Contrary to this, Hong et al. [17] found a decrease in the wall CHF with his shallow (H_{ch}/W_{ch} < 1) microchannel test samples when the diameter was increased. The effect of the heated length was demonstrated by Mauro et al. [29], who examined the same small diameter samples results of Park and Thome [32] with a liquid supply split system. Mauro et al. [29] report a CHF increase of up to 80% on the footprint CHF. This is also consistent with Wojtan et al. [48] findings in their single-channel CHF investigations, which indicate an increase in the CHF with decreasing heated length. Concerning the length-to-diameter ratio, the CHF typically decreases with increasing length-to-diameter ratio, which was also found at low mass fluxes in the investigation by Mastrullo et al. [28]. However, at higher mass fluxes their results indicated the opposite trend. Although the previous findings could expose the effects of diameter and heated length on the CHF, comparative investigations of different wall geometry, such as expanding and sinusoidal wavy walls, are scarce and the effect on the CHF of new microchannel geometries are not established.

2.3. FLOW BOILING IN DIVERGING MICROCHANNELS

As an alternative to the conventional straight channels, investigation of other alternatives such as diverging channels indicated a promising reduction of flow instability in microchannels. Prajapati et al. [33] demonstrated that flow instability can be suppressed significantly for flow boiling in microchannels with a diverging wall design. They attributed the stabilization of the flow to the steep pressure gradient near the inlet in the diverging microchannel that resists the vapor backflow, thus stabilizing the two-phase flow. Wang et al. [47] found that the use of microchannels with diverging cross-sections could suppress the reversed flow enhancing the heat transfer performance and yielding stable flow. They attributed the flow reversal avoidance due to the faster purging bubbles out of the channels achieving a stable two-phase flow and delaying the CHF. Balasubramanian et al. [4] conducted an experimental investigation of flow boiling heat transfer in both straight and expanding microchannels. They demonstrated that expanding microchannels could significantly reduce the lower pressure drop by up to 30% due to the stabilizing effect of the channels. The above findings could suggest that the stabilizing effect of the two-phase flow, may not only enhance the heat transfer in the diverging microchannels but the stabilizing effect could be extended to the CHF increase. A study by Fu et. Al [16] demonstrated that the CHF was higher with their diverging channels compared to the conventional straight ones, especially at low mass fluxes. They attributed the higher CHF to the diverging design that enhances the flow stability. Comparative studies on the CHF between diverging and straight channels are limited, while investigations on LGWP refrigerants for cooling systems in power electronics are currently inexistent.

2.4. FLOW BOILING IN SINUSOIDAL WAVY MICROCHANNELS

Another alternative to the conventional straight microchannel is the sinusoidal corrugated design. Although there is vast literature regarding single-phase heat transfer in wavy microchannels, flow boiling heat transfer was studied until a certain extent and studies concerning CHF is particularly limited. Concerning single-phase flow, Sui and Lee [43] found that compared with straight baseline microchannels, the heat transfer performance of their wavy microchannels was superior with smaller pressure drop penalty. Later, Sui and Teo. [44] demonstrated an increase in heat transfer performance with their two novel wavy microchannel designs. The above suggested that it is reasonable to extend the heat transfer enhancement to flow boiling as well. Later, Wan et al. [46] found that the bottom half-corrugated structure could store more liquid for evaporation and bubble nucleation, which contributes to heat transfer enhancement. In a recent study, Xia et al. [51] obtained significantly high CHF with their test samples, reaching values of 601 W/cm^2 with wavy channels. There is a significant absence of experimental data on flow boiling in wavy microchannels and there is vast room for observations to understand the enhancement mechanism that result in high CHF.

Table 2.1. Main parameters, conditions, and effects observed in multi-microchannel saturated CHF studies.

Author	Geometry					Fluids	Conditions				Effects
	$\mathrm{N} \times (\mathrm{W_{ch}} \times \mathrm{H_{ch}})$ [μm]	$\mathrm{L_h}$ [mm]	D_{he} [μm]	$\frac{L_h}{D_{he}}$ [−]	$\frac{H_{ch}}{W_{ch}}$ [−]		T_{sat}	G	ΔT_{sub}	$q_{fp,max}$	
Kuan, Kandlikar [20]	6 x (1054 x 157)	63.5	484	131.2	0.15	R-123	42-55	411-534	24-38	16.4*	CHF↑ with G
Koşar, Peles [24]	5 x (200 x 264)	100	344	344.7	1.32	R-123	52-82	291-1118	29-59	196	CHF↑ with G and ΔT_{sc} CHF↑↓ with T_{sat}
Agostini et al. [2]	67 x (223 x 680)	20	52	52.2	3.0	R236fa	20-34	276-992	0-15	250	CHF→ with ΔT_{sc}, T_{sat}
Park, Thome [32]	20 x (467 x 4052)	20	22	22.6	8.7	R245fa, R236fa	10-50	90-450	0-24	342	CHF↑ with G and ΔT_{sc} CHF→ with T_{sat}
	29 x (199 x 756)	20	56	56.9	3.8	R134a	15-40	200-4000	0-15	215	CHF↑ with G CHF → with ΔT_{sc}, T_{sat}
Mauro et al. [29]	29 x (199 x 756)	10	28	28.4	3.8	R245fa, R236fa R134a	15-40	250-1500	5-25	330	CHF↑ with G, ΔT_{sc}** CHF↓ with T_{sat} **
Chen. Garimella [8]	60 x (100 x 389)	12.7	177	71.7	3.9	FC-77	97	254-1015	26	107	CHF↑ with G
Mastrullo et al. [28]	7 x (2000 x 500)	25	2000	12-17	0.5	R134a	25-76	146-1504	0-18	175*	CHF↑ with G
	7 x (2000 x 400)	35	1333	26.3	0.25	R1234ze(E), R1234yf, R32	25-76	146-1504	0-18	169*	CHF → with T_{sat} ***
Hong et al. [17]	4 x (2000 x 400)	100	1143	87.5	0.2	Ethanol	56-78	3-39	29-44	68	CHF↓↑with L_h/D_{he}***
	4 x (1500 x 400)	100	857	116.7	0.2	Acetone	20-28	5-70	29-44	90	
Dalkiliç et al. [12]	4 x (1500 x 300)	40	543	73.6	1.23	R134a	57	1000		71	CHF↑ with G CHF↓ with x_{in}, T_{sat}
Kærn et al. [19]	25 x (198 x 1167)	10	365	27.4	5.89	R134a, R1234yf	30-40	333-1260	(1.3-	678	CHF↑ with G, ΔT_{sc}
	17 x (293 x 1176)	10	521	19.2	4.01	R1234ze(E)			14.7)		CHF↓ with T_{sat}
Fu et al. [16]	6 x (300 x 300)	20	400	50	0.45	HFE-7100	61	39-180		114	CHF↑ with G
	6 x (300 x 4000)	20	1120	17.8	6.06						CHF↑ with *diverging*
Xia et al. [51]	16 x (128 x 80)	120	98	12.2	0.626	Acetone	56	251-423	26	601	CHF↑ with G CHF↑ with *wavy*

∗ maximum footprint CHF ($q_{fp,max}$) calculated by assuming 0.9 fin efficiency ↑ increase

∗∗ no effect for R245fa → no effect

∗∗∗ CHF decreased with T_{sat} for R134a ↓ decrease

2.5. SUMMARY AND PROBLEM STATEMENT

Power electronics is a core component of many technologies strategic to the sustainable development of our society, such as wind turbines and electric vehicles. Heat flux dissipation of these systems has been increasing over the years and flow boiling of refrigerants in microscale channels has gained increasing attention as an attractive alternative to liquid cooling. To present, comparative investigation of the CHF with alternative microchannel geometries to the conventional straight channels is scarce and the investigation of physical phenomena related to CHF in microchannels is not yet fully established. The investigation aims to contribute to the general discussion on CHF in microchannels and the effects of the main parameters of interest in flow boiling by using saturated flow boiling of refrigerants in narrow high aspect ratio microchannels with thin separating walls, and different wall geometries. The investigation is coupled with IR camera visualization and high-speed flow videos to support the measurements with information concerning the flow instability in the channels. The effect of the wall geometry of wavy, diverging, and straight channels was investigated, while parametric analysis on the CHF was used to demonstrate the effect of saturation temperature, inlet subcooling, and fluid properties. The investigation covers a wide range of mass fluxes, and a comparative analysis of the CHF with and without inlet restrictions, i.e., orifices at the inlet of the channels. According to the points highlighted in the literature review, the following questions are addressed through the thesis:

- Question 1: what are the critical heat flux (CHF) characteristics in micro-milled sinusoidal, expanding, and straight multi-microchannels copper heat sinks in flow boiling with R1234yf and R135a?

- Question 2: What is the relationship between the measured critical heat flux (CHF) and the mass flux, the saturation temperature, and inlet subcooling with R134a and R1234yf?

- Question 3: How the wall geometry (diverging design, sinusoidal wavy design, conventional straight design) affects the wall CHF?

- Question 4: What are the prediction capabilities of existing literature correlations on the critical heat flux CHF in microchannels?

3

Experimental Setup

A detailed description of the experimental setup is presented in the present chapter. The experimental facility employed in the elaboration of this investigation was built and designed at the Department of Mechanical Engineering of the Technical University of Denmark as a project carried out in collaboration with KTH Stockholm, TU Kiel, Danfoss Silicon Power, and Danfoss Drivers [14].

The content of this chapter is based on the content published in" Experimental Characterization of the Heat Transfer in Multi-Microchannel Heat Sinks for Two-Phase Cooling of Power Electronics" [11] and the Ph.D. Thesis "Two-phase cooling of power electronics. An investigation on flow boiling of refrigerants in narrow channels" [10].

3.1. FLOW CONDITIONING LOOP

The refrigerant loop consists of the components to regulate the saturation temperature in the test section, the mass flux in the channels, and the inlet sub-cooling before entering the inlet plenum of the heat sink, hence the main circuit of the experimental setup was dedicated to methodically controlling the main parameters of interest in the present investigation. A schematic of the flow conditioning loop of the experimental test facility is illustrated in Fig. 1. A cylindrical receiver, two plate heat exchangers, a gear pump, a needle valve, and an electric pre-heater were the main components of the flow conditioning loop. The refrigerant was accumulated in the cylindrical receiver and later went through a plate heat exchanger (sub-cooler) until a slight level of subcooling was obtained. Afterward, the liquid refrigerant pressure was increased through the Tuthill gear pump that generated the flow in the loop, and later, the high-pressure liquid refrigerant was balanced with the needle valve. Finally, the electric pre-heater raised the inlet temperature of the refrigerant before entering the test section. After boiling occurs in the test section, the two-phase flow is condensed in the second heat plate exchanger (condenser) and collected back to the receiver. Two filters were installed in the conditioning loop, a 7 µm filter before the inlet plenum of the test section, and a dry filter before the gear pump. In addition, two sight glasses were mounted to visually verify the state of the flow along the loop. As part of the measuring instruments positioned in the loop, a Micro Motion Coriolis Elite sensor (CMFS010M) measured the mass flow rate. Type-T thermocouples by Omega Engineering and Danfoss AKS33 pressure transmitters measured the temperature and pressure at several locations in the experimental setup. Likewise, the thermocouples were calibrated in a thermal bath using a Standard Platinum Resistance by Rosemount, while the pressure transducers were calibrated by an Air-Operated dead weights tester by Budenberg. All signals were collected by data acquisition modules by National Instrument and the temperature set-points, and the heating power supply was monitored and controlled in a customized Labview interface. The regulation of saturation pressure was controlled by the internal coil mounted inside the receiver, which was capable of cooling and heating the water fed by the auxiliary loop. A three-way valve allowed the cooling, while a heating wire wrapped around the piping connected to a thyristor power controller allowed the heating of the water fed to the receiver inner coil, consequently controlling the pressure of the system. The control and regulation of the mass flux were done by manually adjusting the motor speed of the pump using a variable frequency speed drive. Then, the desired level of inlet subcooling was controlled by regulating the electric pre-heater power supply. The instruments range and the uncertainties based on the 95% confidence interval are presented in Table 3.2.

Table 3.2. Instruments range and uncertainties based on the 95% confidence interval

Instrument	u	**Units**	**Range**
Thermocouples, T-type	± 0.15	°C	18 – 50
Thermocouples, K-type	± 0.16	°C	18 – 50
RTDS	± 0.09	°C	25 – 160
Pressure sensor, low range	± 0.025	Bar	0 – 10
Pressure sensor, high range	± 0.04	Bar	0 – 21
Mass flow meter	± 0.1%	kg/h	5 –55
Power supply	± 0.1%	W	0 – 1500

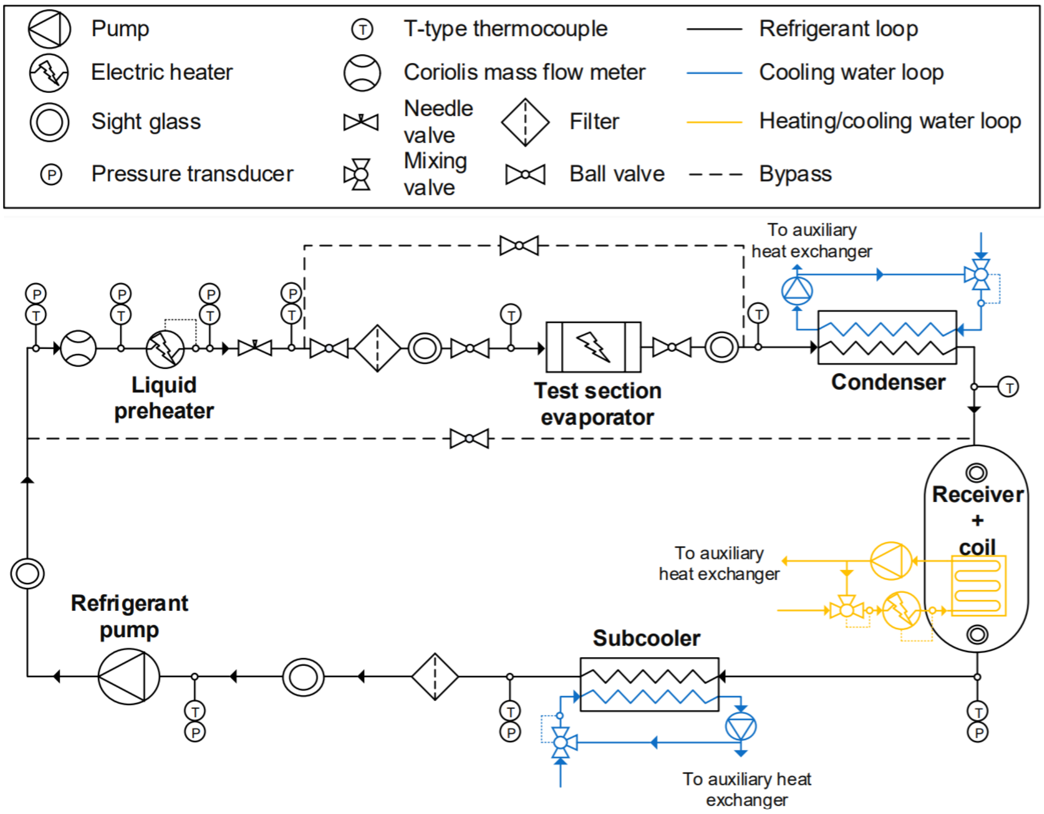

Fig. 1. Schematic of the refrigerant flow conditioning loop of the test rig.

3.2. THE AUXLIARY WATER LOOP

The auxiliary water loop that was used to cool down the refrigerant inside the condenser, the sub-cooler, and the receiver, was operated at a constant mass flow rate. Each one of the three auxiliary loops comprised a pump, an electric heater, a mixing valve, and air release valves. Therefore, the temperature set-points in the condenser, sub-cooler, and receiver were obtained by a mixing valve that controlled the heat exchange with the refrigerant. The auxiliary loop was connected to the central cooling system of the laboratory through a plate heat exchanger, as shown in Fig. 2, and later the auxiliary water would flow through the secondary side of the plate heat exchangers and the inner coil of the test rig.

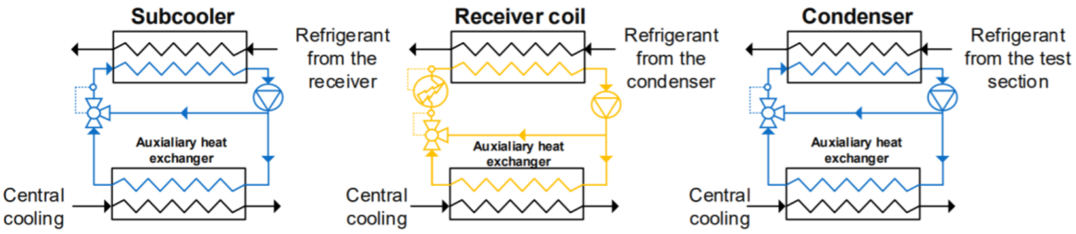

Fig. 2. Schematic of the auxiliary water loop of the test rig

3.3. TEST SECTION

The measurements of interest for the experimental investigation are obtained from the test section, and it is deemed the central part of the refrigerant loop. It comprises the copper heat sink, the microheater, the steel chassis, and the top cover. The steel chassis is soldered directly to the piping of the flow conditioning loop presented before, and the entire test section was covered with polyurethane insulation to minimize heat loss. Fig. 3 presents a schematic view of the exploded view of the main components of the test section.

3.3.1. The copper heat sink

The parallel microchannels and the inlet and outlet manifolds were micro-milled by a CNC machine from an Electrolytic Tough Pitch copper substrate. The parallel microchannels extended in a nominal footprint area of 1 cm^2 between the inlet and outlet plenum, and they comprised the main part of the test section. Three copper heat sinks with distinct channel geometries were manufactured. The CAD models of the copper heat sinks are shown in Fig.7 – 9. At the upper section of the copper heat sink, a groove was included to place a rubber O-ring to seal the refrigerant loop, and four holes were dedicated to assembling the test section. At the bottom, an additional 20 µm deep groove was milled to apply the solder paste used to vacuum-solder the microheater serpent to the copper heat sink.

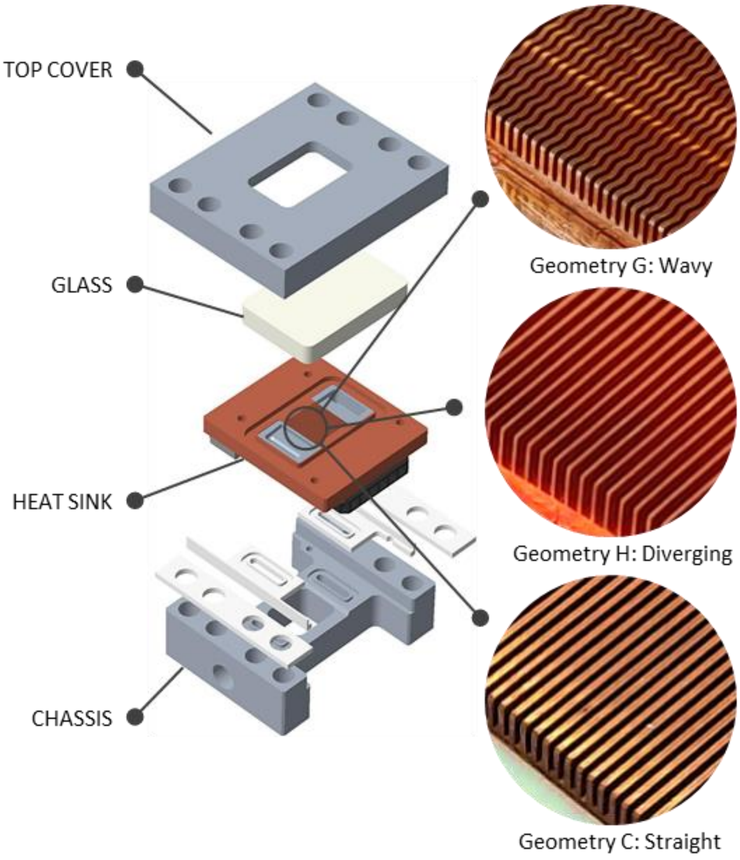

Fig. 3. Exploded view of the test section showing the heat sink, chassis, and microheater.

3.3.2. The microheater

The microheater was manufactured to allow infrared temperature measurements. Additionally, its design was intended to mirror a real power electronics application producing a uniform heat flux at the footprint of the heat sink. It consists of a 0.88 µm thick platinum serpentine on a 350 µm silicon wafer, where each serpentine features a connection pad to the power supply. The platinum Pt was deposited by vapor deposition following two serpentine shapes covering the entire bottom of the microchannels' footprint. Furthermore, four 4-wire platinum resistance thermal detectors (RTDs) are placed at the serpentine heater to monitor the local chip temperature. The location of the RTDs is at 1/8, 3/8, 5/8, and 7/8 of the flow-wise length of the channels, which consequently correspond to 0.125 cm, 0.375 cm, 0.625 cm, and 0.875 cm from the channel inlet. Lastly, the microheater was vacuum soldered with an Sn-Ag paste onto the bottom of each copper heat sink. The solder layers were verified for significant voids using 3-D tomography and found to be less than 1%. The pins of the power supply were soldered to the power pads of the microheater using a solder with a lower melting point than the solder paste as shown in Fig. 5. The serpentine heater was covered with a black matt heat-resistant paint to allow infrared thermography, and the RTDs were calibrated with a Rosemount Standard Platinum Resistance using a 165 °C thermal oil bath. The melting point of the solder paste was 221 °C, and a maximum temperature of 170 °C was considered in the experimental investigation to avoid the melting of the solder, especially for R134a as the working fluid. The infrared camera FLIR A655sc was calibrated using the platinum thermal detectors in the serpentine heater and the thermography imaged of the serpentine was examined through the software ResearchIR Pro Max by FLIR. Fig. 4 shows the bottom of the test section exemplifying the Infrared thermography of the microheater made during the experimental measurements.

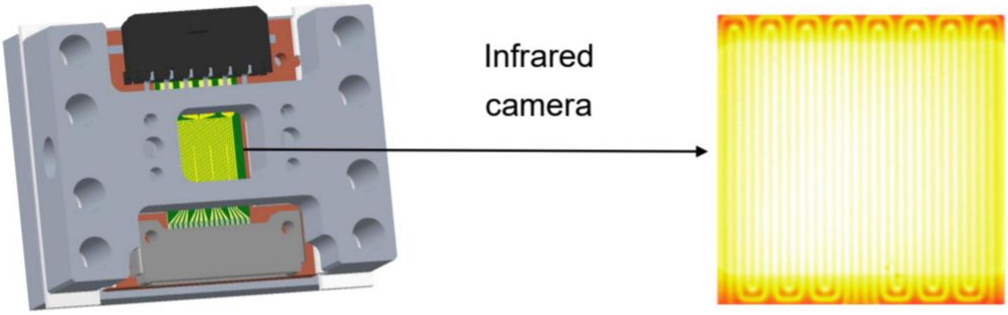

Fig. 4. Bottom view of the test section with the heat sink assembly mounted and a schematic view of an IR thermography.

3.3.3. The chassis

To aid with the assembly of the test section, the stainless-steel chassis allowed the refrigerant to flow from the main loop to the inlet plenum. The inlet and outlet sections of the chassis are fitted with two 0.25 mm Type K thermocouples to measure the temperature. For the absolute pressure measurement, a Danfoss AKS33 pressure tap was placed at the inlet and a pressure transmitter EndressHauser PMD75 at the outlet for the differential pressure.

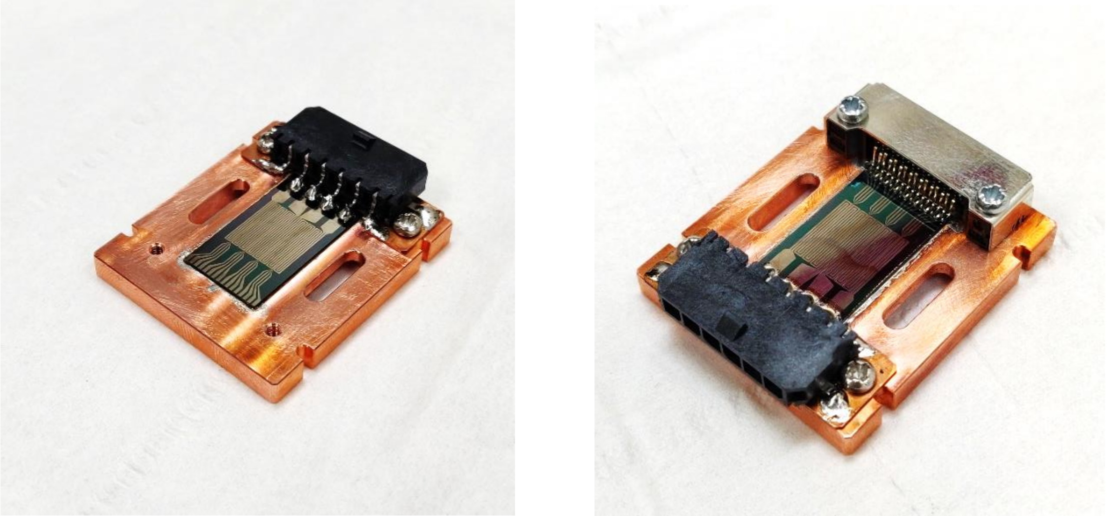

Fig. 5.Heat sink assembly and the microheater connector for the power supply.

3.3.4. The top cover

High-speed images are an imperative part in CHF measurements. The top cover allows visual access to the high-speed camera and seals the test rig as shown in Fig. 6. The cover consists of a stainless-steel structure with a central cavity and borosilicate glass. Additionally, a 100 µm thick heat resistant transparent silicon layer was used to seal and prevent boiling on top of the heat sinks. Polyurethane insulation is used around the whole test section to prevent heat loss. The high-speed videos were obtained through a Photon Fastcam Viewer 4 (PFV4) with a double 2x teleconverter and pulsed lighting (2 × 150 W GSVitec LED lights). Fig 8 shows an illustration of the high-speed camera view with an image of (512 × 896) pixels.

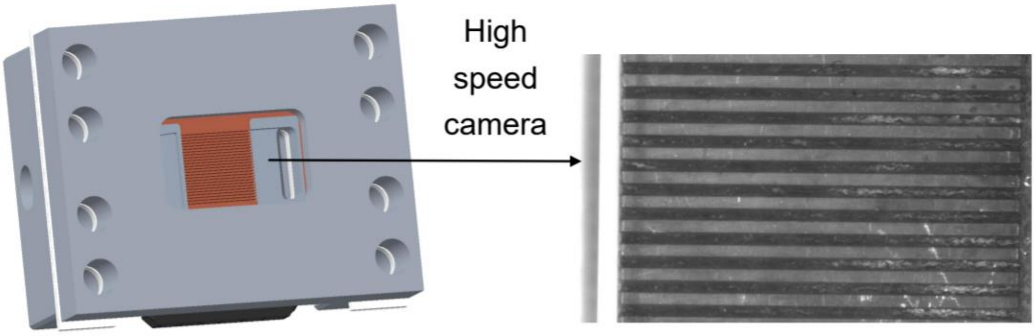

Fig. 6. Top view of the test section with the cavity where flow visualization takes place, and on the right a schematic a high-speed image.

3.4. CHANNEL GEOMETRY

The detail of the micro-milled copper heat sinks for the current investigation are detailed in this section. Three different geometries were employed: geometry C had the standard straight channels with nominal dimensions of (200 × 1200) µm, geometry H had diverging-like channels with channel nominal width of 200 µm at the inlet and 340 µm at the outlet, and geometry G had corrugated wavy walls with nominal dimensions of (200 × 1200) µm. The CAD model and images of the channels are displayed in Fig. 7 – 9. The nominal width of the microchannels matched to the nominal width of the CNC machine cutting tool and for all cases, the microchannels covered a nominal footprint area of 1 cm^2 and the channel length was 10 mm. The nominal geometric dimensions are displayed in Table 3.3. The test section was designed and built to allow the exchange of the heat sinks, which included a by-pass in the flow conditioning loop which was closed during all measurements.

Table 3.3. Channel dimensions for geometry C, H, and G.

Geometry	W_{ch} [μm]	H_{ch} [μm]	W_{fin} [μm]	D_h [μm]	L_h/D_{he} [$-$]	H_{ch}/W_{ch} [$-$]	N [$-$]
C ($straigth$)	198	1167	200	338	29.5	5.89	25
H ($diverging$)	200 – 340*	1200	200 – 60*	343	22.2	6.0 – 3.53*	25
G ($wavy$)	200	1200	200	338	29.5	5.89	25

* Indicates that the values correspond to inlet and outlet of the channels, respectively.

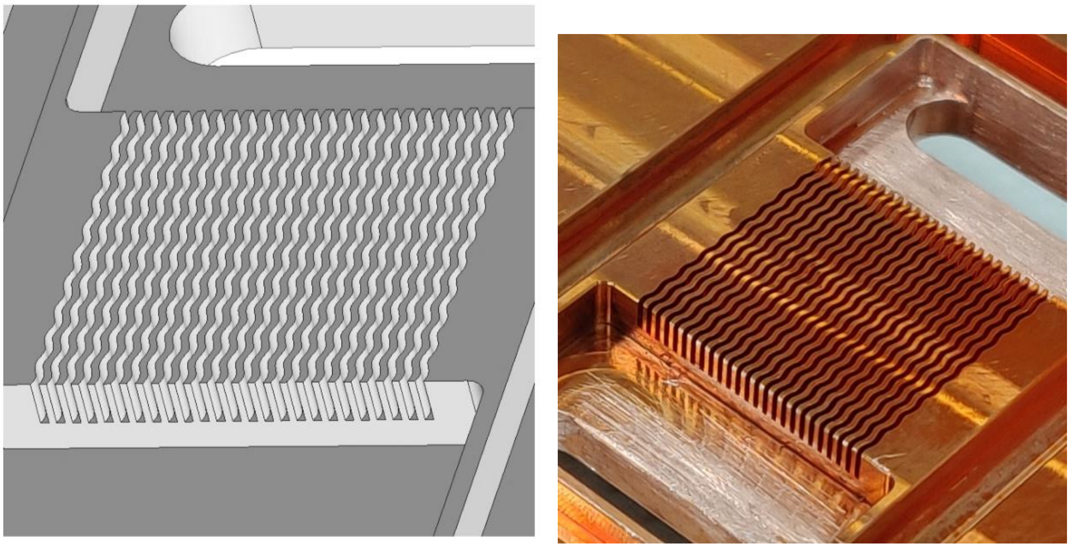

Fig. 7. CAD model of the copper heat sink for geometry G (wavy) on the left, and on the right the manufactured test sample.

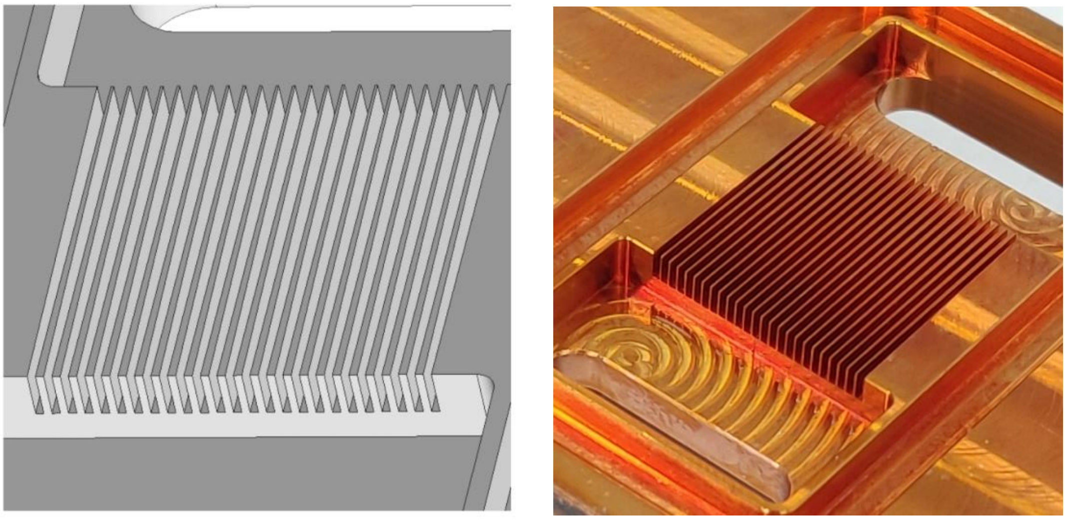

Fig. 8. CAD model of the copper heat sink for geometry H (diverging) on the left, and on the right the manufactured test sample.

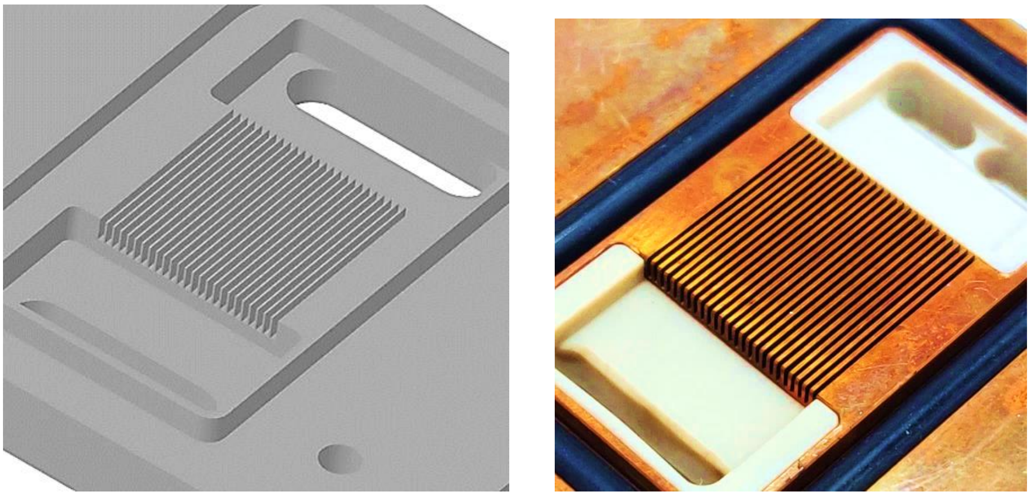

Fig. 9. CAD model of the copper heat sink for geometry C (straight) on the left, and on the right the manufactured test sample.

Additional details of the differences in the wall areas of the three geometries are presented in Section 4.1.4..

4

Methodology

This chapter contains the experimental methods applied to the investigation of CHF in microchannels. The information is arranged in three main sections. First, the data reduction methodology employed is presented for the calculation of the heat flux at the footprint and the wall of the channels. Later, the uncertainty evaluation applied to the investigation is detailed followed by the experimental methodology for CHF detection.

4.1. DATA REDUCTION

The methodology for the data reduction of the heat flux at the footprint and the wall of the channels required an evaluation of the different geometric characteristics of the test samples. This section presents the detailed calculation procedure of the parameters of interest that are analyzed in this investigation.

4.1.1. HEAT LOSSES CHARACTERIZATION

The heat losses in the test section are calculated according to Criscuolo's [10] dedicated tests, which developed an estimation of the heat losses from the microheater to the surroundings through convection, conduction, and radiation. The tests consisted of three different methodologies: single-phase at the outlet of channels, single-phase at the outlet of the test section, and tests without any flow. The data from the analysis were regressed concerning the temperature difference between the ambient and the average temperature of the microheater according to equation 1.

$$\dot{Q}_{AMB} = c1 + \Delta T_{H-A}^{c2} \tag{1}$$

According to Criscuolo [10], the adjusted R^2 value was 0.897, and the RMSE was 1.12 W, resulting in a 14 % standard error on the calculated heat loss.

4.1.2. MASS FLUX AND HEAT FLUX

The mass flux in the channels was calculated under the assumption of uniform mass flow rate distribution among all the parallel channels since the high-speed camera inspections determined negligible flow maldistribution at low mass fluxes. The mass flux is calculated according to the formula:

$$G = \frac{\dot{m}}{N.H_{ch}.W_{ch}} \tag{2}$$

where N is the number of parallel channels, and $\dot{m}$ is the measured mass flow rate. The heat flux at the footprint level of the channels was calculated considering the heat loss, according to the equation:

$$q_{fp} = \frac{V.I - \dot{Q}_{AMB}}{A_{fp}} \tag{3}$$

where A_{fp} corresponds to the total footprint area of the heat sink, V to the voltage of the power supply, and I the current of the microheater.

4.1.3. TEMPERATURE AT THE WALL

The wall temperature was calculated by assuming 1-D conduction through the silicon chip, the solder, and the copper. The temperature of the microheater T_h was obtained by considering the average of the four RTDs. Fig. 10 presents a schematic representation of the 1-D conduction from the microheater through the heat sink.

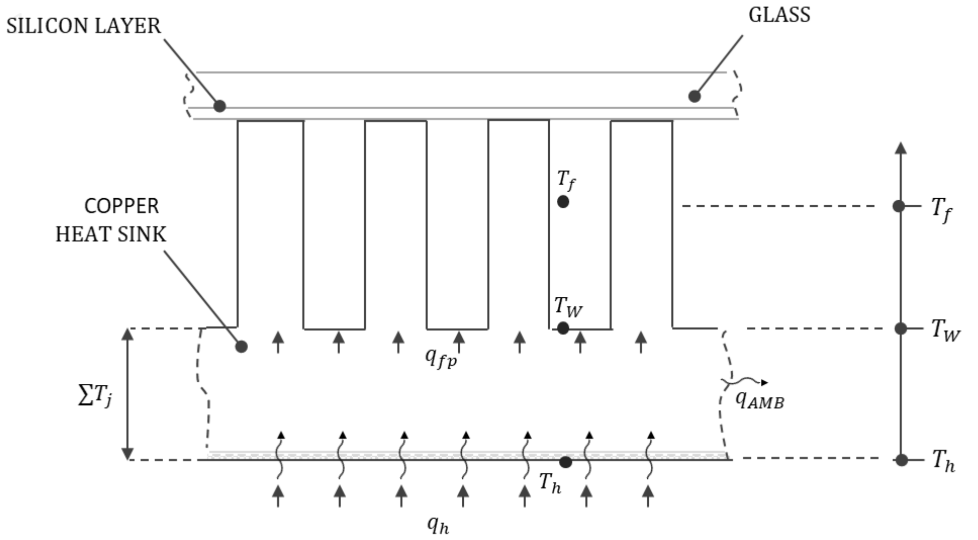

Fig. 10. Schematic of the temperature calculation by 1-D conduction from the heater temperature T_w to the wall temperature T_w of the channels.

The wall temperature was calculated by subtracting the conduction temperature drops according to the equation:

$$T_W = T_h - \Delta T_{Si} - \Delta T_{Sn} - \Delta T_{Cu} \tag{4}$$

$$\Delta T_j = k_j \, q_{fp}/t_j \qquad j \in \{Si, Sn, Cu\} \tag{5}$$

were the thermal conductivity of the silicon layer was calculated according to Shanks [41], and the copper and solder layer thermal conductivities were calculated by the regressions provided by the manufacturers, as follows:

$$k_{Cu} = 1.44 \times 10^{-4} T^2 - 1.09 \times 10^{-1} T + 3.90 \times 10^2 \tag{6}$$

$$k_{Cu} = -6.13 \times 10^{-5} T^2 - 1.92 \times 10^{-2} T + 6.14 \times 10^2 \tag{7}$$

where T was the average temperature in °C in the temperature values between 0 °C and 200 °C.

4.1.4. WALL HEAT FLUX

The heat flux at the wall level was calculated according to the fin model assuming that the separating walls of the channels resemble the temperature distribution of an adiabatic tip fin in the height-wise direction. Because of the distinct wall characteristics of the three geometries studied, a separate analysis made ensured that the fin parameter and fin efficiency reflected the effects of the corrugated walls of the wavy channels and wall thickness reduction of the expanding channels.

STRAIGHT CHANNELS

The wall heat flux for the straight channels was calculated employing the adiabatic tip fin model, based on the effective wetted perimeter P_{wet}, while the average heat flux q_{AV} different only by the absence of the fin efficiency η. Fig. 11 shows the schematic of the heat transfer area in the straight channels. The calculation for the wall heat flux results in the following equations:

$$q_W = \frac{q_{fp} . (W_f + W_{ch})}{(W_{ch} + 2\eta H_{ch})} \tag{8}$$

$$q_{AV} = \frac{q_{fp} . (W_f + W_{ch})}{(W_{ch} + 2H_{ch})} \tag{9}$$

$$m = \sqrt{\frac{2h_{tc}(W_f + L_{ch})}{k_{Cu} W_f L_{ch}}} \tag{10}$$

$$\eta = \frac{\tanh(mH_{ch})}{mH_{ch}} \tag{11}$$

where k_{Cu} is the thermal conductivity of copper, h_{tc} is the heat transfer coefficient, m is the fin parameter, and η is the fin efficiency.

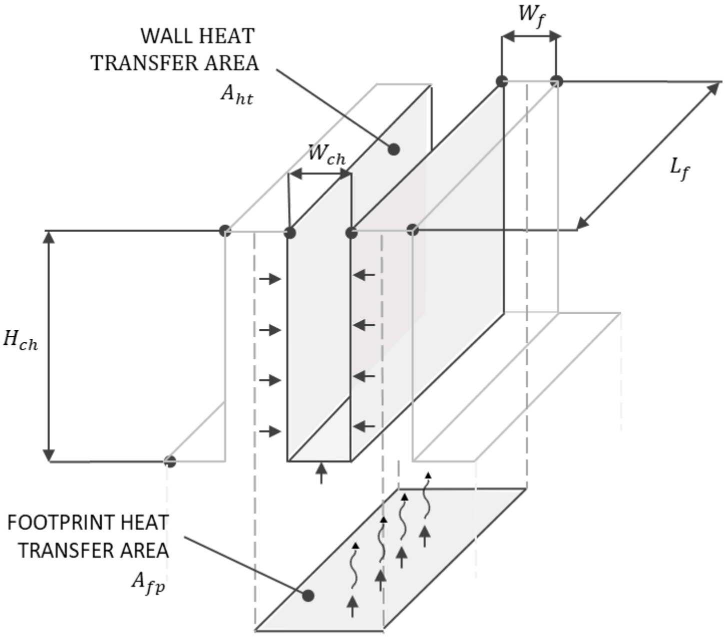

Fig. 11. Schematic of the area of footprint area and the area of the channels for geometry C.

The heat transfer coefficient was calculated by the equation:

$$h_{tc} = \frac{q_w}{T_W - T_{sat}} \tag{12}$$

The mentioned equations were solved iteratively due to the dependence of the fin parameter m on the heat transfer coefficient.

DIVERGING CHANNELS

The fin efficiency and fin parameter for the expanding channels were calculated considering the effect of the thickness reduction of the wall at the outlet section of the channels, this causes a variation of the width of the fin along with the flow-wise direction. Then, the fin efficiency was calculated in three different ways: fin parameter considering the average width of the walls of the channel, discretization of the fin to calculate the mean fin parameter, and discretization of the fin to calculate the mean fin efficiency. The fin was discretized in 25 equidistant sections, and the results between the fin efficiencies differed from each other by less than >2% difference. Fig. 12 presents the schematic of the discretization of the fin, and Fig. 13 the heat transfer area of the walls in the expanding channels.

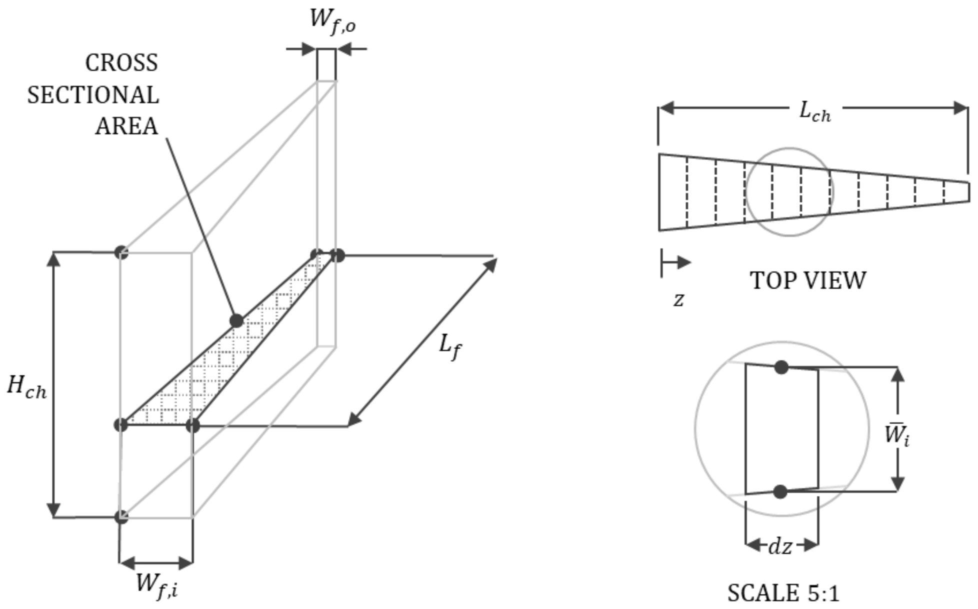

Fig. 12. Schematic of the discretization of the diverging channels for the calculation of the fin efficiency and fin parameter

The fin efficiency was calculated according to the equations:

$$\begin{cases} m_{ave} = \sqrt{\dfrac{2h_{tc}}{k_{Cu}.\overline{W}}} \\ \eta_{ave} = \dfrac{\tanh(m_{ave}.H_{ch})}{m_{ave}.H_{ch}} \end{cases} \tag{13}$$

$$\begin{cases} m_i = \sqrt{\dfrac{2h_{tc}}{k_{Cu}.\overline{W_i}}} \\ m_{mean} = \displaystyle\sum_{i=1}^{N} \frac{m_i}{N} \\ \eta' = \dfrac{\tanh(m_{mean}.H_{ch})}{m_{mean}.H_{ch}} \end{cases} \tag{14}$$

$$\begin{cases} m_i = \sqrt{\dfrac{2h}{k_{Cu}.\overline{W_i}}} \\ \eta_i = \dfrac{\tanh(m_i.H_{ch})}{m_i.H_{ch}} \\ \eta'' = \displaystyle\sum_{i=1}^{N} \frac{\eta_i}{N} \end{cases} \tag{15}$$

where k_{Cu} is the thermal conductivity of copper, h_{tc} is the heat transfer coefficient, m is the fin parameter, and η is the fin efficiency

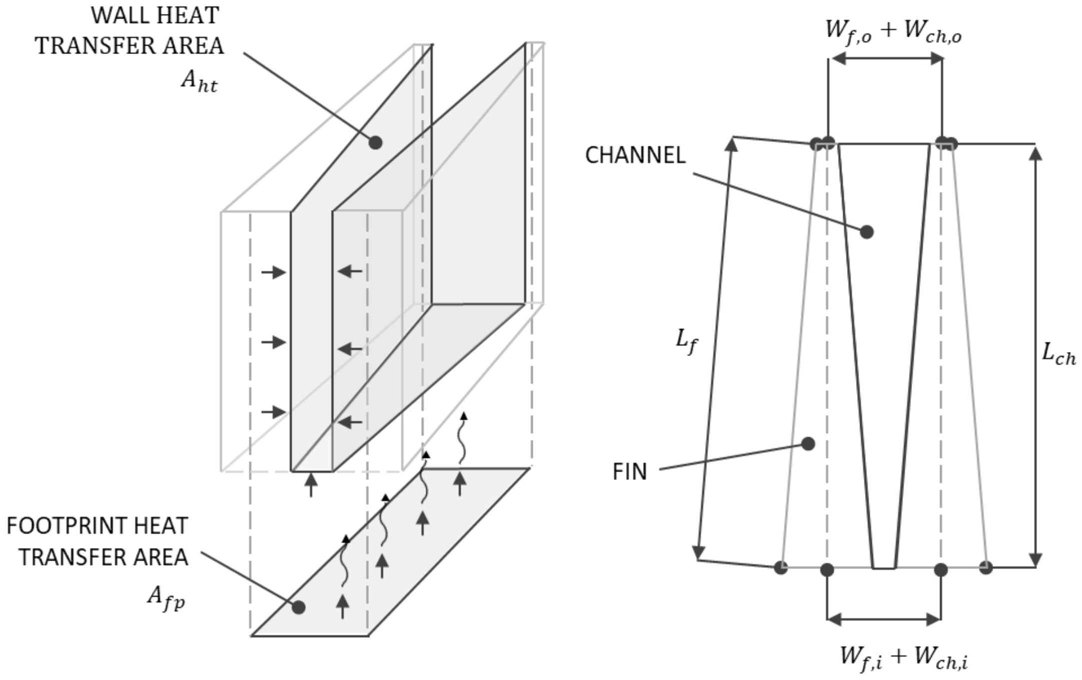

Fig. 13. Schematic of the wall channels area for geometry H used to calculate the wall flux q_w.

The wall heat flux and average heat flux was calculated by:

$$q_W = \frac{q_{fp}.\left(W_{f,i} + W_{ch,i}\right)L_{ch}}{\left(\overline{W_{ch}}L_{ch} + 2\eta H_{ch}L_f\right)} \tag{16}$$

$$q_{AV} = \frac{q_{fp}.\left(W_{f,i} + W_{ch,i}\right)L_{ch}}{\left(\overline{W_{ch}}L_{ch} + 2H_{ch}L_f\right)} \tag{17}$$

where L_{ch} is the length of the channels and L_f is the length of the fin. These two values differed from each other. The heat transfer coefficient was calculated by:

$$h = \frac{q_w}{T_W - T_{sat}} \tag{18}$$

where T_w is the wall temperature, and T_{sat} is the average temperature between the temperature measurements at the inlet and outlet of the channels.

SINUSOIDAL WAVY CHANNELS

The area enhancement of the corrugated wall of the sinusoidal wavy channels was accounted for according to Holger Martin [27], which ignores the effect of corrugations and treats the walls as if they were straight by employing an area enlargement factor Φ. Fig. 14 shows the concept of the enlargement factor comparing the un-corrugated and corrugated length of the fin. Additionally, Fig. 15 shows the area heat transfer of the wavy channels involved in the calculation of the wall heat flux q_w. The wall heat flux was calculated based on the common practice of ignoring the wall corrugation considering the area enlargement factor Φ.

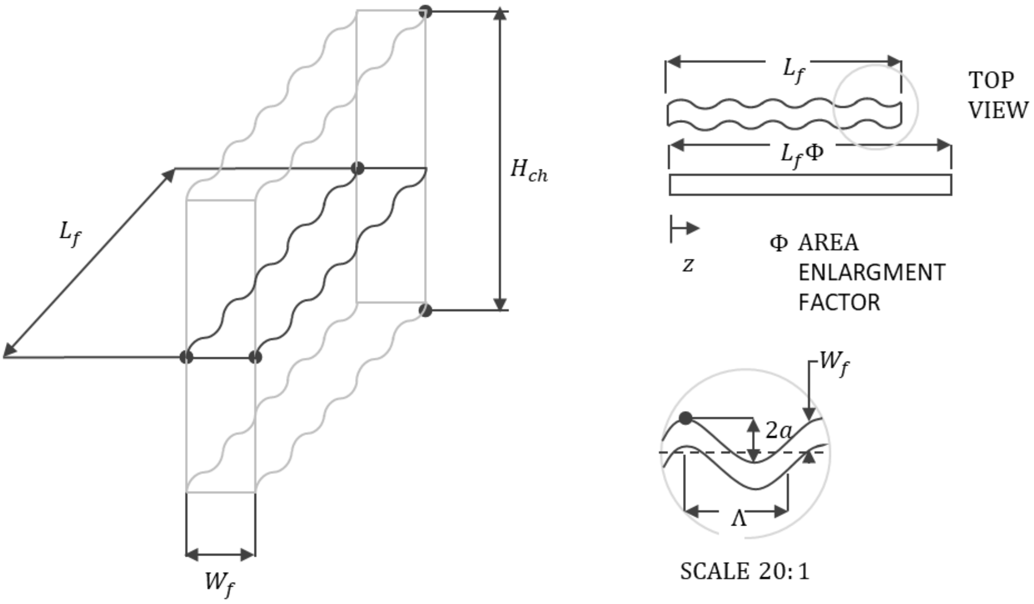

Fig. 14. Schematic of the area enhancement of the wavy walls in geometry G on the LEFT, and the area enlargement factor concept on the RIGHT.

The area enlargement factor was calculated by:

$$\mathrm{X} = \frac{2\pi a}{\Lambda} \tag{19}$$

$$\Phi \approx \frac{1}{6}\left(1 + \sqrt{1 + \mathrm{X}^2} + 4\sqrt{1 + \frac{\mathrm{X}^2}{2}}\right) \tag{20}$$

where X is the corrugated parameter, a is the amplitude of the corrugation, and Λ is the wavelength of the sinusoidal walls.

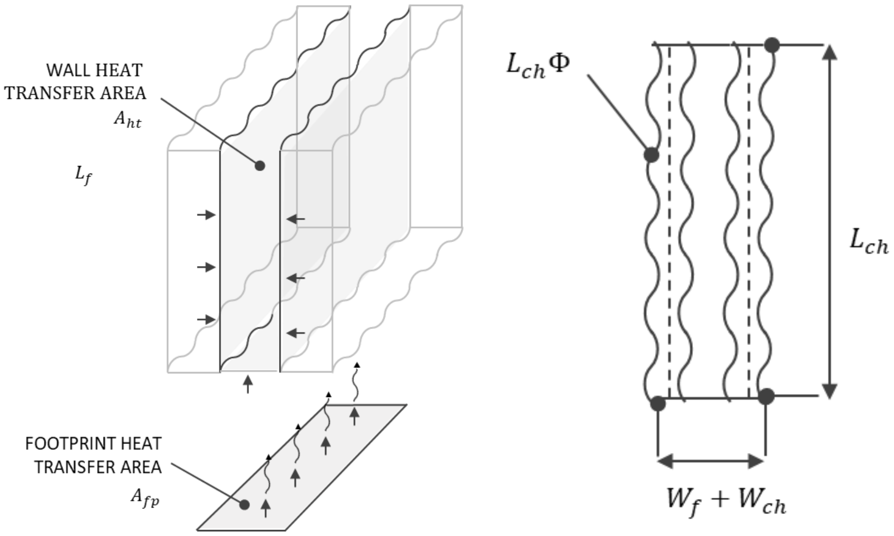

Fig. 15. Schematic of the wall channel area in geometry G for the calculation of q_w.

The wall flux was calculated according to the equations:

$$\begin{cases} m_{ave} = \sqrt{\dfrac{2h\left(W_f + L_{ch}\Phi\right)}{k_{Cu}\left(W_f L_{ch}\Phi\right)}} \\ \eta = \dfrac{\tanh(mh)}{mh} \end{cases} \tag{21}$$

$$q_w = \frac{q_{fp}.\left(W_f + W_{ch}\right)L_{ch}}{(W_{ch} + 2\eta h)L_{ch}\Phi} \tag{22}$$

$$q_{AV} = \frac{q_{fp}.\left(W_f + W_{ch}\right)L_{ch}}{(W_{ch} + 2h)L_{ch}\Phi} \tag{23}$$

where k_{Cu} is the thermal conductivity of copper, h is the heat transfer coefficient, m is the fin parameter, η is the fin efficiency, and Φ is the area enlargement factor

4.1.5. PRESSURE DROP

The pressures measured P_{in} and P_{out} correspond to pressure transducers located at the inlet and outlet manifold of the test section. Therefore, the inlet pressure $P_{in,ch}$ of the microchannels is obtained by subtracting the pressure drop corresponding from the inlet manifold to the inlet of the microchannels, and for the outlet pressure $P_{out,ch}$ by adding the pressure drop from the outlet of the channels to the outlet manifold.

PESSURE LOSS AT INLET

The pressure loss at the inlet manifold consists of the pressure loss caused by a straight section, an elbow with changing area, and another straight section. These are accounted for by a regression according to Kærn [19] which was obtained by separated adiabatic pressure drop tests to account for the liquid pressure loss in the inlet manifold. The refrigerant also encounters a sudden compression by sudden area reduction at the inlet of the channels. The pressure loss is accounted for according to Chalfi and Ghiaasiaan that considers the pressure drop in capillaries by employing the vena-contracta coefficient [7]. Fig. 16 shows the pressure loss accounted for in the calculation of the inlet pressure P_{in}.

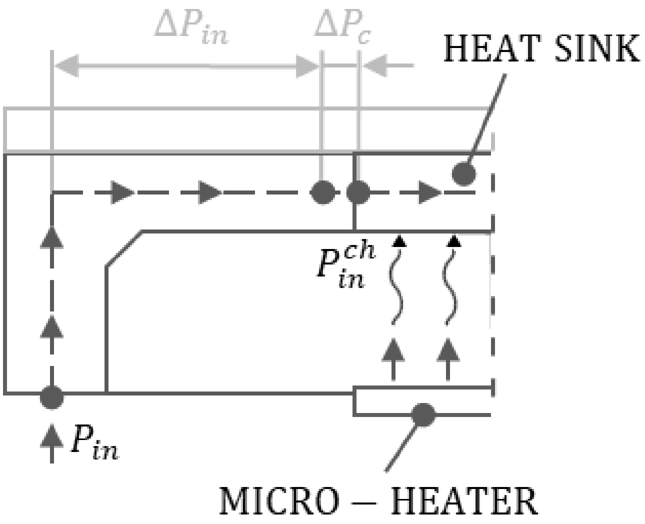

Fig. 16. Illustration of the pressure drop at the inlet manifold including the pressure drop ΔP_{in} and pressure drop ΔP_c due to the sudden contraction at the inlet of the channels.

The fit regression for the straight sections and elbow is:

$$\Delta P_{in} = \frac{c1 G_{ma}^{c2}}{2\rho_l} \tag{24}$$

where the coefficients c1 and c2 are presented in [10]. The pressure loss due to the sudden compression was calculated accordingly by:

$$\Delta P_{c,R} = \frac{G^2}{2\rho_l(1-\sigma_c^2)} \tag{25}$$

Then, the inlet pressure is calculated by the equation:

$$P_{in}^{ch} = P_{in} - \overbrace{\Delta P_{st,1} - \Delta P_{el} - \Delta P_{st,2}}^{\Delta P_{in}} - \Delta P_{co} \tag{26}$$

PRESSURE DROP AT OUTLET

The pressure losses at the outlet manifold are analogous to the inlet one. The outlet manifold consists of a straight section, an elbow with changing area, and another straight section. Similarly, these are accounted for by a fit regression performed by Kærn [19], which was obtained from a series of adiabatic two-phase pressure drop tests using the preheater with different fluids. The refrigerant experiences a sudden expansion due to the area enlargement from the outlet of the channels to the outlet plenum. The pressure loss by the two-phase flow expansion was calculated according to Chalfi and Ghiaasiaan under the assumption that both phases are incompressible and homogeneous flow conditions [7]. Fig. 17 presents the schematic of the pressure losses accounted for the calculation of the outlet pressure P_{out}.

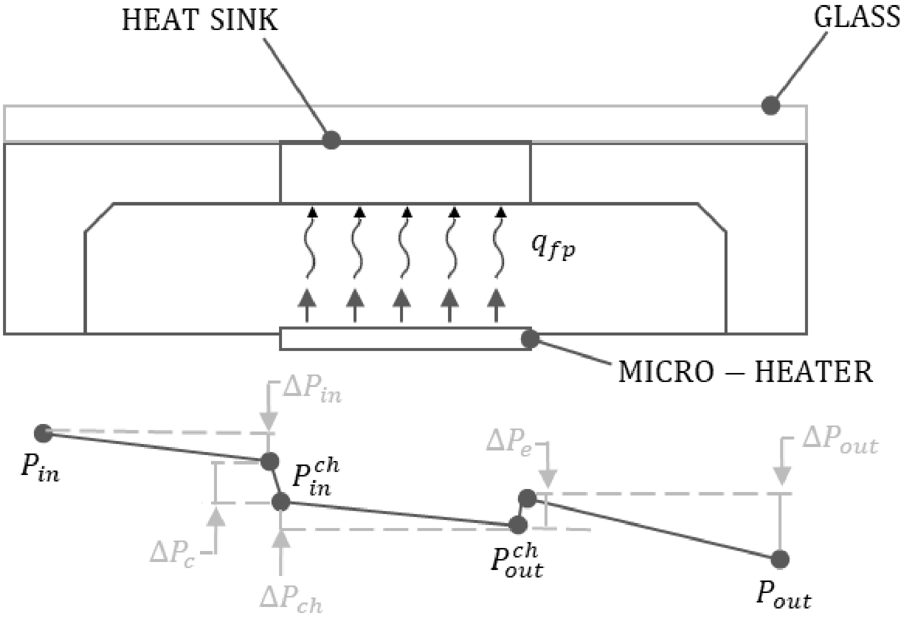

Fig. 17. Illustration of the pressure drop across test section, showing the pressure drop ΔP_e for the sudden expansion at the outlet of the channels and the pressure drop ΔP_{out} at the outlet manifold.

Accordingly, the fit regression for the outlet manifold is:

$$\Delta P_{out,fit} = \frac{c3 G_{ma}^2}{2\rho_l} \tag{27}$$

$$\Delta P_{out} = \Delta P_{out,fit} . \left(1 + c4 We_{\mathrm{hom}}^{c5} x_{out}^{c6}\right) \tag{28}$$

Where $\Delta P_{out,fit}$ accounts for the single-phase pressure loss, We_{hom} is the homogeneous Weber number, and G_{ma} is the mass flux in the manifold. The coefficient c3 is presented in [10]. The pressure loss due to the expansion was calculated accordingly with the equation:

$$\Delta P_e = \frac{G_{ma}^2}{\rho_l}\sigma(\sigma-1)\left(1+\frac{x_{out}}{\frac{\rho_l}{\rho_G}-1}\right) \tag{29}$$

And the outlet pressure at the channels was obtained by:

$$P_{out}^{ch} = P_{out} + \underbrace{\Delta P_{st,3} + \Delta P_{el} + \Delta P_{st,4}}_{\Delta P_{out}} + \Delta P_e \tag{30}$$

4.1.6. CRITICAL VAPOR QUALITY

The critical vapor quality x_{cr} (or outlet vapor quality) was calculated by using the energy balance. Fig. 18 presents a schematic of the parameters involved in the calculation of the critical vapor quality.

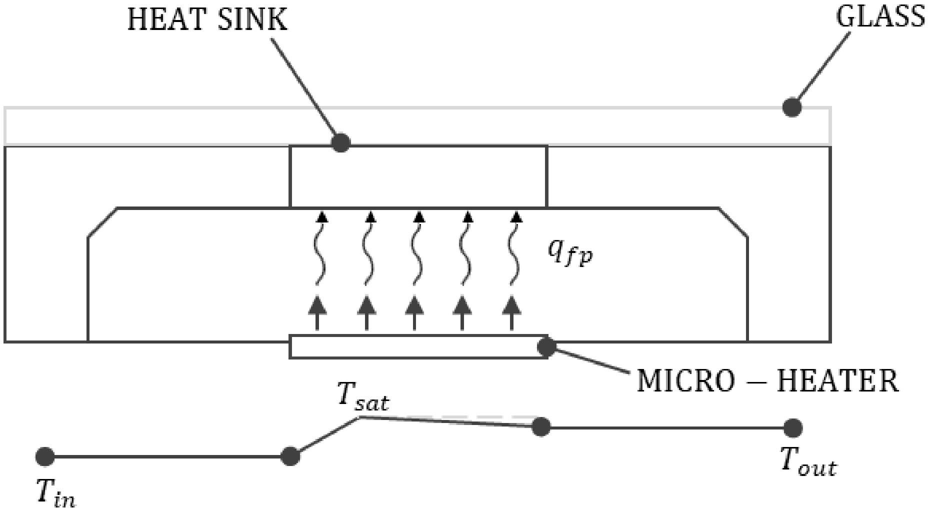

Fig. 18. Illustration of the flow temperature across the test section used to calculate the critical vapor quality x_{cr} through the energy balance.

Accordingly, the critical vapor quality is calculated by:

$$x_{cr} = \frac{h_{out} - h_{sat}^{L}\left(P_{out}^{ch}\right)}{\Delta h_{fg}\left(P_{out}^{ch}\right)}$$

$$h_{in} = h\left(T_{in}, P_{in}^{ch}\right)$$

$$h_{out} = h_{in}\left(T_{in}, P_{in}^{ch}\right) + \frac{Q_{fp}}{\dot{m}}$$

where h_{out} and h_{in} are the enthalpies at the outlet and inlet of the channels, Q_{fp} is the heat form the microheater minus the heat loss, and Δh_{fg} the latent heat of vaporization.

$$x_{cr} = \frac{q_w}{G.\Delta h_{fg}} . \frac{P_{wet}}{A_{ch}} - \frac{\Delta h_{sub}}{\Delta h_{fg}}$$

$$= \frac{q_w}{G.\Delta h_{fg}} . \frac{4.L_h}{D_{wet}} - \frac{\Delta h_{sub}}{\Delta h_{fg}} \quad (31)$$

The critical heat flux can reveal the definition of the hydraulic diameter using the effective wetted perimeter P_{wet}. This later can be used to expose the effective wetted perimeter D_{wet}, as shown in equation 31.

4.1.7. LOCAL QUANTITIES

The local quantities in the flow-wise direction were calculated based on the discretization of 24 equidistant segments of the channels. These started from the location of the first RTD until the outmost one. The discretization procedure is shown in Fig. 19 and 20. The wall temperature was obtained under the assumption of 1-D conduction between the microheater and the root of the channel walls. For these calculations, the infrared maps were employed to obtain the local distribution of the heater temperature $T_h(z)$. On the other hand, the local pressure $p(z)$, local enthalpy $h(z)$, and local vapor quality $x(z)$ were obtained by a linear interpolation corresponding to each flow-wise local coordinate z.

Consequently, the local wall temperature was calculated by the equation:

$$T_w(\tilde{z}) = T_h(\tilde{z}) - \Delta T_{Si} - \Delta T_{Sn} - \Delta T_{Cu} \quad (32)$$

$$\Delta T_j = k_j \, q_{fp}/t_j \qquad j \in \{Si, Sn, Cu\} \quad (33)$$

$$T(z) \begin{cases} T_{sat}\big(p(z)\big) & if \; x_{loc}(z) > 0 \\ T\,\big(p(z), h(z)\big) & if \; x_{loc}(z) < 0 \end{cases} \quad (34)$$

where the thermal conductivities were calculated according to Section 4.1.3. The local pressure $p(z)$, local enthalpy $h(z)$, and local vapor quality $x_{loc}(z)$ were calculated by the following equations:

$$p(z) = p_{in}^{ch} - \Delta P_{ch} \left(\frac{z}{L}\right) \quad (35)$$

$$h(z) = h_{in}^{ch} + \Delta h_{ch} \left(\frac{z}{L}\right) \quad (36)$$

$$x_{loc} = \frac{h(z) - h_{sat}^{L}\big(p(z)\big)}{\Delta h_{fg}\big(p(z)\big)} \quad (37)$$

where p_{in}^{ch} is the pressure at the inlet of the channels, L_{ch} is the length of the heat sink, and z is the local flow-wise coordinate.

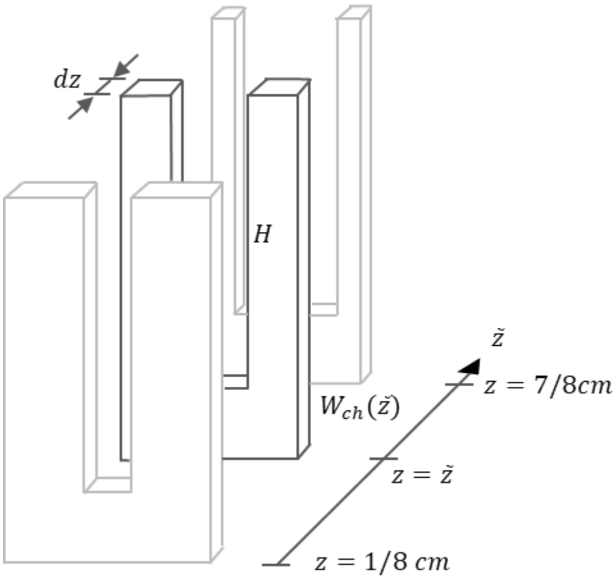

Fig. 19. Illustration of the discretization in the flow wise discrete coordinate $\breve{z}$ for the geometry H.

The local wall flux for the expanding channels is calculated by:

$$q_W(z) = \frac{q_{fp}.\left(\overline{W}_f + \overline{W}_{ch}\right)L_{ch}}{\left(\overline{W}_{ch}L_{ch} + 2\eta(z)H_{ch}L_f\right)} \tag{38}$$

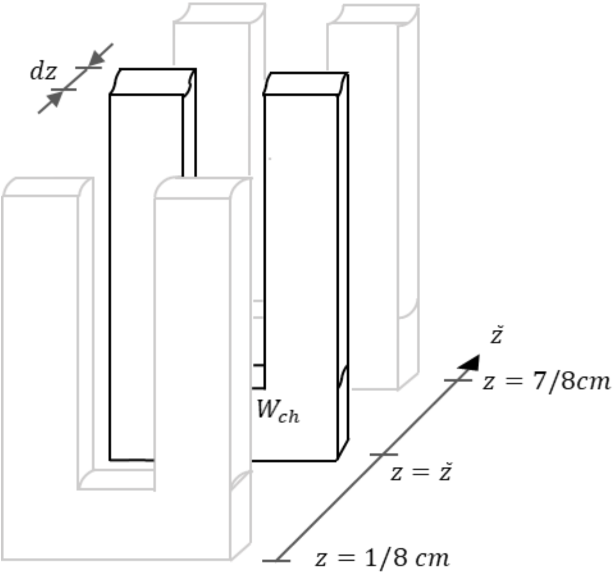

Fig. 20. Illustration of the discretization in the flow wise discrete coordinate $\breve{z}$ for the geometry G.

The local wall flux for the wavy channels was calculated by:

$$q_W(z) = \frac{q_{fp}.\left(W_f + W_{ch}\right)}{(W_{ch} + 2\eta(z)H_{ch})\Phi} \tag{39}$$

And the local wall flux for the straight channels was calculated by the equation:

$$q_W(z) = \frac{q_{fp}.\left(W_f + W_{ch}\right)}{\left(W_{ch} + 2\eta(z)H_{ch}\right)} \tag{40}$$

The local heat transfer coefficient h is calculated with the local heat flux q_w.

4.2. UNCERTAINTY

The single sample error propagation method by Kline and McClintock [13] was employed to calculate the experimental uncertainties risen from the data reduction, where no correlation between the input variables was assumed. The uncertainty calculation accounted two types of errors on a generic measured quantity x_i with n samples and whose mean value is $\bar{x}_i$. The bias uncertainty w_{x_i} and random uncertainty s_{x_i} were calculated according to [18], and the overall uncertainty $u_{\bar{x}_i}$ was estimated with the sum of the squares according to equation 41, since the two types of uncertainties can be considered independent. In the case of calculated variables $y = f(\bar{x}_j)$, the uncertainty on y propagated from the uncertainties in x_j was calculated following the error propagation for uncorrelated variables according to equation 42. The instruments uncertainty values in Table 3.2 were used and the uncertainty on a calculated variable u_y was expanded to a confidence interval close to 95% (20:1 odds) with a 2σ coverage factor coverage. Additionally, the uncertainties of the layer thicknesses were estimated to 2 µm for the silicon, 4.5 µm for the solder and 20 µm for the copper, and for the CHF detection method employed, an additional uncertainty was estimated to 0.5 V for the power supply. Table 4.4 presents the measurement range as well as the relative single sample and the absolute uncertainties based on 95% confidence interval. The uncertainty of the wall CHF was higher than the footprint one because of the uncertainty on the mass flux which was relatively high because of dimensional uncertainties, that propagated from the mass flux to the footprint, and later to the wall CHF. Nonetheless, the uncertainties were well accepted for the purpose of the study.

$$u_{\bar{x}_i} = \sqrt{\omega_{\bar{x}_i}^2 + s_{\bar{x}_i}^2} \tag{41}$$

$$u_y = \sqrt{\sum_{j=1}^{n} \left(\frac{\partial f}{\partial \bar{x}_j} u_{\bar{x}_j}\right)^2} \tag{42}$$

4.3. EXPERIMENTAL PROCEDURE

The experimental points of interest obtained from the test rig followed an experimental procedure, which is described in this section. While investigating the CHF with a given fluid, either R134a or R1234yf, three parameters were deemed as degrees of freedom and carefully controlled during the measurements. These are the saturation temperature at the outlet of the channels, the mass flux, and the inlet subcooling. When an experimental series took place, the electric pre-heater power supply was adjusted to obtain the desired inlet subcooling level, either 2±1 °C or 8±1 °C. Due to the large thermal inertia of the hose and piping, the system took approximately 15-20 minutes to stabilize once a different subcooling level was set. The saturation temperature was set by the receiver at 30 °C or 40 °C and the variable speed drive of the pump was manually adjusted to the desired mass flux. Subsequently, the power supply of the microheater was increased until the CHF was reached. For a given mass flux, the two-phase flow became dominant inside the channels once boiling took place, causing the pressure drop to increase. Consequently, the inlet subcooling increased slightly with increasing mass flux. Additionally, the pressure drop also caused a slight decrease in the mass flux, which had to be repeatedly adjusted to the nominal value of the test run. During the measurements, the by-pass and safety valves were kept closed. Once the system achieved steady conditions the CHF detection took place.

Table 4.4. Range and uncertainties of reduced variables based on 95% confidence.

Variables	Range	Relative uncertainty, %	Absolute uncertainty
Mass flux $\boldsymbol{G}$, kg/m^{2}s	323 – 1249	6.7 – 7.0	22.6 – 84.9
Critical vapor quality, $\boldsymbol{x_{cr}}$	0.41 – 1.07		0.005 – 0.015
Footprint CHF, $\boldsymbol{q_{fp}}$,W/cm^2	315 – 852	0.9 – 1.5	4.7 – 7.5
Wall CHF, $\boldsymbol{q_w}$, W/cm^2	59 – 197	5.1 – 5.6	3.0 – 11.1
Saturation temperature, $\boldsymbol{T_{sat}}$, °C	30.5 – 42.2		0.06 – 0.08
Inlet subcooling, $\Delta\boldsymbol{T_{sub}}$, K	1.8 – 12.7		0.17 – 0.19

4.3.1. CHF DETECTION

The CHF detection in the present investigation relied on the sharp temperature increase of any of the RTDs in the microheater, causing a digital output signal from Labview that triggered a safe-stop function to stop the power supply. Therefore, the procedure consisted in gradually increasing the voltage of the microheater power supply and observing the thermal response of the RTDs. In the case of being far away from the CHF, the signal of the RTDs resulted in an increment of first-order response. However, when the CHF occurred, the RTDs presented a sharp second-order growth. Fig. 21 shows the RTDs temperature and voltage of the microheater signal versus time during an experimental measurement, where the increment steps on the voltage were five steps of 5 V, three steps of 1 V, and a last 0.5 V. When the CHF was detected and the safe-stop was triggered, the voltage was reduced by 0.25 V and the measurement of a point was obtained once the steady-state of the system was verified. The steady-state condition was defined by observing a temperature variation of fewer than 0.05 °C over a 120s interval. In most cases, the mass flux was repeatedly adjusted to compensate for its decrease caused by the pressure drop when increasing the heat flux through the channels. Later, the parameters of interest, such as temperatures, pressures, and mass flow rate were acquired for 60 seconds at 10 Hz, and the power supplies were recorded at 1.5 Hz. Subsequently, the infrared camera recorded 30 frames, and the high-speed camera recorded 150 frames at 10 kHz during the recording of the results. The high-speed camera allowed the inspection of the two-phase flow stability during the experimental measurements and verify the absence of significant vapor backflow at low mass fluxes.

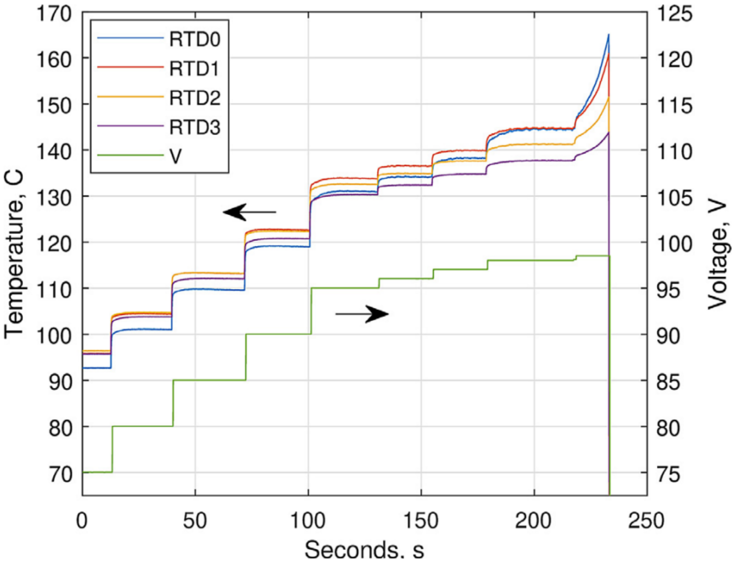

Fig. 21. *R*TDs and voltage signal response vs. time during the measurement of an experimental point. The RTD0 to RTD3 correspond to the RTDs placed at 7/8, 5/8, 3/8 and 1/8 of the channel length flow wise, respectively.

previous procedure. At low mass flux conditions, the increase in voltage of the microheater power supply never resulted in a second-order response in the RTDs signal. Instead, when the voltage was increased, the RTD thermal response resulted in a first-order, and the power uptake momentarily raised, but then slowly dropped to the previous value. This occurred because of the increased resistance of the platinum serpent with the increase in temperature, which compensated for the increase in voltage resulting in the same power uptake value. Therefore, when the power supply could not be further increased in these conditions, the experimental point was measured and assumed to be the CHF. Fig. 22 presents the flowchart of the experimental procedure.

4.3.2. VALIDATION

The experimental setup was validated by Criscuolo [10], who performed single-phase heat transfer test runs and benchmarked them with well-established prediction methods, concealing a close agreement with them, and validating the data reduction and the test section for the analysis of CHF in microchannels.

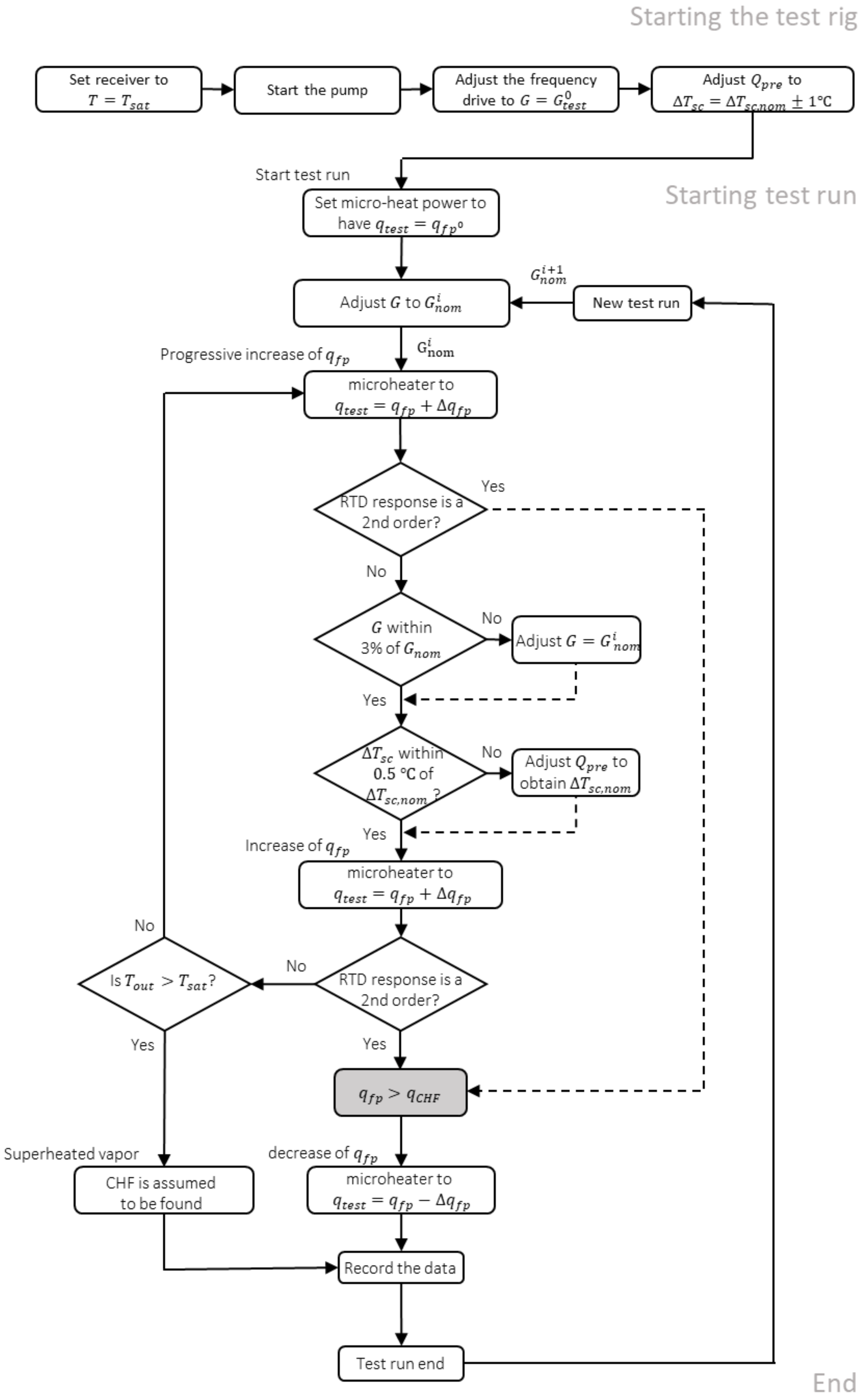

Fig. 22. Flowchart of the experimental procedure for the CHF detection.

5

Results

This chapter contains the results of the experimental investigation where the different research questions formulated in Chapter 2. are addressed. Each section presents the parametric analysis of the CHF under the test conditions, followed by a discussion regarding the major findings of the analysis and a summary. Accordingly, the following questions are answered:

- Question 1: what are the critical heat flux (CHF) characteristics in micro-milled sinusoidal, expanding, and straight multi-microchannels copper heat sinks in flow boiling with R1234yf and R135a?
- Question 2: What is the relationship between the measured critical heat flux (CHF) and the mass flux, the saturation temperature, and inlet subcooling with R134a and R1234yf?
- Question 3: How the wall geometry (diverging design, sinusoidal wavy design, conventional straight design) affects the wall CHF?

5.1. FOOTPRINT CHF

For the actual application of the cooling heat sink, the footprint CHF is much more practical than the wall heat flux since it accounts for the total heat dissipation rate per unit area of the cooling system. This section presents the results for the footprint CHF with all the geometries studied. The effect of the absence of inlet restriction is compared with previous experimental results. Finally, the effect of the main parameters on the footprint CHF is detailed and discussed. For the easiness of reference, the test samples are referred to by the corresponding labels shown in Table 3.3. Accordingly, the wavy sinusoidal design is labeled as G, the diverging design as H, and the straight channel design as C.

5.1.1. FOOTPRINT CHF RESULTS

Fig. 23a and 23b present the footprint CHF results versus mass flux with R134a at different inlet subcooling for nominal saturation temperatures of 30 °C and 40 °C, respectively, and in the mass velocity range of 320—1200 kg/m^2. Fig. 24a and 24b show the same results with R1234yf. The footprint CHF increased with increasing mass flux in all test conditions. In the case of R134a, the region of low mass flux is characterized by a steep increase in the CHF, while at high mass it presents a flattening behavior. In the low-mass-flux region, the results with all geometries show a similar value of around 317 – 360 W/cm^2 at 30 °C saturation temperature and 315 – 341 W/cm^2 at 40 °C saturation temperature. The highest CHF is obtained with geometry G and with a saturation temperature of 30 °C, resulting in a value of 852.1 W/cm^2 at the highest mass flux. The footprint CHF with geometry C and H shows similar results, with a value of 652 W/cm^2 and 612.6 W/cm^2, respectively. On the other hand, the rate of increase in the low-mass-flux region was smaller with R1234yf, but similarly, the results appear to flatten at the highest mass flux. In the low-mass-flux region, the results with all geometries show a value around 364 – 303 W/m^2 at 30 °C saturation temperature and 259 – 290 W/cm^2 at 40 °C saturation temperature. Equally to R134a, the highest footprint CHF with R1234yf was obtained with geometry G and saturation temperature of 30 °C, with a value of 620.5 W/ cm^2, while the CHF with geometry C and H are 461.1 W/cm^2 and 448.1 W/cm^2 respectively.

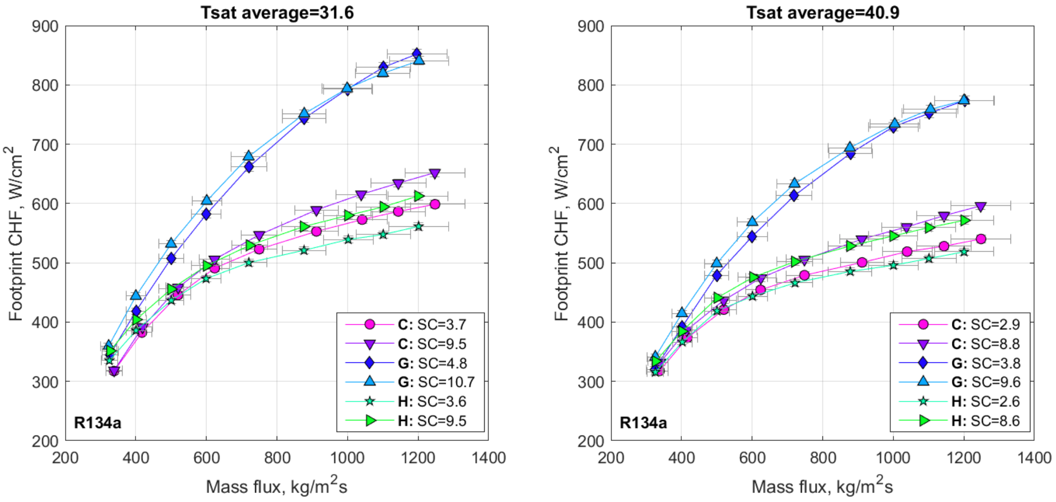

(a) (b)

Fig. 23. Footprint CHF vs. mass flux for R134a. The average saturation temperature was 31.6 °C (a) and 40.9 °C (b). The average subcooling (SC) in K indicated for each curve concerning geometry C, H, and G.

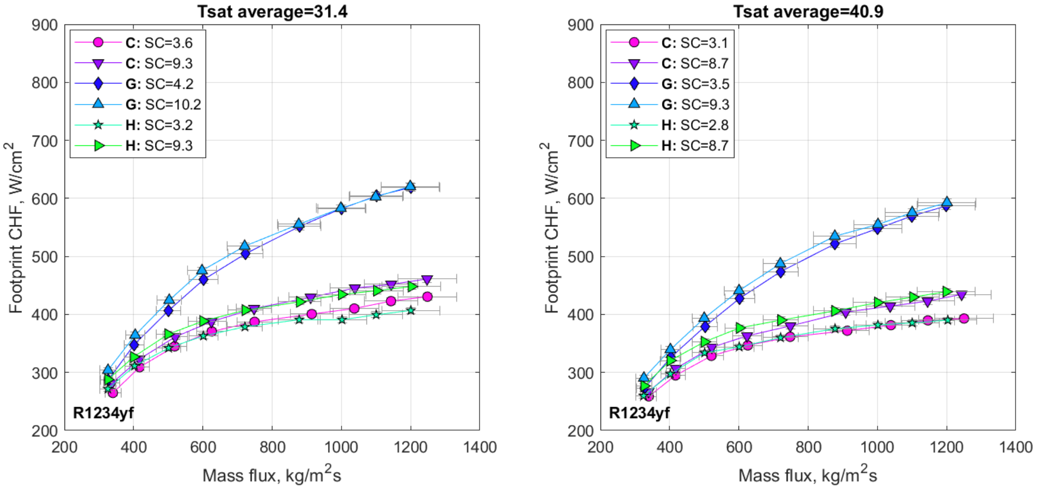

(a) **(b)**

Fig. 24. Footprint CHF vs. mass flux for R1234yf. The average saturation temperature was 31.4 °C (a) and 40.9 °C (b). The average subcooling (SC) in K indicated for each curve concerning geometry C, H, and G.

For both working fluids, there is an evident effect of inlet subcooling on the footprint CHF at constant mass flux with geometry H and C. However, the effect is insignificant with geometry G. Further details on the subcooling effect are provided in Section 5.1.3. In contrast to the inlet subcooling effect, the increase in saturation temperature systematically reduces the footprint CHF with all geometries. In the case of R134a, the CHF at 40 °C saturation temperature, shown in Fig. 23b, appears to be significantly lower compared with the CHF at 30 °C saturation, as its value reduces around 7.7% – 9.7 % with high inlet subcooling and high mass flux. Meanwhile, for the case of R1234yf, the results in Fig. 24b show a smaller saturation temperature effect compared to R134a. Consequently, the footprint CHF reduces by around 2% – 5.8% with low inlet subcooling.

5.1.2. EFFECT OF INLET RESTRICTION

To assess the effect of the absence of inlet restriction in the present investigation, Fig. 25a and 25b indicate the obtained footprint CHF results with and without the inlet restriction at different inlet subcooling and the various mass fluxes (320 – 1200) kg/m^{2}s at saturation temperature 30 °C with R134a. The effect of inlet restriction either increases or decreases the CHF depending on the geometry, but in all cases the variation is no more than 4%. The relative contribution of the orifices to the CHF is displayed in Fig. 25c which presents the ratio between CHF without and with orifices versus mass flux. In the case of geometry C, the CHF consistently decreases if no orifices are used. At the midrange mass flux, the reduction is less (<2 % at low subcooling) and increases slightly as the mass flux is further increased. On the other hand, the CHF increases by around 4% without the inlet restriction with geometry H, but at the highest mass flux, it becomes insignificant, or even reduces around 4% for high inlet subcooling. Similarly, when no inlet restrictions are used, the CHF with geometry G increases up to 6% from the mid to high-mass flux range for low inlet subcooling, but the increase becomes insignificant at the highest mass flux in the case of high subcooling. The general trends indicate the effect of subcooling at high mass fluxes when inlet restrictions are used.

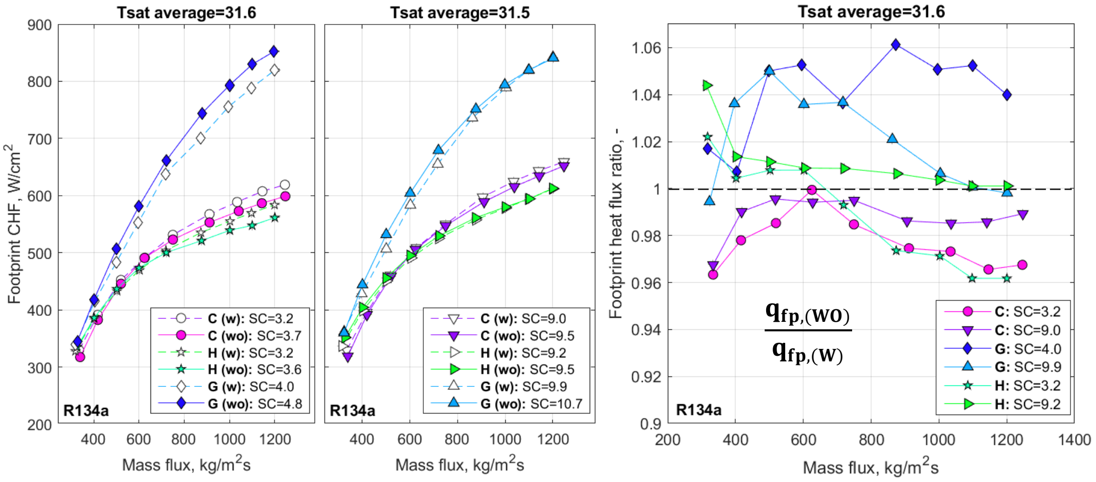

(a) (b) (c)

Fig. 25. Footprint CHF vs. mass flux for R134a (a) at saturation temperature 31.6 °C with (W) and (b) 31.5 °C without (**WO**) orifices and (c) the normalized footprint CHF (**WO/W**) vs. mass flux for R134a. The average subcooling (SC) in K indicated for each curve concerning geometry C, H, and G.

5.1.3. EFFECT OF INLET SUBCOOLING

Fig. 26a – c shows the footprint CHF with R134a as a function of the inlet subcooling for several mass fluxes in the range of 320—1200 kg/m^{2}s at 30°C saturation temperature, and Fig. 26d – f at 40°C saturation temperature. As mentioned in Section 5.1.1, there is an evident effect of inlet subcooling on the footprint CHF. In the case of R134a, high inlet subcooling consistently increases the footprint CHF with geometry H and C, and its effect reduces significantly at low mass fluxes. Meaning that at nominal mass flux 320 kg/m^{2}s, the CHF increase is 0% – 4%, while 9% – 10% at nominal mass flux 1200 kg/m^{2}s with geometry C. Similar results are obtained with geometry H, where Fig. 26b and 26e show an increase of 5% – 6% at the lowest mass flux, and a 9% – 10% increase at the highest. For Geometry G, the CHF is more sensitive to subcooling at low mass fluxes increasing around 4% – 6.5%, but the subcooling effect at high mass fluxes becomes insignificant.

On the other hand, the results with R1234yf presented in Fig. 27a – c and 27d – f show a slight improvement of the inlet subcooling effect compared to R134a. The CHF increase with geometry C is 3% – 6% with the lowest mass flux, and 7% – 11% with the highest. Geometry H presents an increase around 6% with 320 kg/m^{2}s, and around 10% with 1200 kg/m^{2}s. And similarly, as in the case of R134a, the subcooling effect with geometry G becomes negligible with high mass flux, while at the lowest has an increase of around 6%. Consequently, with both working fluids, an increase in inlet subcooling leads to a footprint CHF increase with geometry H and C, and its effect increases with mass flux increase. Interestingly, the opposite trend is found with geometry G, where the subcooling effect becomes insignificant at low high mass fluxes.

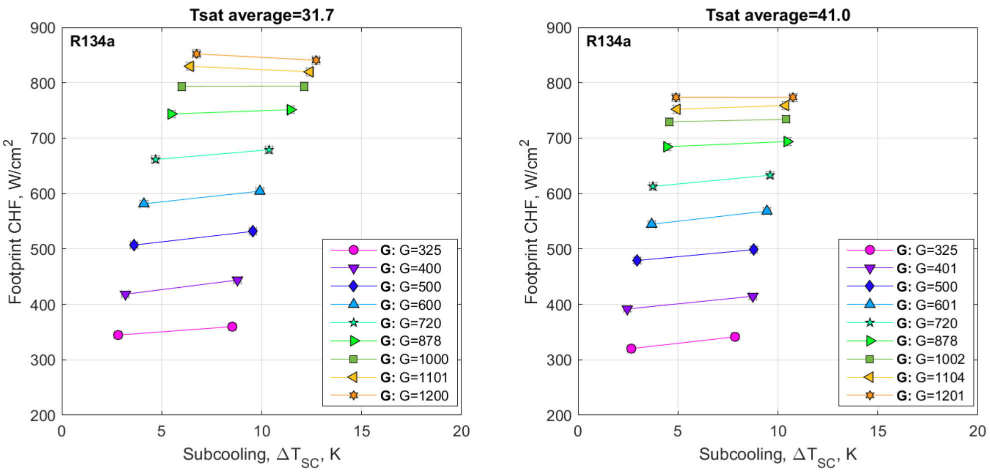

(a) Geometry G

(d) Geometry G

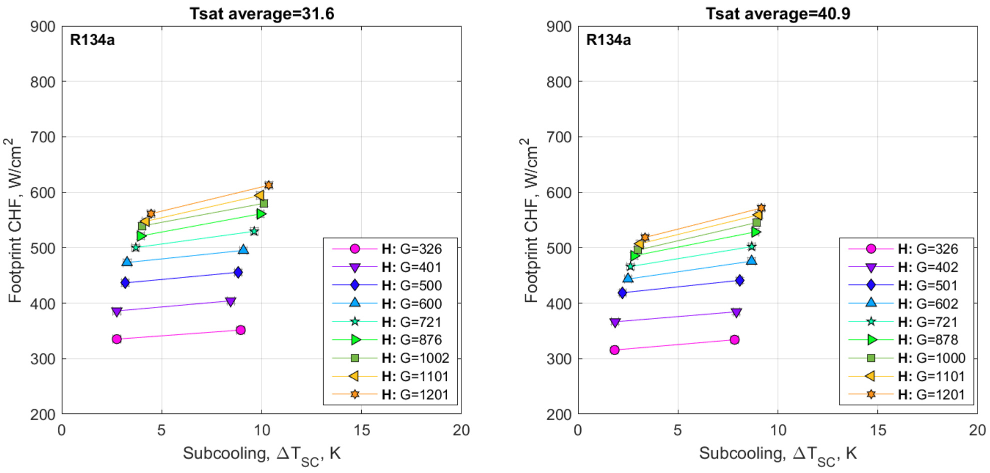

(b) Geometry H

(e) Geometry H

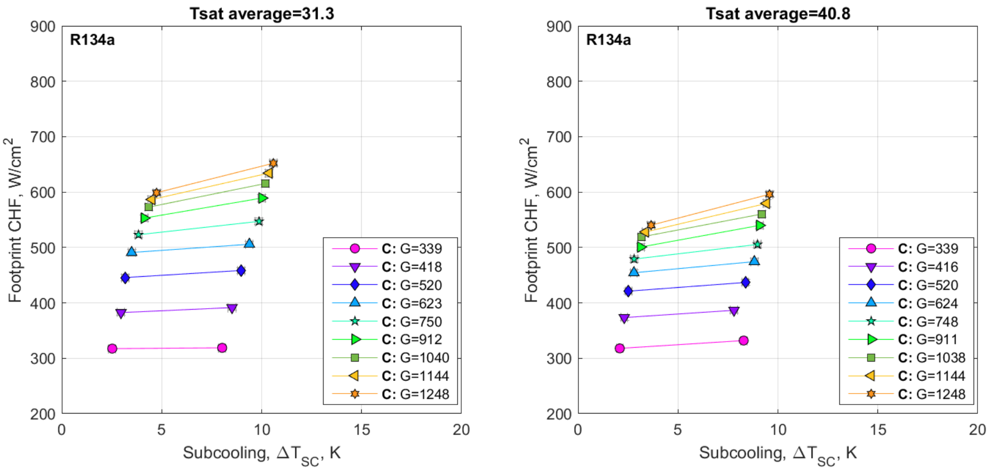

(c) Geometry C

(f) Geometry C

Fig. 26. Footprint CHF vs. inlet subcooling for R134a at nominal saturation temperature of 30°C (a) for geometry G, (b) H, (c) and C, and at 40°C for geometry (d) G, (e) H, (f) and C.

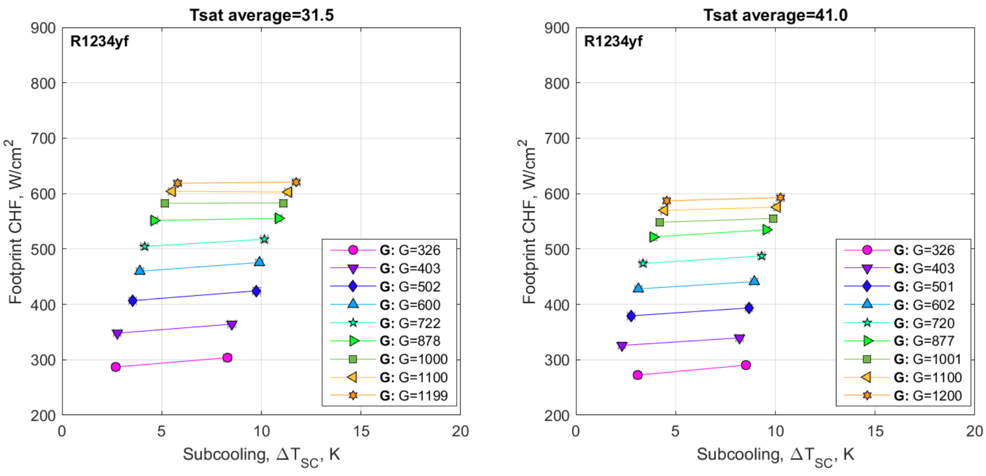

(a) Geometry G **(d)** Geometry G

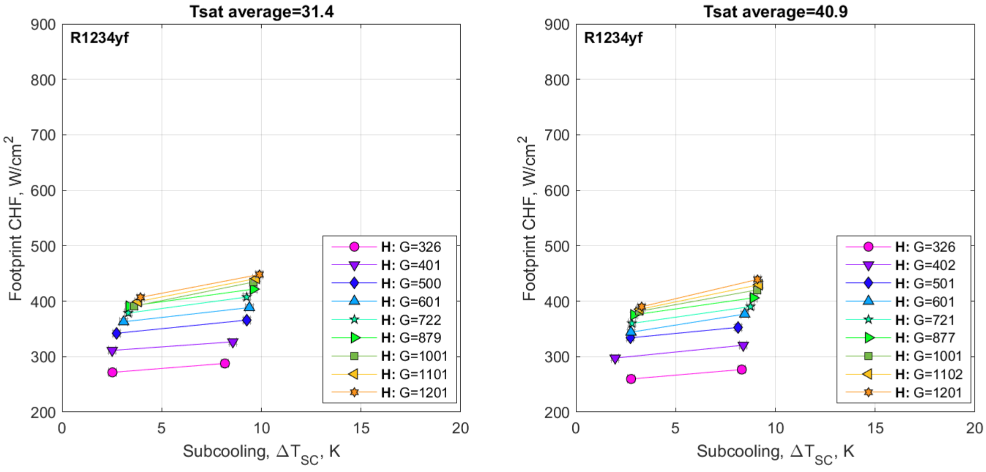

(b) Geometry H **(e)** Geometry G

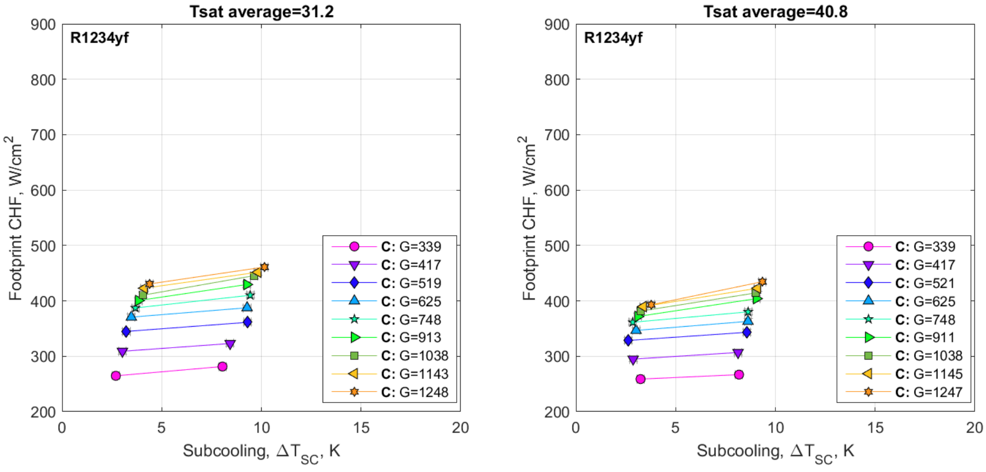

(c) Geometry C **(f)** Geometry G

Fig. 27. Footprint CHF vs. inlet subcooling for R1234yf at nominal saturation temperature of 30°C (a) for geometry G, (b) H, (c) and C, and at 40°C (d) for geometry G, (e) H, (f) and C.

5.1.4. EFFECT OF FLUID AND SATURATION TEMPERATURE

The effect of the saturation temperature on the footprint CHF is shown in Fig. 28a and 28b which present the footprint CHF at nominal saturation temperatures of 30 °C and 40 °C versus the mass flux with R134a. Fig. 29a and 29b present the same results with R1234yf. For both working fluids, the increase of saturation temperature consistently resulted in a decrease of the CHF at a constant mass flux. In the case of R134a, the effect of the saturation temperature was slightly higher for lower inlet subcooling, meaning that with an average inlet subcooling of 3.6 °C, the CHF reduced more when increasing the saturation temperature from 30 °C to 40 °C. The ratio between the CHF with 30 °C and 40 °C saturation temperature versus mass flux is presented in Fig. 28c. The CHF reduction is no more than 10% for all cases in terms of percentage. In the region of high mass fluxes, the reduction is more significant while it was slightly lower in the low-mass-flux region, except for some discrepancies in geometry C at the lowest mass flux.

Fig. 29c presents the CHF ratio versus mass flux with R1234yf. In this case, R1234yf showed a smaller CHF reduction compared to R134a. The inlet subcooling appeared to have no clear effect on the CHF reduction caused by an increase in saturation temperature, showing a small oscillation in the variation between the two subcooling levels. The reduction exhibited in the CHF when increasing the saturation temperature was around 4.5%, 2%, and 5.8% for geometry G, H, and C with R1234yf. Consequently, the effect of saturation temperature was consistently smaller with geometry H with both working fluids.

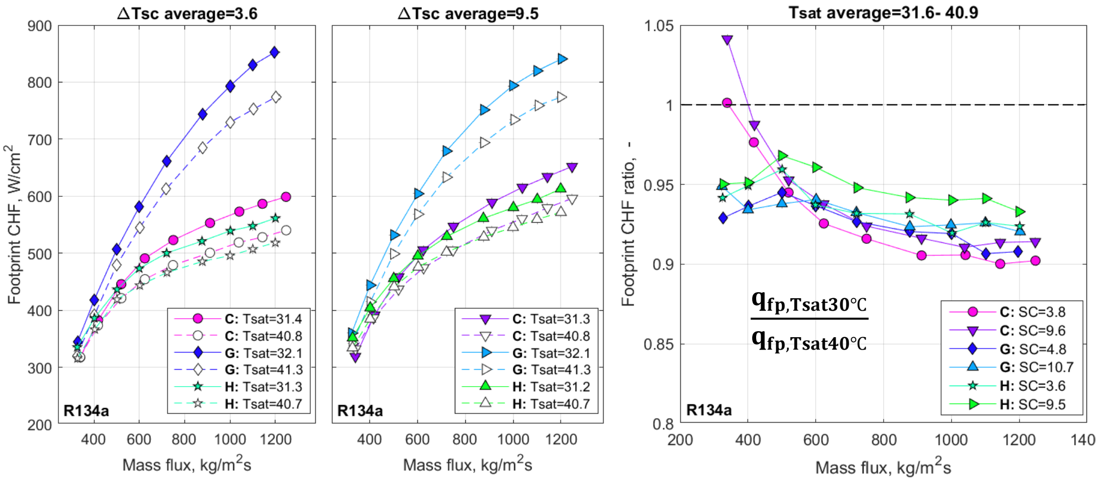

(a) **(b)** **(c)**

Fig. 28. The effect of saturation temperature on footprint CHF vs. mass flux with R134a (a) for average subcooling 3.6 K and (b) average subcooling 9.5 K, and (c) the normalized footprint CHF vs. mass flux for R134a.

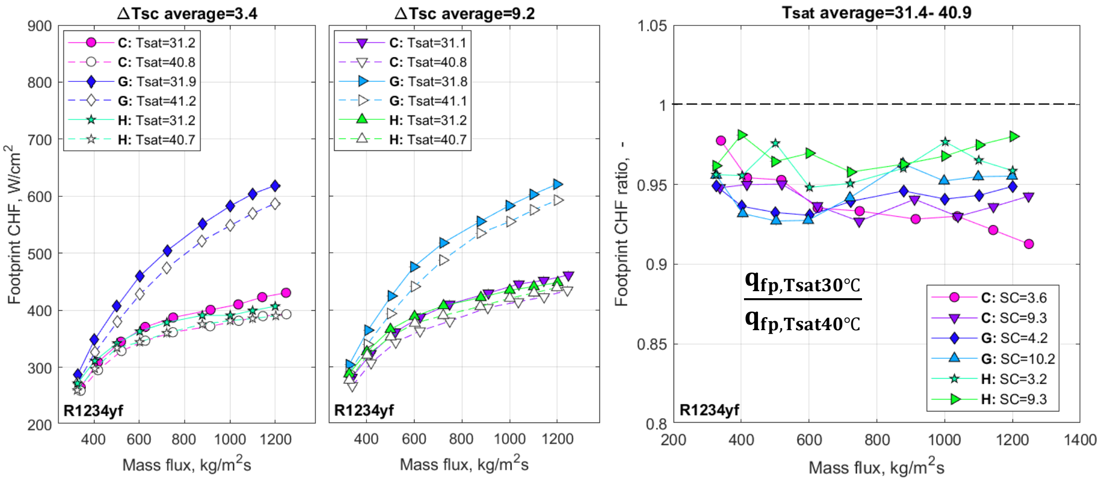

(a) (b) (c)

Fig. 29. The effect of saturation temperature on footprint CHF vs. mass flux with R1234yf (a) for average subcooling 3.4 K and (b) average subcooling 9.2 K, and (c) the normalized footprint CHF vs. mass flux for R1234yf.

The comparison results between the CHF obtained with R134a and R1234yf versus mass flux at saturation temperature 30 °C are presented in Fig. 30a and 30b. In general, while there is no substantial difference in the CHF at the low-mass-flux region, the difference becomes significantly evident at high mass fluxes. Consequently, the traditional R134a indicates better performance as a cooling fluid. Fig. 30c shows the CHF ratio between R134a and R1234yf versus mass flux. Concerning the percentage difference, the increase of CHF with R134a compared to R1234yf tends to be higher with low inlet subcooling, although this is not consistent at all mass fluxes. In the case of geometry C, the CHF at saturation temperature 30°C increased around 41% with R134a at the highest mass flux. On the other hand, the increase with R134a was similar to geometry H and G, increasing around 41% compared to R1234yf.

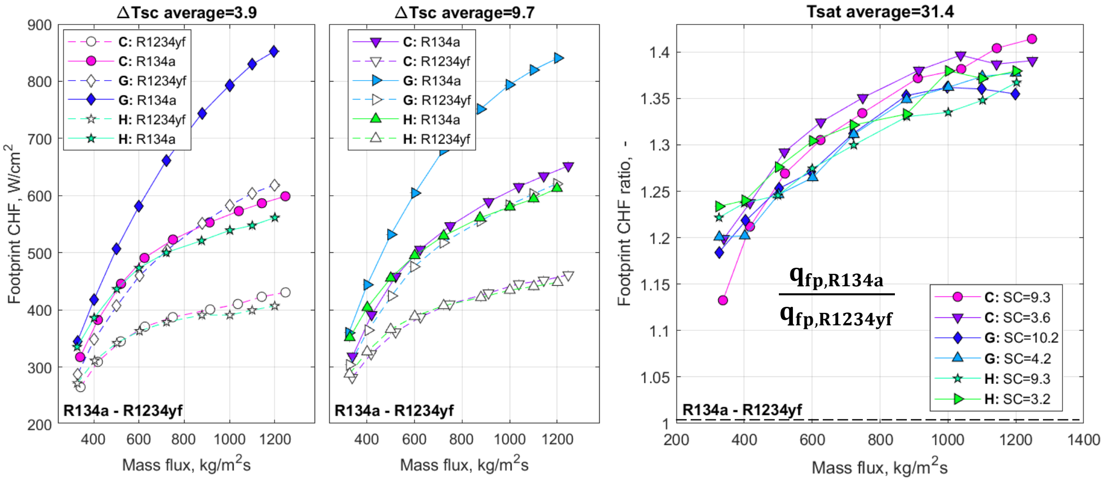

(a) (b) (c)

Fig. 30. The effect of fluid on footprint CHF vs. mass flux with 31.4 °C average saturation temperature (a) for average subcooling 3.9 K and (b) average subcooling 9.7 K, and (c) the normalized footprint CHF vs. mass flux for R134a.

5.1.5. DISCUSSION

The increase of the footprint CHF with mass flux in Fig. 23 and 24 is consistent with previous findings [32],[29],[28],[19]. The high CHF obtained with geometry G could be attributed to the combination of the higher heat transfer surface area, and the breakup and reattachment of the boundary layer caused by the high shear stresses, high turbulence, and secondary flows due to channel corrugation, eventually diminishing the likelihood of dryout. The experimental trend suggests the footprint CHF could furtherly be increased, potentially leading to values close to 1000 W/cm^2, however, additional experiments at very high mass fluxes are needed to corroborate this experimental trend. Interestingly, in Fig. 23a under the same condition of the same mass flux, the footprint CHF the Geometry H was slightly higher than in geometry C in the low-mass-flux region. This result follows previous findings by Fu et al. [16] who suggest the footprint CHF increases with the hydraulic diameter since the area enhancement concerning the footprint is larger for geometry H due to the thinner separating walls at the outlet of the microchannels. However, at higher mass fluxes from (600-1200) kg/m^{2}s, geometry H achieves a lower footprint CHF despite its enhanced area which is counter-intuitive with the monotonous CHF increase due to the bigger heat transfer area. Previous analysis with the same geometry but with inlet restriction found the same results on the footprint CHF [1]. Fu et al. [16] might have not observed this effect in their experimental investigation at very low mass fluxes (up to 180 kg/m^{2}s), and a deeper study on the limits on CHF with diverging channels could provide interesting information from the design point of view of cooling systems.

From the saturation temperature perspective, the reduction in the footprint CHF with increased saturation temperature in Fig. 28 and 29 is in accordance with the experimental results found by Criscuolo [10] and Kærn [19] who suggest the saturation temperature increase may enhance the presence of dryout as both the surface tension and the heat of vaporization are decreased causing the CHF to decrease. For instance, as shown in Table 5.5, in the case of R134a, increasing the saturation temperature from 30 °C to 40 °C causes an increment in the vapor-to-liquid density ratio $\rho_\mathrm{v}/\rho_\mathrm{L}$ (from 0.03 to 0.04) which stabilizes the flow by reducing the gap between the liquid and vapor phase. This agreed with several correlations that expect an increase in the CHF with an increase of $\rho_\mathrm{v}/\rho_\mathrm{L}$ [52],[36],[2]. However, the latent heat of vaporization h_{lv} decreases (from 171.5 to 162.0 kJ/kg), and the surface tension reduction σ (from 7.1 to 6.0 mN m^{-1}) overcomes these effects resulting in a lower CHF. Mauro and Thome's [29] suggestion that the two opposite effects may lead to either an increase or decrease of the CHF, implying the existence of an optimal saturation temperature (peak in CHF) could be aligned with the results obtained in this experimental investigation. It is important to notice that a concrete conclusion cannot be made since the range of saturation temperature in the present study was not big. In a recent study, Dalkılıç [12] found that no specific peak point was reached in their experimental investigation varying the saturation temperature. Consequently, a deeper investigation of a wider range of saturation temperatures is required to conclude the existence of the peak or its absence with the present geometries and experimental conditions in this work.

Table 5.5. Fluid properties for different reduced pressure for R134a and R1234yf.

Fluid	T_{sat} [°C]	P_r [−]	h_{lv} [kJ/kg]	ρ_v/ρ_L [−]	σ [mNm^{-1}]
R134a	31.6	0.19861	171.55	0.0333	7.175
	40.9	0.25654	162.06	0.0449	6.003
% Divergence			- 5.5%	+35%	16.3%
R1234yf	31.4	0.24057	140.04	0.0426	5.397
	40.9	0.30804	131.41	0.0575	4.302
% Divergence			- 6.2%	+34.9%	-20.3%

Since there is a connection between the fluid properties and the effect of the saturation temperature, the CHF with R134a and R1234yf is affected differently by the increase in saturation temperature from 30 °C to 40 °C, as shown in Fig. 28 – 29. This could be related to the influence of the reduced pressure P_r [29] as shown in Table 5.5. On the basis that a peak CHF exists, the increase in saturation temperature with R134a could have been beyond the corresponding value to the peak CHF, while R1234fy might have been slightly closer to the peak, resulting in less sensitivity to changes in saturation temperatures over R134a. Another aspect to consider is the effect of fluid properties on the CHF shown in Fig. 30. R134a depicted the highest CHF at a saturation temperature of 30 °C compared to R1234yf for a given mass flux. While the vapor-to-liquid density ratio ρ_v/ρ_L is 27% lower for R134a, the latent heat of vaporization h_{lv} is 18% higher compared to R1234yf at 30 °C saturation temperature, as shown in Table 5.6. Consequently, it could be that the higher footprint CHF with R134a is mainly analogous to the difference in the latent heat of vaporization with the other fluid, which is in line with several correlations proposed.

Table 5.6. Fluid properties at saturation temperature of 30 °C.

Fluid	P_r [−]	h_{lv} [kJ/kg]	ρ_v/ρ_L [−]	σ [mNm^{-1}]	ρ_v [kg/m^3]
R134a ($T_{sat} = 30$°C)	0.19861	171.55	0.0333	7.175	39.3
R1234yf ($T_{sat} = 30$°C)	0.24057	140.04	0.0426	5.397	45.5
% Difference		+18.4%	-27.9%	-32.9 %	-15.8%

The effect of inlet subcooling on Fig. 26 and 27 with geometry C and H is consistent with past results [19],[24],[32], which is found to be significant at high mass fluxes. This could be attributed to the increase in the importance of the enthalpy change Δh_{sub} in the inlet plenum (subcooled region) concerning the enthalpy change $h_{fg}x_{cr}$ in the two-phase region inside the channels at higher mass fluxes (Critical vapor quality x_{cr} reduces with increasing mass flux) leading to a CHF increase [19]. On the other hand, the negligible inlet subcooling effect with Geometry G reflects the results of other investigations [2],[32], but a direct comparison is difficult to make due to the corrugation and different separating wall thickness. One possible explanation for the decreasing effect of inlet subcooling at high mass fluxes could be explained by the higher void fraction found in geometry G. At the highest mass flux, the critical vapor quality x_{cr} for Geometry G is around 0.6, much higher compared to geometry H and C, with a vapor quality around 0.4 – 0.45. The high vapor void fractions along the channels combined with the larger pressure drop could result in higher resistance to the inlet liquid momentum causing flow instabilities, and the reduction of the subcooling effect even at high mass fluxes. An analysis of high-speed camera footage shown in Fig. 31 reveals oscillations in the annular flow between channels suggesting the presence of instabilities occurring at high mass fluxes. Previous results with geometry G using inlet restriction to aid flow stabilization also revealed such oscillation even at the highest mass flux [1]. Another possible explanation is that the high mixing and secondary flows in the wavy channels could lead to a quick mixture of the vapor phase with the incoming subcooled liquid, bringing its temperature quickly to the saturation one, thus eliminating the subcooling effect. As shown in Fig. 32a-b, an analysis of the IR thermal maps of the heat sinks reveals a more uniform temperature distribution between RTDs for the geometry G, however, this was not the case with the other test samples that show a higher temperature gradient. Likewise, the temperature gradient with geometry G was higher at low mass flux, as shown in Fig. 32c, mirroring the trend of the subcooling effect. Hence, the very high heat fluxes obtained at high mass fluxes coupled with the flow mixing in the channels could be a reasonable conclusion for the negligible subcooling effect with geometry G at high mass fluxes.

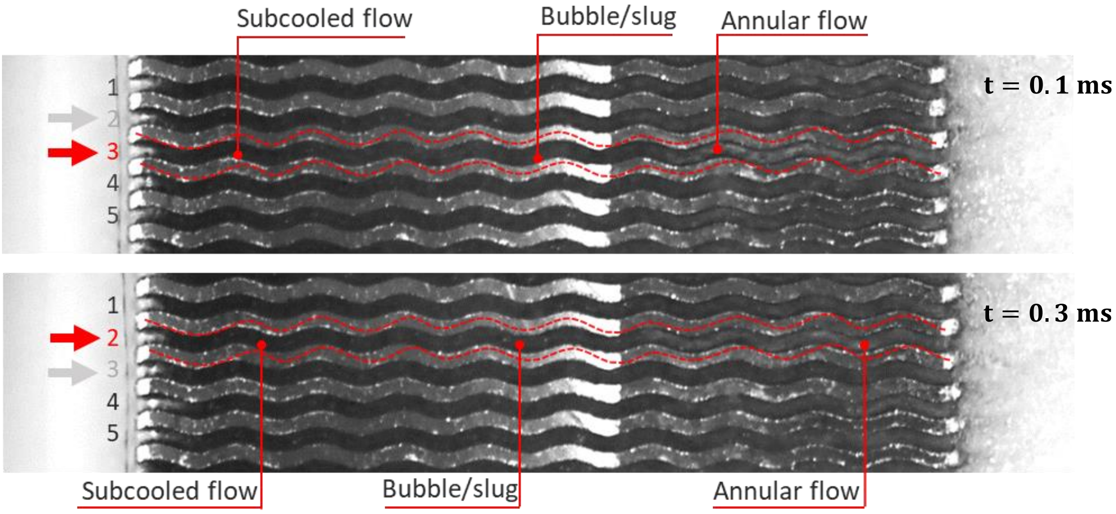

Fig. 31. High-speed flow images for geometry G at 1200 kg/m^2 with R134a showing the annular flow alternation between channel 3 (top) and channel 2 (bottom).

Accordingly, the liquid inertia at high mass velocities might not be enough to overcome the instabilities inside the channels, thus explaining the insignificant subcooling effect. Further analysis of the pressure drop of geometry G is discussed in Section 5.4.

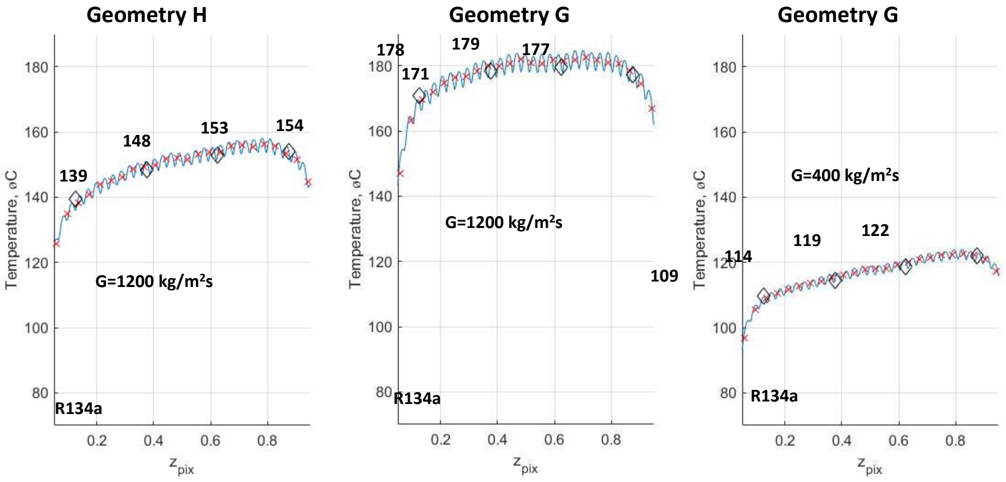

(a) (b) (c)

Fig. 32. Flow-wise temperature profile at nominal mass flux of 1200 kg/m^{2}s for (a) geometry H, (b) geometry G, and (c) at 400 kg/m^{2}s geometry G with R134a at nominal saturation temperature of 30 °C.

5.1.6. SUMMARY

The analysis presented in this section highlighted the effect of the mass flux, saturation temperature, the inlet subcooling level, and fluid properties on the footprint CHF with R134a and R1234yf, for three geometries with different characteristics. The highest CHF in the experimental investigation was obtained with geometry G, and CHF with R134a was higher in all test conditions due to its higher latent heat of vaporization. The saturation temperature reduces the CHF, and the effect is slightly more prominent with R1234yf. The effect of subcooling is evident in geometry C and H, while it was negligible in geometry G. This was attributed to the high mixing in the channels. Finally, the effect of inlet restriction to minimize the flow instability revealed a positive effect for geometry C, but for the other solutions, the CHF increased when no inlet restrictions were used.

5.2. WALL CHF

The previous section presented the analysis of the CHF at the footprint or base level. While these results are useful for cooling system applications on power electronics, since they evaluate the overall cooling performance on the heat sink, the wall CHF reflects the effective heat flux dissipated on the wetted perimeter of the microchannels. The results presented in this section consider the effect of the fin efficiency, as proposed in the data reduction in Section 4.1.4.

The following section presents the results of the wall CHF and the detailed analysis of the effect of the different aspect ratios, hydraulic diameter, and other aspects caused by the wall geometry of the expanding and corrugated channels versus the straight ones.

5.2.1. WALL CHF RESULTS

To reflect the effects of the channel dimensions on the CHF, Fig. 33a and 33b present the comparison of the channel wall CHF versus the mass flux for nominal saturation temperatures 30 °C and 40 °C with R134a with different sub-cooling in the mass velocity range of 320—1200 kg/m^{2}s. Fig. 34a and 34b present the same results with R1234yf. The wall CHF significantly increases with increasing mass flux, which is in agreement with correlations for CHF in the literature on the flow boiling in microchannels. While the wall CHF increased with mass velocity, its rate of increase was less at higher mass fluxes. The wall CHF with geometry H and C increased moderately with increasing inlet subcooling. However, no significant inlet subcooling effect was observed with geometry G. As presented in section 5.1.4., increasing the saturation temperature from 30 °C to 40 °C decreases the wall CHF with both fluids. The highest wall CHF was achieved with geometry G, followed by geometry H, and C using the traditional refrigerant R134a. Consequently, in the case of R134a at 30 °C saturation temperature, the highest wall CHF obtained with geometry G is 197 W/cm^2, with geometry H is 138.7 W/cm^2, and with geometry C 139.6 W/cm^2 at 1200 kg/m^{2}s with 10 K average subcooling. While the highest CHF with R1234yf and geometry G is 146.3 W/cm^2, for geometry H is 101.9 W/cm^2, and 101.1 W/cm^2 for geometry C.

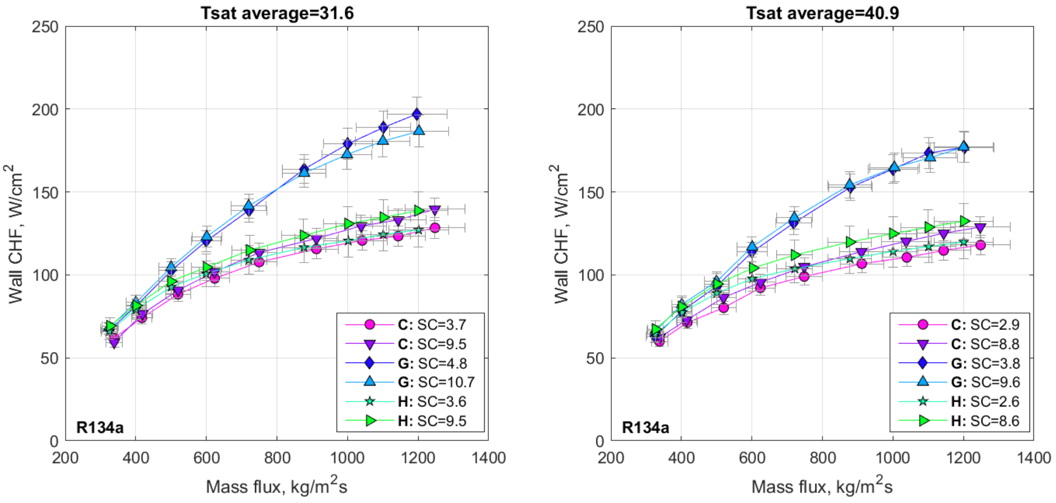

(a) **(b)**

Fig. 33. Wall CHF vs. mass flux for R134a. The average saturation temperature was 31.6 °C (a) and 40.9 °C (b). The average subcooling (SC) in K indicated for each curve with respect to geometry C, H, and G.

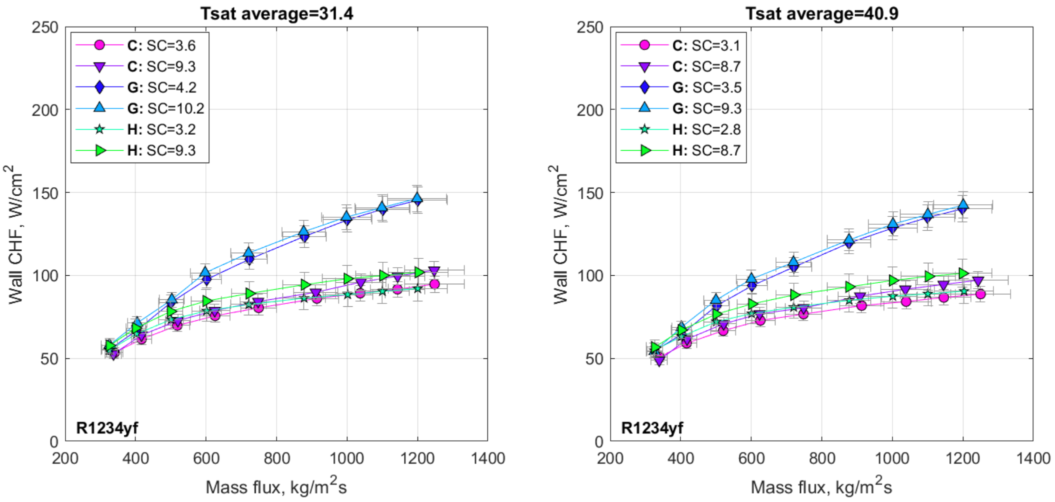

(a) **(b)**

Fig. 34. Wall CHF vs. mass flux for R1234yf. The average saturation temperature was 31.4 °C (a) and 40.9 °C (b). The average subcooling (SC) in K indicated for each curve with respect to geometry C, H, and G.

5.2.2. DISCUSSION

The results in Fig. 33a-b and 34a-b reflect the effect of the main parameters studied before. The increase in saturation temperature decreases the wall CHF with both working fluids, the highest wall CHF is obtained with R134a, and the inlet subcooling increases slightly the wall CHF with geometry C and H, while its effect is negligible with geometry G. The detailed analysis of these parameters is presented in section 5.1.5. Henceforward, the effect of the channel geometry is discussed in the present discussion. In the case of geometry H, Fu et al. [16] found an increase of up to 16% in the wall CHF in their experimental investigation when comparing uniform microchannels with diverging ones at the same hydraulic diameter. As shown in Fig 33b and 34b, the wall CHF was slightly higher compared to geometry C with a saturation temperature of 40 °C, increasing up to 15% at the mid-mass-flux region, while with a saturation temperature of 30 °C, Fig. 33a and 34a show that the increment was notable at low mass fluxes but decreasing at high ones. This is aligned with the experimental results found by Fu with his diverging microchannels where the CHF increase was higher, especially at low mass fluxes.

Table 5.7. Channel dimensions for geometry C, H, and G.

Geometry	W_{ch} $[\mu m\,]$	H_{ch} $[\mu m]$	W_{fin} $[\mu m]$	D_h $[\mu m]$	L_h/D_{he} $[-]$	H_{ch}/W_{ch} $[-]$	N $[-]$
C $(straigth)$	198	1167	200	338	29.5	5.89	25
H $(diverging)$	200 – 340*	1200	200 – 60*	343	22.2	6.0 – 3.53*	25
G $(wavy)$	200	1200	200	338	29.5	5.89	25

* Indicates that the values correspond to inlet and outlet of the channels, respectively.

The higher wall CHF with diverging channels was attributed by Prajapati et al. [33] to the stabilizing effect of the steep pressure gradient near the inlet in the diverging microchannel. Consequently, the flow stability enhancement on the two-phase flow could partly explain the increase in the wall CHF in the present investigation. It is important to mention that Fu's [16] findings were under the condition of the same hydraulic diameter. Here, part of the increase in the wall CHF with geometry H is related to the higher hydraulic diameter, as shown in Table 5.7. Indeed, previous studies and correlations in the literature expect an increase in the wall CHF with increasing heated equivalent diameter. Additionally, the relationship between the hydraulic diameter and the aspect ratio, affected by the decrease in the wall thickness of the diverging channel at the outlet section, could play a role in the wall CHF increase as well. Choi [9] demonstrated that a decrease of AR (AR<1) leads to thinner liquid film in the corners of the microchannels. Later, Fu et al. [16] would extend the concept to AR >1, meaning that the liquid film decreases due to the confinement effect when the AR is higher. Fig. 35 shows how the AR effect on the expanding channels could also affect the wall CHF increase since the main CHF mechanism attributed to microchannels with high AR is dryout of the liquid film layer.

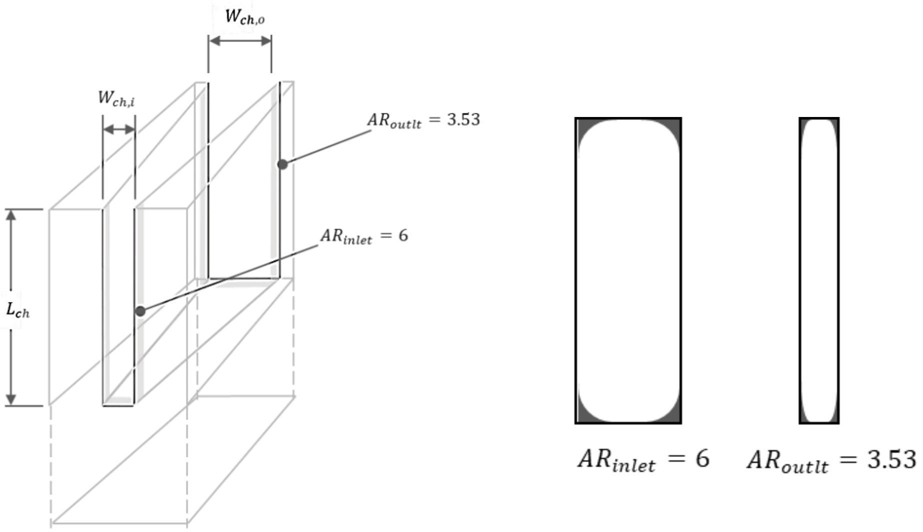

Fig. 35. Illustration of the effect on the liquid film due to the different AR ratios in geometry H.

In the case of geometry G, the higher wall CHF achieved compared to both geometry H and C is believed to be the result of the area enhancement and the continuous developing liquid film layer caused by the corrugated wall. The area enhancement of geometry G with respect to geometry C is represented by equation 20. While there is extensive literature concerning one-phase flow in corrugated microchannels, the studies performed with a two-phase flow are scarce. In terms of percentage, the increase with geometry G compared to C is significantly higher at high mass fluxes, up to 54 % with R134a and 58% R1234yf. The experimental investigation by Xia [51] demonstrated that bubble nucleation tends to occur in the corner regions of the microchannels, which store more liquid for evaporation. Consequently, the study concluded that due to the coupled effect of the stored liquid in corner regions and the continuously developing liquid film, the partial dryout can be prevented. While the analysis with the high-speed camera did not reveal the nucleation in the corner regions, the constant developing liquid film layer could be detected, indicating that the high CHF achieved in the present study is well explained by these conclusions.

5.2.3. SUMMARY

The higher wall CHF obtained with geometry H is attributed to the smaller hydraulic diameter and the pressure gradient at the inlet that could help to stabilize the two-phase flow inside the channels. The different aspect ratios could play a role in the wall CHF increase revealed in the experimental results. The significant increase in the wall CHF with geometry G is believed to be a combination of the area enhancement and the continuous developing liquid film layer caused by the corrugated wall, preventing the dryout and increasing the CHF.

5.3. CRITICAL VAPOR QUALITY

This section presents the relationship between the CHF and the vapor quality at the outlet of the channels (referred to as critical vapor quality). The investigation results are followed by a discussion of the major findings and a summary.

5.3.1. RELATIONSHIP BETWEEN CRITICAL VAPOR QUALITY AND CHF

Fig 36a and 36b present the wall CHF versus the critical vapor quality with different inlet subcooling at 30 °C and 40 °C saturation temperatures, respectively for R134a. Fig. 37a and 37b present the same results for R1234yf. The critical vapor quality increases with higher wall CHF for both working fluids, and the experimental points tend to collide into a single curve at very low wall CHF (low mass flux). In terms of saturation temperature increase, the critical vapor quality change is insignificant when increasing from 30 °C to 40 °C saturation temperature with both fluids. In the case of R134a, Fig. 36 reveals that the inlet subcooling decreases the critical vapor quality, and thus decreases the annular-to-dryout transition with geometry C and H, however, the opposite is found with geometry G. Generally, the critical vapor quality at constant wall CHF is lower for geometry C compared to geometry H, meaning that the diverging microchannels could operate at slightly higher outlet vapor quality x_{out} than the straight ones. For the highest corresponding wall CHF (high mass flux), the critical vapor quality is around 0.42 for geometry H, 0.45 for geometry C, and 0.6 – 0.65 for geometry G at a saturation temperature of 30 °C. However, at the lowest corresponding wall CHF (low mass flux), the critical vapor quality is 0.97 for geometry H, 0.92 – 0.96 for geometry C, and superheated (x_{out}>1) for geometry G. On the other hand, the critical vapor quality with R1234yf shown in Fig. 37 has lower values at constant wall CHF compared to R134a. These values are 0.35 – 0.37 for geometry H, 0.36 – 0.39 for geometry C, and 0.51 – 0.57 for geometry G at the corresponding highest wall CHF (high mass flux), while the critical vapor quality is around 0.96 for geometry H and C and slightly superheated for geometry G at the lowest corresponding wall CHF (low mass flux). The inlet subcooling with R1234yf has a much significant effect on the critical vapor quality at constant wall CHF, i.e., due to the less steep curve of geometry H, at constant wall CHF of 90 W/cm^2 the critical vapor quality with low subcooling is around 0.40 while at high inlet subcooling it increases around 0.65.

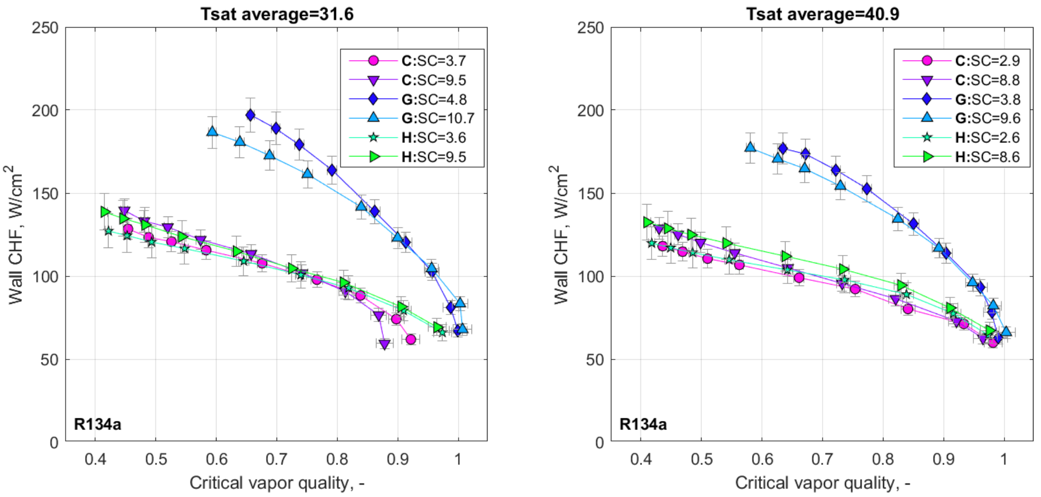

(a) **(b)**

Fig. 36. Wall CHF vs. critical vapor quality with R134a at saturation temperature (a) 31.6 °C and (b) 40.9 °C. The average subcooling (SC) in K is indicated in each curve concerning geometries C, H, and G.

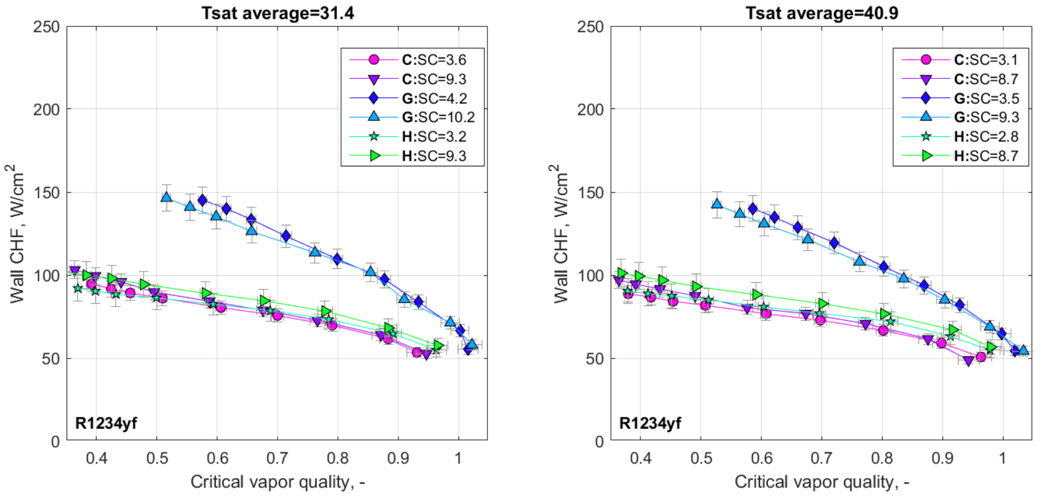

(a) **(b)**

Fig. 37. Wall CHF vs. critical vapor quality with R1234yf at saturation temperature (a) 31.4 °C and (b) 40.9 °C. The average subcooling (SC) in K is indicated in each curve concerning geometries C, H, and G.

5.3.2. DISCUSSION

The experimental investigation by Revellin and Thome [37] presents the critical vapor quality to define annular-to-dryout transition as a function of the outlet vapor quality. As shown in section 4.1.6., equation 31 is obtained from the energy balance under the assumption of uniform heat flux. Consequently, the slight variations in the critical vapor quality with geometry H and geometry C in Fig. 36 and 37 could be the result of the different effective hydraulic diameters, as suggested by Kærn et al. [19]. This analogy is reasonable considering that due to the decrease in wall thickness of the microchannels at the outlet section, the local flow velocity is reduced causing a higher residence time of the flow inside the channels and intensifying the generation of vapor. This is particularly true for R1234yf, while R134a at saturation temperature of 30 °C showed a negligible difference between both geometries. On the other hand, it can be concluded that the CHF and critical vapor quality are the highest for geometry G compared to the straight and diverging channels which are expected according to equation 31. The decrease of the critical vapor quality with increasing wall CHF is aligned with the results of Qi [35], who found that the critical mass quality decreased with the increase of mass flux. The comparison of the results in Fig. 36a-b and 37a-b with Qi's conclusion is possible since, in the present work, low wall CHF values correspond to low mass fluxes, and high wall CHF to higher mass fluxes, as shown in section 5.2.1. According to Qi, high mass flux may be prone to tear the liquid film in the annular flow inside the microchannels, resulting in a CHF at low critical vapor quality. In an experimental investigation by Revellin and Thome [37], the experimental flow pattern map was integrated with equation 31, showing that their experimental results corresponded inside the annular flow region, close to the annular-to-dryout transition. Here, the analysis with a high-speed camera revealed that at high mass fluxes, the flow pattern in the outlet of the microchannels was characterized by annular flow, indicating the presence of a thin liquid film layer and that the CHF mechanism was governed by dryout. This validates the conclusion by Qi, stating that high mass fluxes could tear the liquid film explaining the low critical vapor quality at high wall CHF. It is important to mention that as stated by Agostini et al. [2] and Pribyl [34], at very high mass fluxes, a different flow transition might occur, i.e., bubbly-to-dryout instead of annular-to-dryout. These results were not observed in the mass velocity range (320 – 1200) kg/m^{2}s employed in the current investigation. However, detailed analysis and additional experimental measurements might be required to make a reliable conclusion.

An important discrepancy is observed in Fig 36a in the low-mass-flux region for geometry C, where the curve becomes suddenly steeper, consequently resulting in lower critical vapor quality. This could be the result of the methodology used to determine the CHF point in the experimental setup. The CHF is detected when the response in the RTDs is of a second-order, indicating a steep increase in the wall temperature and eventually triggering the safety system of the power supply. Nonetheless, at very low mass fluxes, such a response might be never obtained allowing a further increase in the heat flux, and the heat transfer coefficient deteriorates further and further. In this condition, the CHF is conventionally assigned when the outlet thermocouple detects the bulk flow temperature higher than the saturation one, meaning that superheated vapor is found at the outlet of the microchannels, and the experimental point is measured. The discrepancy in Fig 36a could be explained by the convention applied to define the CHF, and the solution to the latter would be to push the experimental setup to trigger the steep increase in the wall temperature.

The lower values of critical vapor quality found in Fig 37a and 37b with R1234yf compared to R134a are believed to be the result of the lower wall CHF with R1234yf compared to R134a results. While the latent heat of vaporization h_{lv} for R1234yf is around 18.4% lower at a saturation temperature of 30 °C, as presented in Table 5.6, the wall CHF is 26% compared to R134a at the highest mass flux. The lower latent heat of vaporization h_{lv} increases the critical vapor quality, but this effect is overcome by the much lower wall CHF, resulting in a decrease in the critical vapor quality compared to the case of R134a. Thus, the traditional R134a presents a higher limit for the outlet vapor quality before the annular-to-dryout transition occurs.

5.3.3. SUMMARY

The critical vapor quality decreases with increasing wall CHF. The higher mass flux corresponding to the high wall CHF values could tear the liquid film in the annular flow resulting in CHF with a lower critical vapor quality, as stated by Qi [35]. The highest wall CHF and critical vapor quality correspond to geometry G. The wall CHF with geometry H is comparable to or slightly higher than geometry C. The slightly higher critical vapor quality achieved with geometry H is believed to be the result of the increase in width in the flow-wise direction that decelerates the two-phase flow enhancing the vapor production. Finally, the different critical vapor qualities with R1234a and R134a are explained by the different latent heat of vaporization, and the wall CHF at a given mass flux.

5.4. PRESSURE DROP

In this section, the results of the pressure drop analysis are presented. While CHF is one of the most important parameters as a limit for the heat flux in cooling systems for power electronics, the pressure drop in two-phase systems has significant importance to achieve sustainable cooling solutions by minimizing the pump size and power consumption.

The section presents the discussion of the effect of the mass flux over the pressure drop and its relationship with the critical vapor quality. Finally, a qualitative analysis of the overall performance of the geometries studied is presented, considering the footprint CHF and the pressure drop as parameters in consideration.

5.4.1. MASS FLUX EFFECT

The pressure drops versus the mass flux with R134a at different inlet subcooling and saturation temperatures of 30 °C and 40 °C are presented in Fig. 38a and 38b. The same results are shown in Fig. 39a and 39b with R1234yf. With both working fluids, the pressure drop increases with the increase of mass flux and higher inlet subcooling systematically reduces the pressure drop at constant mass flux. The subcooling effect is significant with R1234a while less important with R134a, and in all cases, the pressure drop is more affected in the high-mass-flux region, while at the low to mid mass fluxes the inlet subcooling effect on the pressure drop becomes insignificant.

Increasing the saturation temperature from 30 °C to 40 °C produces a reduction in the pressure drop, although this is highly linked to the reduction in the footprint CHF, as discussed in section 5.1.5. In the case of R134a, the pressure drop is steeper compared to R1234yd. The highest value is obtained with geometry G, while geometry H resulted in the lowest pressure drop at both saturation temperatures. The pressure drop ranged from 69 – 550 mbar with geometry, 47 – 271 mbar with geometry C, and 27 – 140 mbar with geometry H for the range of mass fluxes in the experimental investigation (320 – 1200) kg/m^{2}s.

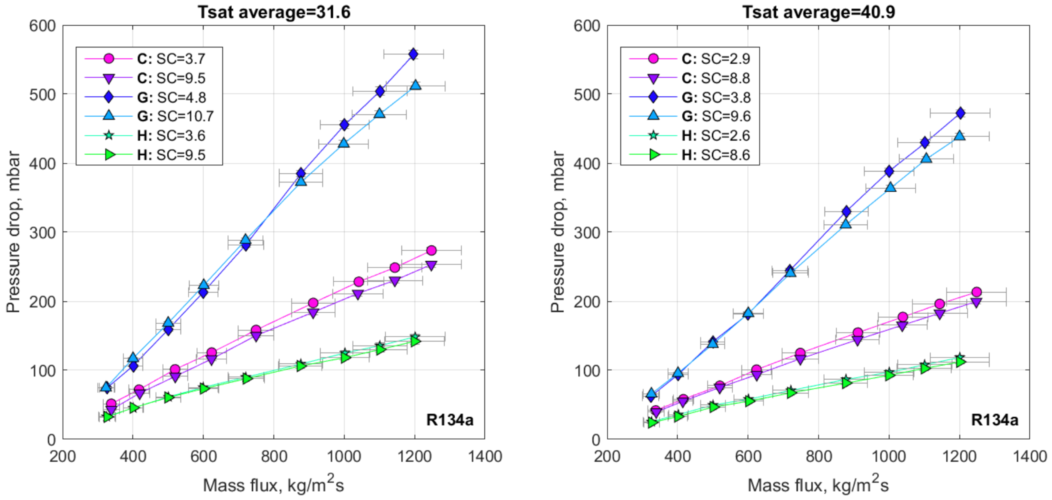

(a) **(b)**

Fig. 38. Pressure drops vs mass flux with R134a, at saturation temperature (a) 31.6 °C and (b) 40.9 °C. The average subcooling (SC) in K is indicated in each curve corresponding geometry C, H, and G.

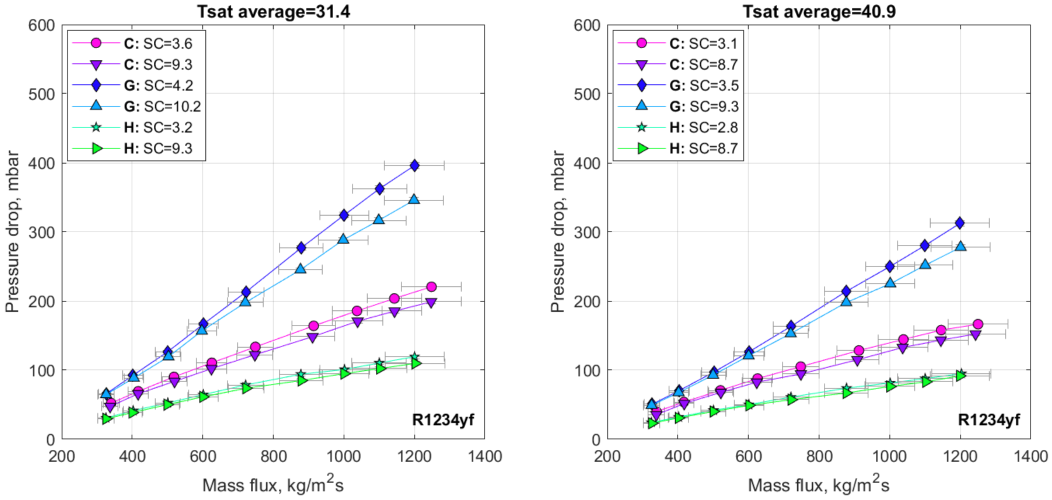

(a) **(b)**

Fig. 39. Pressure drops vs mass flux with R1234yf, at saturation temperature (a) 31.4 °C and (b) 40.9 °C. The average subcooling (SC) in K is indicated in each curve corresponding geometry C, H, and G.

On the other hand, the pressure drop with R1234yf was less steep with an increasing mass flux, as shown in Fig. 39a and 39b. The pressure drops ranged from 67 – 310 mbar with geometry G, 37 – 218 mbar with geometry C, and 26 – 107 mbar with geometry H during the experimental investigation. In both working fluids, while the pressure drop with geometry G and H increases almost linearly with an increase in the mass flux, geometry H has a steeper increase at the low-mass-flux region, but the rate of increase diminishes at high mass fluxes.

5.4.2. PRESSURE DROP AND CRITICAL VAPOR QUALITY

Fig. 40a and 40b show the pressure drop versus the critical vapor quality with R134a at different inlet subcooling with saturation temperatures of 30°C and 40°C, respectively. Similarly, as in the case of the wall CHF, all curves tend to collide into a single region. The results with R1234yf are presented in Fig. 41a and 41b under the same experimental conditions. With both working fluids, the critical vapor quality decreases with increasing pressure drop, but the decrease is steeper with R134a compared to R1234yf. The increase of saturation temperature from 30 °C to 40 °C decreases both the pressure drop and the critical vapor quality, although the reduction in the critical vapor quality is slightly smaller or even negligible in some cases, i.e., for geometry G, the pressure drop decrease is around 21% while the vapor quality reduces less than 2% with an increase in the saturation temperature, with R1234yf at the highest pressure drop. The inlet subcooling decreases the pressure drop and increases the critical vapor quality. In the case of geometry G, the subcooling effect is significant at low critical vapor quality (the mass flux is high), while it becomes negligible at high critical vapor quality (the mass flux is low). On the other hand, the subcooling effect remains slightly significant in the case of geometry C in all the range of the critical vapor quality, while the effect is notably negligible for geometry H. Generally, the highest critical vapor quality and pressure drop are obtained with geometry G, while geometry H presented the lowest.

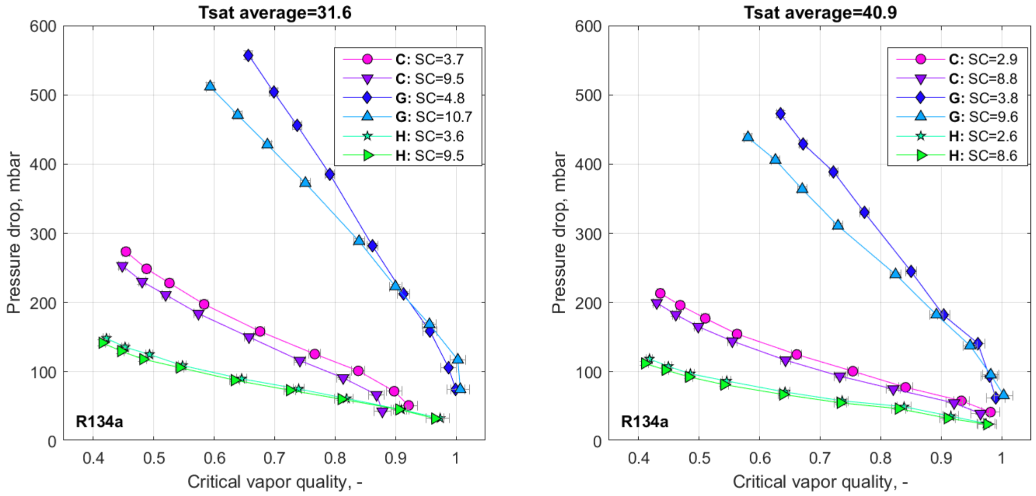

(a) **(b)**

Fig. 40. Pressure drops vs critical vapor quality with R134a, at saturation temperature (a) 31.6 °C and (b) 40.9 °C. The average subcooling (SC) in K is indicated in each curve corresponding geometry C, H, and G.

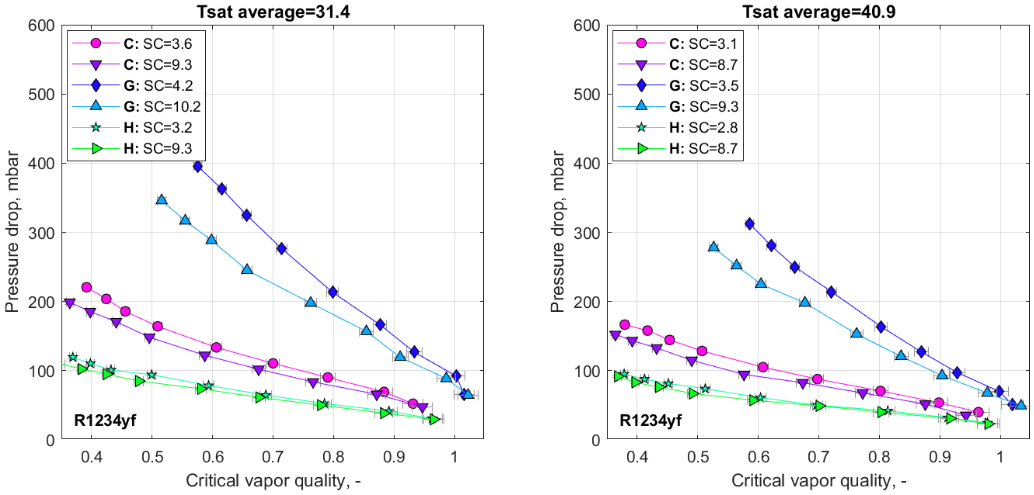

(a) **(b)**

Fig. 41. Pressure drops vs critical vapor quality with R1234yf, at saturation temperature (a) 31.4 °C and (b) 40.9 °C. The average subcooling (SC) in K is indicated in each curve corresponding geometry C, H, and G.

5.4.3. FOOTPRINT CHF AND PRESSURE DROP

The CHF and pressure drop are used to evaluate the geometrical characteristics of geometry G, H, and C, for performance analysis and design considerations. Fig. 42a-b and 43a-b report the footprint CHF vs. pressure drop for the various mass fluxes with R134a and R1234yf, respectively. As mentioned in section 5.4.1., the lowest pressure drop for a given footprint CHF is obtained with geometry H (especially with high inlet subcooling). The footprint CHF with geometry C is 6% – 3 % higher compared with geometry H with R134 and R1234yf, respectively, but the pressure drop increases 79% – 81%. In general, the CHF and pressure drop with R1234yf is lower compared to R135a. In terms of saturation temperature, the increase in saturation temperature from 30 °C to 40 °C with geometry H slightly reduces the CHF (>7%) with both working fluids, but the pressure drop reduces by around 16%. If the system is to reduce the pressure drop, geometry H obtains the lowest result at high inlet subcooling, and high saturation temperature with R1234yf, as shown in Fig. 43b.

As mentioned in Section 5.4.1., the highest CHF is obtained with geometry G. Comparing the geometry G and H, the footprint CHF with geometry G increases by 37% and 29% with R134a and R1234yf, respectively, but the pressure drop increases by a remarkable 262% and 216%. At constant CHF, geometry C performs similarly to geometry G in the range of (300-600) W/cm^2, but the mass flux required to achieve the same CHF with Geometry C increases by around 66%. If the system is to work at the highest CHF (heat recovery is crucial) regardless of the pressure drop, geometry G obtains the highest result at high inlet subcooling, and low saturation temperature with R134a, as shown in Fig. 42a.

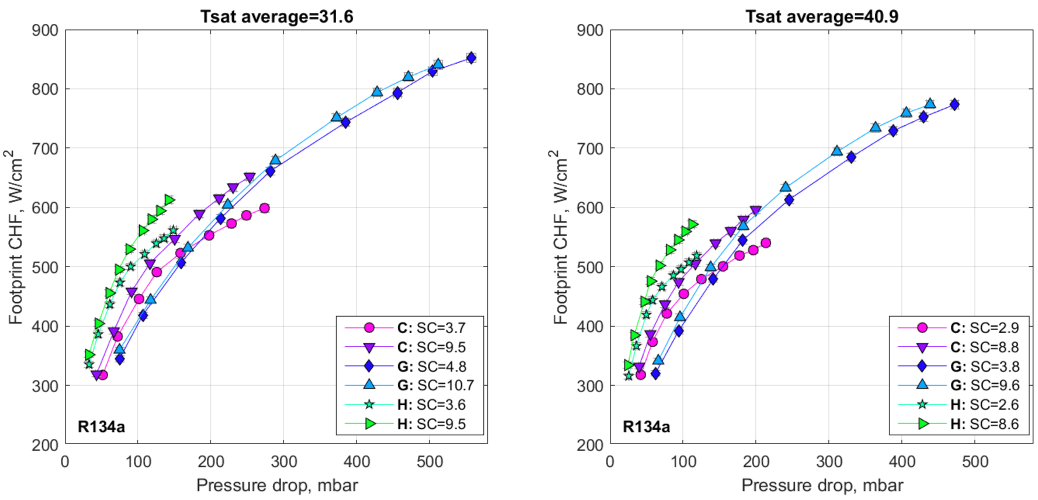

(a) **(b)**

Fig. 42. Footprint CHF vs. pressure drop for R134a at 30°C(a) and at 40°C (b). The average subcooling (SC) in K indicated for each curve with respect to geometry C, H, and G.

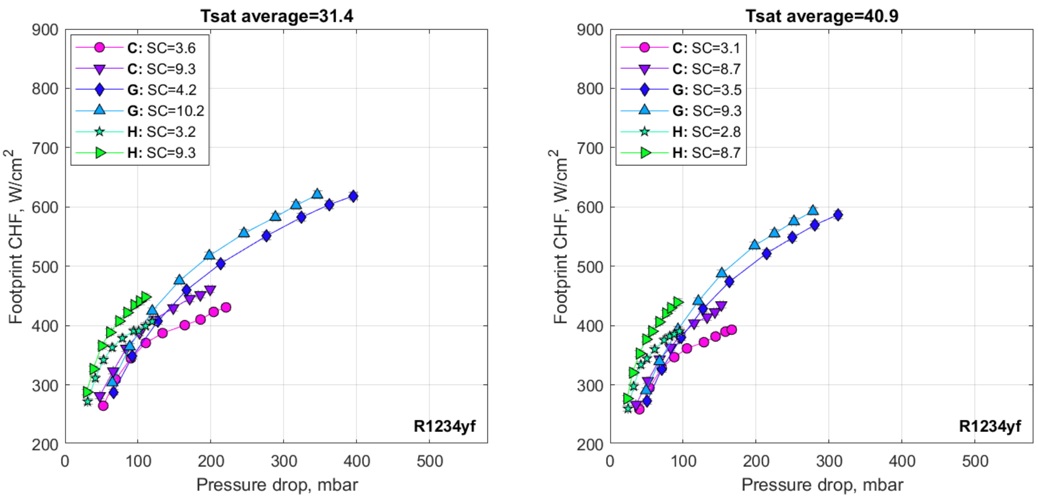

(a) **(b)**

Fig. 43. Footprint CHF vs. pressure drop for R1234yf at 30°C(a) and at 40°C (b). The average subcooling (SC) in K indicated for each curve with respect to geometry C, H, and G.

5.4.4. DISCUSSION

The increase of pressure drops with mass flux and its decrease with critical vapor quality shown in Fig. 38 – 41 are in line with the experimental results of Agostini et al. [2], who observed the total pressure drop increases approximately linearly with the outlet vapor quality and increases with mass velocity in microchannels. This is explained because the growth of footprint CHF increases the dominance of the vapor phase in the two-phase flow causing a higher pressure drop. In all the test conditions, the lowest pressure drop was always obtained with geometry H. As shown in Fig. 38 and 39, at constant mass flux the pressure drop with the diverging channels was especially smaller compared to geometry C at high mass fluxes. A study performed by Balasubramanian and Lee et al. [4] found that the pressure drop in expanding channels was significantly lower especially at higher heat fluxes compared to channels, obtaining a reduction of up to 30%. Here, the same result is visualized in Fig. 42 and 43, where the difference between geometry C and H In terms of pressure drop increases with increasing footprint CHF. Lee attributed the significant reduction in pressure drop to the increase in width of the channel downstream, which decelerates the vapor flow and reduces the pressure drop. Another coupled effect to the decrease of the wall thickness is proposed by Singh [42], who demonstrated that under the same hydraulic diameter, the pressure drop reduces with a reduction in the aspect ratio. Since the aspect ratio at the outlet of geometry H is smaller, the bubbles produced in the diverging microchannel might pass the channel smoothly explaining the reduction as well in the pressure drop. In the case of geometry G, the pressure drop is the highest with sinusoidal channels. The results are expected due to the high CHF obtained, as shown in section 5.1.1, and the intrinsic effect of the corrugated wall. The steep increase in pressure drop with geometry G is aligned with the findings of Xia et al. [51], that observed the two-phase pressure drop increases sharply with an increase of effective heat flux and vapor quality on his sinusoidal wavy microchannels under the dual effect of increasing vapor acceleration and two-phase frictional pressure drop.

In terms of saturation temperature, the lower pressure drop obtained with a saturation temperature of 30 °C compared to 40 °C is expected. Agostini et al. [2] explained that the pressure drop along the channels depends on the fluid properties, finding that it decreases with increasing saturation temperature since the vapor density increases with saturation pressure and temperature. As expected, they found that the two-phase pressure drop was higher with R245fa than R236fa due to its lower vapor density. Certainly, the difference in vapor density between the two working fluids in the present study aligns correctly with their conclusion. As shown in Table 5.6, at a saturation temperature of 30 °C the vapor density of R134a is 39.3 kg/m^3, while for R1234yf is 45.5 kg/m^3. Consequently, the pressure drop with R1234yf compared to R134a, reduces 46% with geometry G, 40% with geometry H, and 36% with geometry C.

The pressure drop measured by the inlet and outlet manifold transducers includes the single-phase pressure drop of the subcooled liquid at the inlet plenum, the two-phase pressure drop along the channels, and the pressure drop at the outlet manifold. Agostini et al. [2] presented an analysis of the relative importance of the liquid, two-phase, and outlet pressure drops. The same analysis brings interesting information about the pressure drop in the different geometries studied. The normalized pressure drop versus critical vapor quality at saturation of temperature 30 °C with R134a and R1234yf is shown in Fig. 44 and 45. As described in section 4.1.5., the pressure drop at the outlet of the channels includes the contribution of the outlet manifold (elbow and two straight sections) and the area change from the channel exit to the outlet plenum, while the inlet pressured drop includes the sudden contraction at the inlet of the microchannels and the inlet plenum (elbow and two straight sections). The normalized outlet pressure drop ω_{out} increases with increasing critical vapor quality, while the normalized inlet pressure drop ω_{in} has the opposite trend. These trends are aligned with Xia et al. [51] results, who explain that at low mass fluxes (vapor quality is high) the amount of vapor generation is larger and becomes a dominant role in the pressure drop compared to the inlet one. At all times, the results show that the main contribution to the total pressure drop comes from channels, meaning that the optimization of the geometry of the channels could play a significant role in decreasing furtherly the pressure drop, as compared to optimizing the inlet and outlet manifolds. The outlet pressure in Fig. 44a becomes even negative at very low critical vapor qualities, this could be explained by the combined effect of the lower amount of vapor generation that reduces the pressure drop in the outlet manifold and the area change from the outlet of the channels to the outlet plenum that expands the flow, recovering pressure.

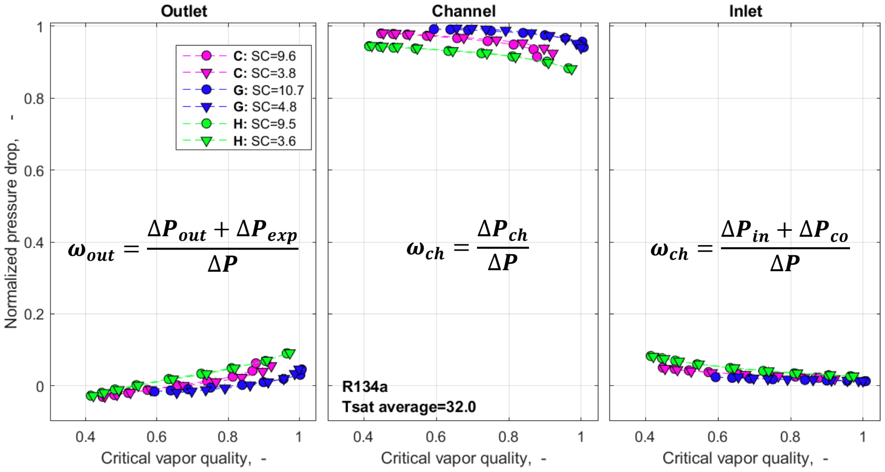

(a) **(b)** **(c)**

Fig. 44. Normalized pressure drops vs. critical vapor quality with R134a at 32 °C saturation temperature at (a) outlet, (b) along the channels, (c) and at the inlet. The average subcooling (SC) in K is indicated in each curve.

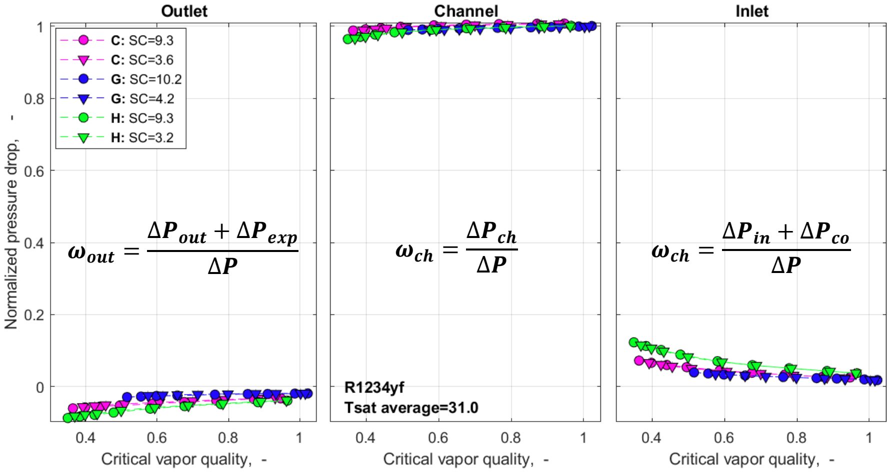

(a) **(b)** **(c)**

Fig. 45. Normalized pressure drops vs. critical vapor quality with R134a at 31 °C saturation temperature at (a) outlet, (b) along the channels, (c) and at the inlet. The average subcooling (SC) in K is indicated in each curve.

As a final remark, as shown in Fig. 42 and 43, geometry H presents the best performance in terms of pressure drop. While if very high heat fluxes are required and heat recovery is critical regardless of the pressure drop, geometry G presents the highest CHF. The comparison between the three geometries, expanding, wavy, and straight channels, can lead to interesting conclusions for the design of heat sinks in engineering applications, i.e., a corrugated wavy microchannel with diverging cross-section, or split systems to reduce the pressure drop while having very high CHF.

5.4.5. SUMMARY

The pressure drop increases with mass flux and decreases with increasing critical vapor quality. The pressure drop with geometry G was the highest, and the lowest with geometry H in all test conditions. The coupled effect of the increasing vapor acceleration and the frictional pressure drop is believed to be the main reason for the steep increase in pressure drop with geometry G, while the increase in width of the channels reduces the pressure drop with geometry H. The pressure drop decreases with increasing saturation temperature because of the reduction in the vapor density, and for the same reason, the pressure drop is lower with R1234yf compared to R134a since the vapor density of R134a is lower. Finally, the contribution of the two-phase pressure drop along the channels is always dominant compared to the pressure drop at the inlet and outlet manifold.

6

Data prediction

This chapter presents the comparison of 14 selected correlations for critical heat flux from literature with the experimental database of this investigation. The correlations employed in the comparative analysis are developed for several channel types, and those based on independent experimental data are referred to as “general” correlations, while the remaining regressions were performed with the experimental data from their laboratory. The sections of the chapter are arranged to present the comparative analysis, followed by a discussion of the major findings and a summary. This chapter answers the last research question from the investigation.

- Question 4: What are the prediction capabilities of existing literature correlations on the critical heat flux CHF in microchannels?

6.1. Methods

The correlations found in the literature cover different channel types implying different considerations made in the calculation of the predicted CHF. Several correlations were developed under the uniform heating condition of single circular tubes. However, as shown in Section 4.1.4., the data reduction in this investigation considers the fin model with an adiabatic tip. Therefore, when not expressly indicated by the authors, to account for the asymmetric heating on the channels, which occurs only on three sides of the rectangular channels, the heated hydraulic diameter D_{he} was employed, defined as:

$$D_{he} = \frac{4.W_{ch}.H_{ch}}{2.H_{ch} + W_{ch}} \tag{43}$$

to replace the reference diameter D for the equivalent heated diameter D_{he} of a rectangular multi-microchannel heated at the bottom. For the statistical analysis, the mean absolute error (MAE) for the correlations was calculated by

$$e_i = \frac{q_{measured} - q_{corr}}{q_{measured}} \tag{44}$$

$$MAE = \frac{1}{n}\sum_{i=1}^{n} |e_i|.100 \tag{45}$$

where q_w is the measured wall CHF, q_{corr} is the CHF predicted by the correlation, and n the number of total experimental points in the investigation (216). The result of the comparison of the experimental results with the selected correlations is presented in Table 6.8. The best predictions are underlined. The table indicates the mean absolute error (MAE), ±20% and ±30% data point coverages, and important remarks on the channel type, heated equivalent diameter, and fluids used to develop the correlations.

6.2. Comparison with literature correlations

Fig. 46 presents the measured CHF compared with the 14 selected correlations from the literature. The best prediction method is obtained by Wu et al. [50] with a coverage of 100% within the ±30% error band and MAE = 8.3%, and Kærn et al. [19]. With 92% coverage and MAE = 10.7%. As a first conclusion, none of the remaining correlations can accurately predict the database from this investigation. This is especially true for the experimental data for the sinusoidal wavy test sample (geometry G) where most correlations underpredict the wall CHF. This is expected since all the selected correlations do not account for the enhanced area and delayed CHF achieved by corrugated fin walls.

However, an important point to consider when using the selected prediction methods is the absent subcooling effect caused by long heated lengths. Ong and Thome's [31] prediction was not accurate with our results, with MAE = 42.7%. However, their correlation was obtained by fitting their data for their circular tubes with a heated length above the test current samples (+180 mm), data by Wojtan (circular tubes), and the data by Park and Thome [32] (rectangular multi-channels). The last, Park and Thome data was calculated employing the fin model, identically as in section 4.1.4., but found no inlet subcooling effect, which later Mauro demonstrated was due to the larger heated length. Indeed, the correlation underpredicts the results measured, probably because of the subcooling that increases the measured CHF, and the correlation could be better aligned if the prediction is shifted upwards.

Another important point to consider is the saturation temperature and pressure in which the correlations were developed. Wojtan et al. [49] prediction resulted in MAE = 28.4%. Their correlation was developed for circular tubes with a larger heated length (20-70 mm) compared to this study, and it was shown by Agostini to predict silicon multi-microchannels accurately. However, because of the lack of experimental data for higher reduced pressures, Wojtan suggested limiting the use of this correlation to ρ_v/ρ_l within the range of 0.009 to 0.0426. Effectively, in this case, the reduced pressure was higher for most of the database and similarly, Wojtan did not account for the subcooling effect on his correlation, probably due to their larger heated length. These two combined effects could explain the underprediction obtained.

Katto and Ohno's correlation [22] is one of the most widely quoted among other authors, and their prediction was relatively well aligned with the results but underpredicting overall, resulting in MAE = 28.6%. In a recent study, Kærn et al. [19] found similar results to the prediction by Katto and Ohno, suggesting the discrepancy was due to the subcooling effect that was not accounted for. Later, they proposed a modified Katto and Ohno correlation to account for the subcooling effect. In fact, the correlation proposed by Kærn provides one of the best predictions with MAE = 10.7%. This is not surprising since the correlation was specifically developed with a database from the same laboratory.

Another point found during this study was the definition of the CHF at the wall of channels that are not uniformly heated. Wu et al. [50] correlation gave the best prediction. Their regression employed their own results from water and Bower and Mudawar [6] data in R-113, alleging the drastic fluid property differences and different geometry made their correlation suitable for multiple cases. However, the calculation of the wall heat flux q_w used in their regression did not consider the fin efficiency, thus, ignoring the conduction effect and assuming the fin has a uniform temperature in its entire length which is not true [38]. Coincidentally, even if the correlation by Wu et al. accurately predicts the data with MAE = 8.9%, it is important to indicate the different data regression of the wall CHF and the unaccounted subcooling effect.

As a final observation, most of the correlations do not account for the effect of a large aspect ratio, where the liquid film behaves differently in the sharp edges and affects the CHF [38].

6.3. Discussion

The use of the correlations for CHF brings several considerations to make since the heat flux which is measured at the base of the heat sink is different from the wall heat flux determined by the correlations. During the study of the predictive methods available, several arbitrary decisions were found. For instance, earlier investigations employed circular tubes, thus, the correlations were developed under the uniform heating condition. However, in this case, the reference diameter of circular tubes had to be replaced by the equivalent heated diameter D_{he} of a rectangular multi-microchannel heated at the bottom, but this is not always the case. Revellin and

Thome [37] employed the width of their rectangular channels as the characteristic diameter of the model in some correlations claiming that it better accounted for the confinement effect of the flow. Later, Revellin et al. [38] would employ the equivalent diameter D_{he} in correlations for uniformly heated circular tubes. However, Qu and Mudawar [36] employed an equivalent diameter in correlations for CHF but did not consider the correction with the fin efficiency η for the measured heat flux, meaning that the conduction effect was ignored assuming infinite conduction, which according to Revellin [38] it is not correct. The selection between the previous method significantly influences the results of the comparison, consequently, exhibiting the importance to calculate accurately the wall heat flux and considering the right characteristic diameter in the earlier correlations. Here, an arbitrary selection had to be made to use the equivalent diameter D_{he} and the wall heat flux accounting for the conduction effect of the fin since it is believed that the use of the average CHF q_{ave}, which differ from the wall CHF q_w by not considering the fin efficiency, leads to significant underprediction of results in most correlations.

6.4. Summary

A comparative analysis of 14 selected correlations was performed. The best predictions were found by Wu et al. [50] with a coverage of 100% and within the ±30% error band, and MAE = 8.3%. The second-best prediction was obtained by Kærn et al. [19]. With MAE = 10.7% and a 92% coverage. The remaining correlations did not predict accurately the experimental results in this investigation. Additionally, several arbitrary decisions and considerations were found when using the available correlations in the literature.

Table 6.8. Prediction statistic of selected correlations for CHF.

Correlation	MAE [%]	**Coverage** [%]		**Remarks**:		
		±20%	±30%	Channel type	D_{he} [mm]	FLuids
Anwar et al. [3]	22.4	32.4	62.5	single circular channels	0.64 – 1.7	refrigerants incl. hydrocarbons
Mikielewicz et al. [30]	30.1	50.46	63.0	single circular channels	1.15 – 2.3	R134a, R1234, ses 32, ethanol
Wojtan et al. [49]	28.4	21.3	63.0	single circular channels	0.5 – 0.8	R134a, R245fa
Ong and Thome [31]	42.7	4.6	13.0	single circular channels and multi rectangular channels	0.35 – 0.88	R134a, R236fa, R245fa
Bowers and Mudawar [6]	17.5	61.1	77.3	multi rectangular channels	2.54 – 0.51	R113
Koşar and Peles [24]	81.2	0	7.4	multi rectangular channels	0.29	R123
Tibiriçá et al. [45]	49.5	0	0	general single circular channels	0.24 – 6.92	water, refrigerants, nitrogen
Kandlikar [53]	54.6	5.1	17.1	general microchannels	0.1 – 3	water, refrigerants
Kumar and Kadam [25]	17.4	61.6	84.2	general microchannels	0.24 – 1.6	R123, R134a, R245fa, R236fa
Wu et al. [50]	8.3	97.2	100	general microchannels	0.22 – 2.98	water, refrigerants, nitrogen
Katto and Ohno [22]	28.6	26.4	55.1	general conventional microchannels		water, refrigerants, nitrogen
Shah [40]	52.4	0	0	general conventional microchannels		water, refrigerants, nitrogen, chemicals, liquid metals
Zhang [52]	40.9	0	37.0	general circular channels	0.33 – 6.22	Water
Kærn [19]	10.7	76.9	92.1	multi rectangular channels	0.36 – 0.52	R134a, R1234yf, R1234ze(E)

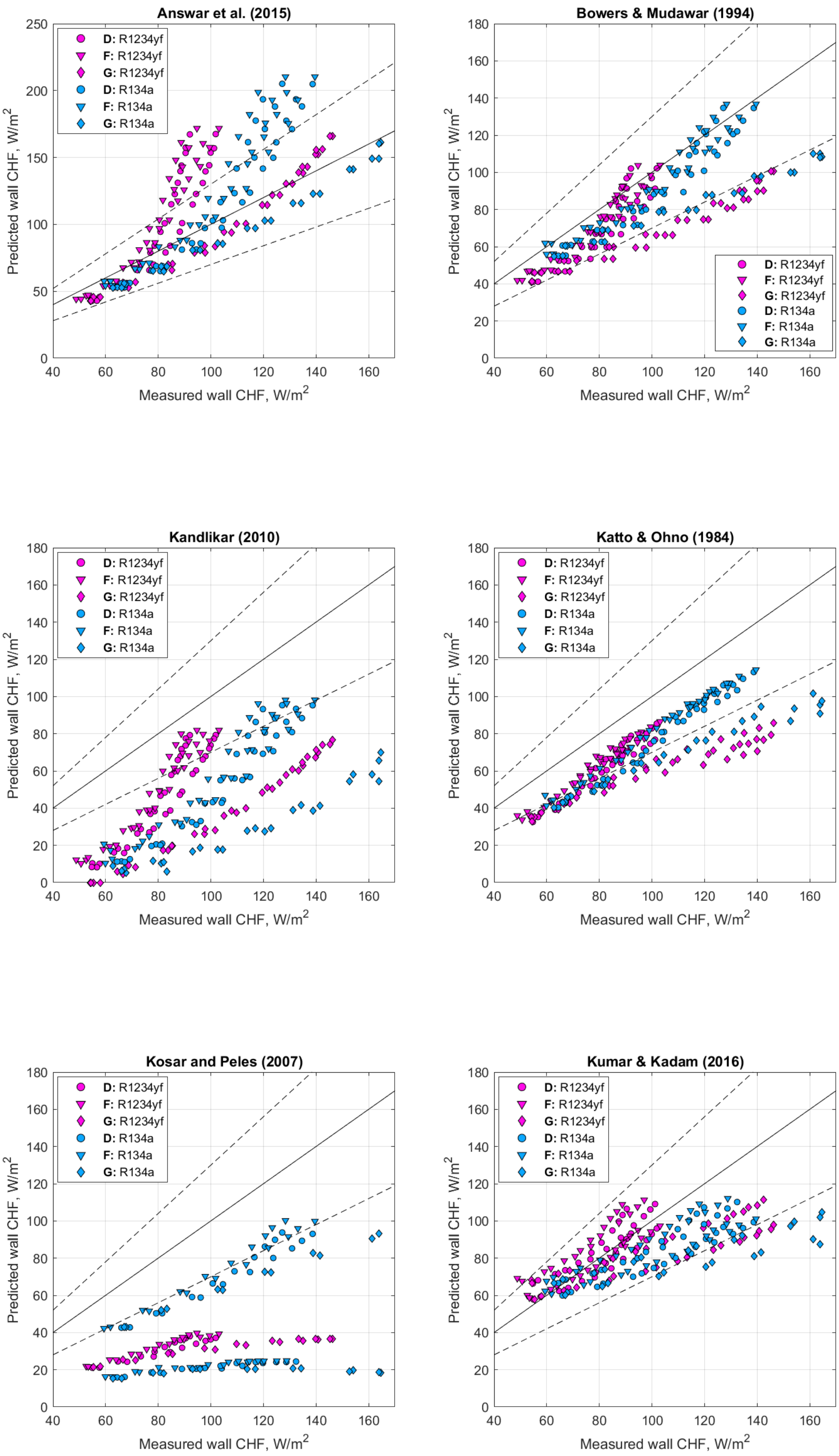

Fig. 46. Parity plot of selected correlations for CHF vs. the measured wall CHF values.

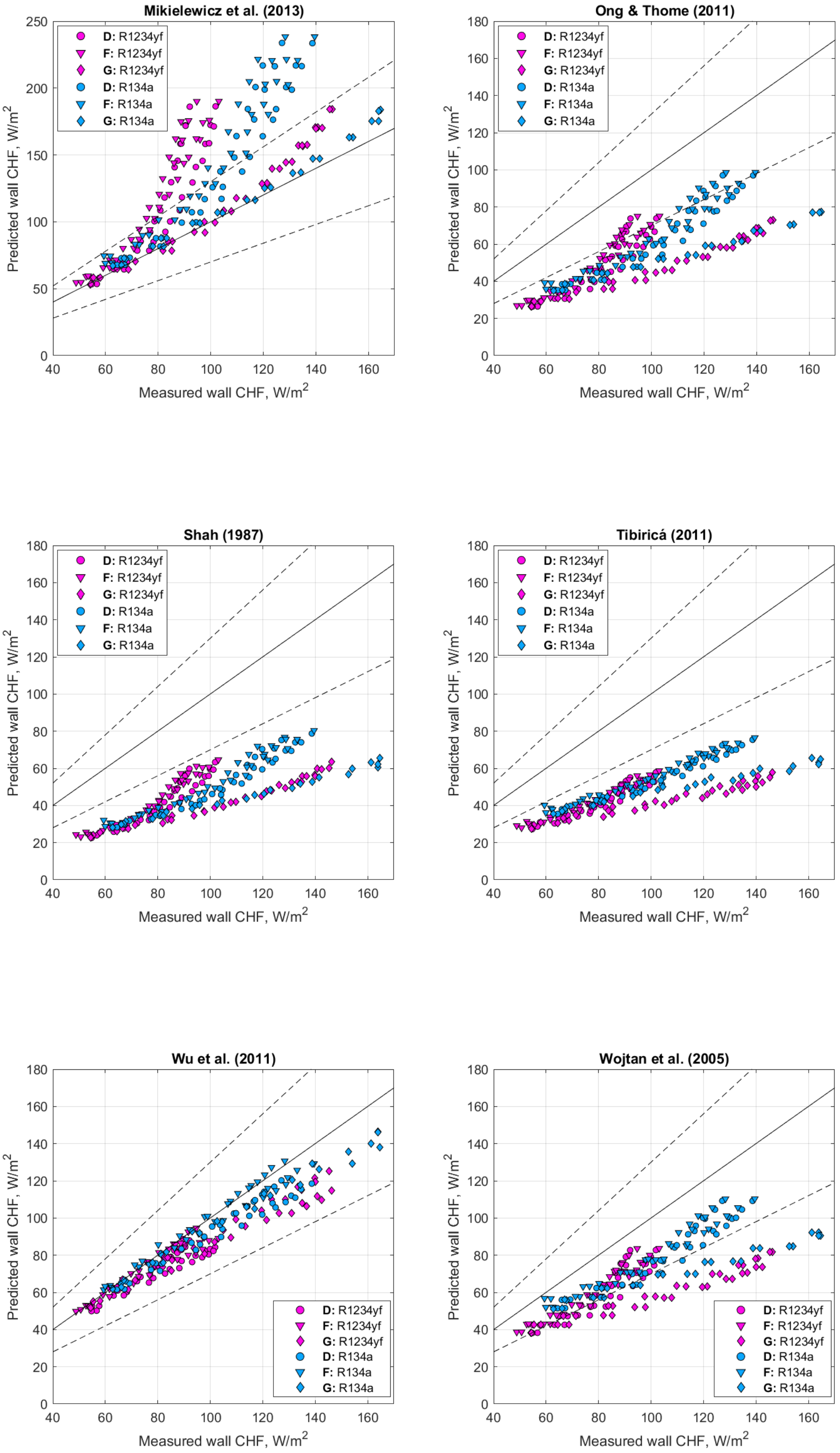

Fig. 46. Continued

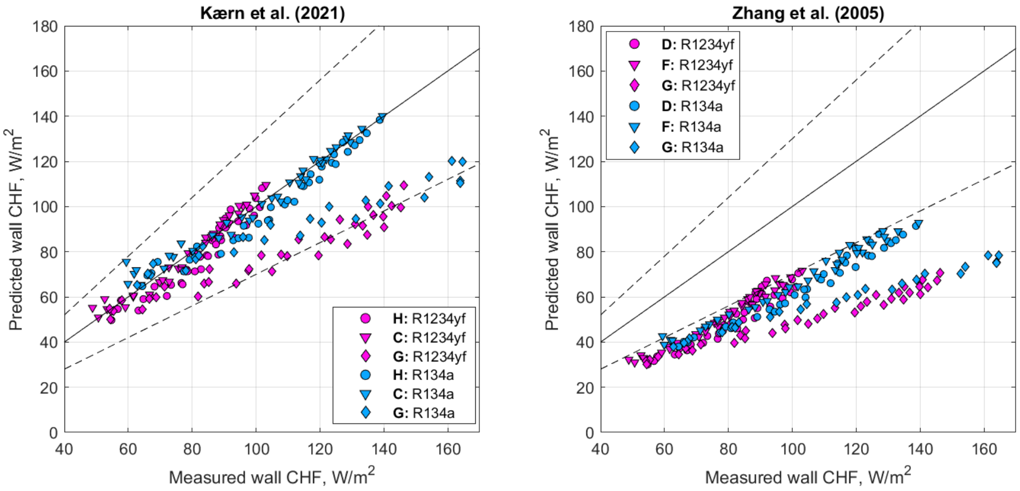

Fig. 46. Continued

7

Concluding Remarks

The present thesis aimed to contribute to the general discussion on CHF in microchannels and the endeavor to develop comprehensive characterizations of the effects of the main parameters of interest. Particularly, the study was oriented to demonstrate that CHF in narrow channels can achieve high CHF, and alternative wall geometries can delay the CHF or decrease the pressure drop. The investigation adopted a low-GWP fluid (R1234yf) and the conventional R134a. Three different microchannels test samples were manufactured in copper and the measurements were taken under a wide range of mass flux between 320 kg/m^{2}s to 1200 kg/m^{2}s, at different subcooling, and the saturation temperature was 30 °C and 40 °C.

7.1. CONCLUSIONS

The conclusions from the results within the range of mass and heat flux tested can be drawn as follows. The effect of the main parameters on the footprint CHF was analyzed with the experimental data. Accordingly, it was shown that:

- The highest CHF in the experimental investigation was obtained was 852.1 W/cm^2 at the highest mass flux with the sinusoidal wavy channels, while the footprint CHF with the straight and diverging channels show similar results, with a value of 652 W/cm^2 and 612.6 W/cm^2, respectively. In general, the CHF in wavy sidewall was consistently higher than with the other test samples. The CHF with the expanding channels was higher than the conventional straight channels at low mass fluxes, but at high mass fluxes, their results were comparable.
- The effect of inlet restriction to minimize the flow instability revealed a positive effect for the straight channels, but for the other test samples, different trends

were found. Generally, the CHF increased when no inlet restrictions were used with the wavy and expanding channels. However, the increase becomes negligible or even absent at high subcooling and high mass fluxes.
- The CHF significantly increases with an increase in the mass flux according to literature. Inconsistencies are found in the effect of subcooling which is evident in the straight and the diverging channel design with CHF increasing with increasing subcooling, while the effect was negligible in the sinusoidal wavy. The latter was attributed to high mixing and secondary flows that quickly mix the incoming liquid. For both working fluids, the saturation temperature systematically reduces the CHF with the three test samples, and the effect is slightly more prominent with R1234yf due to its different reduced pressure. Finally, the CHF achieved with R134a was higher in all test conditions due to its higher latent heat of vaporization.

The experimental data were analyzed at the channel level since it reflects the effective heat flux dissipated on the wetted perimeter of the microchannels. It is believed that:

- The wall CHF obtained with the diverging channels was higher than the straight channel, especially at low mass fluxes. The higher CHF is attributed to the smaller hydraulic diameter, which is consistent with several correlations that expect an increase in the wall CHF with diameter. Moreover, the pressure gradient at the inlet could help to stabilize the two-phase flow inside the channels resulting in a delay in the CHF. Additionally, the coupled effect of different aspect ratios could play a role in the wall CHF increase revealed in the experimental results.
- The wall CHF with the sinusoidal wavy sample was consistently the highest among the three test samples at all test conditions. The significant increase in the wall CHF with geometry G is believed to be a combination of the area enhancement, and the coupled effect of the continuous developing liquid film layer and stored liquid in the corner regions caused by the corrugated wall, preventing the dry-out and increasing the CHF. It is believed that the last two effects are the main ones responsible to sustain the annular flow, although high-speed image observations could not confirm this hypothesis.

The analysis of the relationship between the wall CHF and the critical vapor quality instigated important findings. The results showed that:

- The critical vapor quality decreases with increasing wall CHF. It is believed that high mass fluxes (corresponding to the high wall CHF) could tear the liquid film in the annular flow resulting in CHF with a lower critical vapor quality, as stated by Qi [35]. High-speed images determined the dominance of annular flow at the outlet of the channels making the above a reasonable conclusion.
- The highest critical vapor quality corresponds to the sinusoidal wavy channels in all test conditions. This was attributed to the mentioned effects of the corrugated walls that allow high wall CHF. On the other hand, the critical vapor

quality with the diverging design is comparable to or slightly higher than with the conventional straight channels. The slightly higher critical vapor quality achieved with the diverging design is believed to be the result of the increasing width of the channels that decelerates the two-phase flow enhancing the vapor production and delaying the annular-to-dry-out transition.
- Finally, the different critical vapor qualities with R1234a and R134a are explained by the different latent heat of vaporization, and the wall CHF at a given mass flux.

The investigation was extended to the pressure drop analysis between the test samples. Although pressure drop was not the main scope of the investigation, the analysis in the thesis presents practical considerations for the design of multi-microchannels heat sinks operating in flow boiling.

- pressure drop increases with mass flux and decreases with increasing critical vapor quality according to literature. The pressure drop is the highest with the sinusoidal wavy channels. This was attributed to the coupled effect of the increasing vapor acceleration, and the frictional pressure drop. The lowest pressure drop in all test conditions was obtained with the expanding design, explained by the increase in width of the channels.
- The pressure drop decreases with increasing saturation temperature because the vapor density reduces with higher saturation temperature and saturation pressure. Therefore, the lowest values were obtained with R1234yf. Finally, the contribution of the two-phase pressure drop along the channels is always dominant compared to the pressure drop at the inlet and outlet manifold.

Finally, the comparison of current prediction methods found several considerations and arbitrary decisions to make while employing earlier correlations. The best prediction was found by Wu et al. [50] and Kærn et al. [19]. The remaining predictive methods available did not accurately predict the current results.

7.2. RECOMMENDATIONS FOR FURTHER WORK

The results of the investigation introduce several features in which further and deeper analysis is required to consolidate comprehensive characterizations of the effects of main parameters of interest on CHF. The development of new correlations that account for alternative wall geometries is required to improve the prediction methods in new multi-microchannels alternatives like sinusoidal wavy and diverging designs. Multi-channel setups with alternative sidewall geometry present a variety of phenomena that are difficult to segregate in experiments. Therefore, detailed numerical models could be coupled to the description of the CHF mechanism in alternative geometries. On the other hand, only a patient collection of experimental data for the step-by-step creation of an extensive database of measured CHF data could effectively improve the prediction of future correlations.

More studies regarding observations of flow pattern in sinusoidal wavy directly concerning CHF is required since the delay on dry-out is exclusively related to the replenishment of the liquid layer enhanced by the corrugated wall. Studies regarding two-phase boiling were developed to a certain extent, however, investigations concerning the CHF and flow patterns are currently inexistent.

Additionally, validation and possible refinement in the effect of main parameters are still needed. For instance, a wide range saturation temperature test with R134a and R1234yf could consolidate the existence of a CHF peak and generalize its effect based on the reduced pressure. Experiments run at very high mass flux are needed to verify the experimental trends of CHF with multi-microchannels and validate whether the CHF has an asymptotic behavior. This is remarkably important for diverging channels, which could represent a promising solution if they can achieve high CHF at very high mass fluxes while still presenting a low pressure drop.

Finally, it is interesting to investigate which additional solutions could enhance the heat transfer while keeping limited pressure drops concerning CHF. Although some literature regarding innovative solutions was carried out to a certain extent, investigation of CHF with diverging-sinusoidal wavy, or diverging channels with split systems could present significant conclusions for engineering applications in cooling systems.

Bibliography

[1] Larsen, L. (2021). *Experimental investigation on two-phase cooling of power electronics.* DTU Department of Mechanical Engineering. Retrieved from https://findit.dtu.dk/en/catalog/60fd46add9001d01622e8d97

[2] Agostini, B., Revellin, R., Thome, J., Fabbri, M., Michel, B., Calmi, D., & Kloter, U. (2008). High heat flux flow boiling in silicon multi-microchannels--Part III: Saturated critical heat flux of R236fa and two-phase pressure drops. *International Journal of Heat and Mass Transfer, 51*(21-22), 5426--5442. doi:https://doi.org/10.1016/j.ijheatmasstransfer.2008.03.005

[3] Anwar, Z., Palm, B., & Khodabandeh, R. (2015). Dryout characteristics of natural and synthetic refrigerants in single vertical mini-channels. *Experimental Thermal and Fluid Science, 68*, 257--267. doi:https://doi.org/10.1016/j.expthermflusci.2015.04.016

[4] Balasubramanian, K., Lee, P., Jin, L., Chou, S., Teo, C., & Gao, S. (2011). Experimental investigations of flow boiling heat transfer and pressure drop in straight and expanding microchannels--a comparative study. *International Journal of Thermal Sciences, 50*(12), 2413--2421. doi:https://doi.org/10.1016/j.ijthermalsci.2011.07.007

[5] Bergles, A., & Kandlikar, S. (2005). On the nature of critical heat flux in microchannels. *J. Heat Transfer, 127*(1), 101--107. doi:https://doi.org/10.1115/1.1839587

[6] Bowers, M., & Mudawar, I. (1994). High flux boiling in low flow rate, low pressure drop mini-channel and micro-channel heat sinks. *International Journal of Heat and Mass Transfer, 37*(2), 321--332. doi:https://doi.org/10.1016/0017-9310(94)90103-1

[7] Chalfi, T., & Ghiaasiaan, S. (2008). Pressure drop caused by flow area changes in capillaries under low flow conditions. *International Journal of Multiphase Flow, 34*(1), 2--12. doi:https://doi.org/10.1016/j.ijmultiphaseflow.2007.09.004

[8] Chen, T., & Garimella, S. (2012). A study of critical heat flux during flow boiling in microchannel heat sinks. *Journal of heat transfer, 134*(1). doi:https://doi.org/10.1115/1.4004715

[9] Choi, C., Yu, D., & Kim, M. (2011). Adiabatic two-phase flow in rectangular microchannels with different aspect ratios: Part I--Flow pattern, pressure drop and void fraction. *International Journal of Heat and Mass Transfer, 54*(1-3), 616--624. doi: https://doi.org/10.1016/j.ijheatmasstransfer.2010.07.067

[10] Criscuolo, G. (2021). Two-phase cooling of power electronics: An investigation on flow boiling of refrigerants in narrow channels. DCAMM Special Report(S299), 131. Retrieved from https://orbit.dtu.dk/en/publications/two-phase-cooling-of-power-electronics-an-investigation-on-flow-b

[11] Criscuolo, G., Brix Markusen, W., Meyer, K., Palm, B., & Rhyl, K. (2021). Experimental characterization of the heat transfer in multi-microchannel heat sinks for two-phase cooling of power electronics. *Fluids, 6*(2), 55. doi:https://doi.org/10.3390/fluids6020055

[12] Dalkılıç, A., Celen, A., Erdoğan, M., Sakamatapan, K., Newaz, K., & Wongwises, S. (2020). Effect of saturation temperature and vapor quality on the boiling heat transfer and critical heat flux in a microchannel. *International Communications in Heat and Mass Transfer, 117*, 104768. doi:https://doi.org/10.1016/j.icheatmasstransfer.2020.104768

[13] Describing uncertainties in single-sample experiments. (1953). *ASME Mechanical Engineering, 75*(1), 38. doi: ISSN 19435649, 00256501.

[14] *DFFResearch Project Grants from the Danish Council for Independent Research*. (2017). Retrieved from Danish Ministry of Higher Education and Science: https://ufm.dk/forskning-og-innovation/tilskud-til-forskning-og-innovation/hvem-har-modtaget-tilskud/2017/bevillinger-fra-det-frie-forskningsrad-teknologi-og-produktion-til-dff-forskningsprojekter-1-og-2-maj-2017/

[15] Fan, L., Ciais, P., Bastos, A., Brandt, M., Chave, J., Wigneron, J.-P., . . . Fensholt, R. (2020). Tropical forests did not recover from the strong 2015--2016 El Niño event. *Science advances, 6*(6), eaay4603. doi:https://doi.org/10.1016/j.atmosres.2020.105090

[16] Fu, B., Lee, C., & Pan, C. (2013). The effect of aspect ratio on flow boiling heat transfer of HFE-7100 in a microchannel heat sink. *International journal of heat and mass transfer, 58*(1-2). doi:https://doi.org/10.1016/j.ijheatmasstransfer.2012.11.050

[17] Hong, S., Tang, Y., & Wang, S. (2018). Investigation on critical heat flux of flow boiling in parallel microchannels with large aspect ratio: Experimental and theoretical analysis}. *International Journal of Heat and Mass Transfer, 127*, 55--66. doi: https://doi.org/10.1016/j.ijheatmasstransfer.2018.07.110

[18] (2008). *Joint Comitee for Guides in Metrology. Evaluation of measurement data — Guide to the expression of uncertainty in measurement.* BIPM. Retrieved from http://www.bipm.org/en/publications/guides/gum.html

[19] Kærn, M., Criscuolo, G., Meyer, K., & Markussen, W. (2021). Critical heat flux characteristics of R1234yf, R1234ze (E) and R134a during saturated flow boiling in narrow high aspect ratio microchannels. *International Journal of Heat and Mass Transfer, 180*, 121840. doi:https://doi.org/10.1016/j.ijheatmasstransfer.2021.121840

[20] Kuan, W. K., & Kandlikar, S. G. (2006). Critical heat flux measurement and model for refrigerant-123 under stabilized flow conditions in microchannels. *International Mechanical Engineering Congress and Exposition, 47845*, 285--295. doi: https://doi.org/10.1115/IMECE2006-13310

[21] Karayiannis, T., & Mahmoud, M. (2017). Flow boiling in microchannels: Fundamentals and applications. *Applied Thermal Engineering, 115*, 1372--1397. doi:https://doi.org/10.1016/j.applthermaleng.2016.08.063

[22] Katto, Y., & Ohno, H. (1984). An improved version of the generalized correlation of critical heat flux for the forced convective boiling in uniformly heated vertical tubes. *International journal of heat and mass transfer, 27*(9), 1641--1648. doi:https://doi.org/10.1016/0017-9310(84)90276-X

[23] Kim, S.-M., & Mudawar, I. (2017). Thermal design and operational limits of two-phase micro-channel heat sinks. *International Journal of Heat and Mass Transfer, 106*, 861--876. doi:https://doi.org/10.1016/j.ijheatmasstransfer.2016.10.020

[24] Koşar, A., & Peles, Y. (2007). Critical heat flux of R-123 in silicon-based microchannels. *Journal of Heat Transfer*. doi:https://doi.org/10.1115/1.2712852

[25] Kumar, R., & Kadam, S. (2016). Development of new critical heat flux correlation for microchannel using energy-based bubble growth model. *Journal of Heat Transfer, 138*(6). doi:https://doi.org/10.1115/1.4032148

[26] Lee, J., & Mudawar, I. (2009). Critical heat flux for subcooled flow boiling in micro-channel heat sinks. *International Journal of Heat and Mass Transfer, 52*(13-14), 3341--3352. doi:https://doi.org/10.1016/j.ijheatmasstransfer.2008.12.019

[27] Martin, H. (1996). A theoretical approach to predict the performance of chevron-type plate heat exchangers. *Chemical Engineering and Processing: Process Intensification, 35*(4), 301--310. doi:https://doi.org/10.1016/0255-2701(95)04129-X

[28] Mastrullo, R., Mauro, A., & Viscito, L. (2017). Experimental CHF for low-GWP fluids and R134a. Effect of the Lh/D ratio at low and high mass velocities. *International Journal of Heat and Mass Transfer, 109*, 1200--1216. doi:https://doi.org/10.1016/j.ijheatmasstransfer.2017.02.071

[29] Mauro, A., Thome, J., Toto, D., & Vanoli, G. (2010). Saturated critical heat flux in a multi-microchannel heat sink fed by a split flow system. *Experimental Thermal and Fluid Science, 34*(1), 81--92. doi:https://doi.org/10.1016/j.expthermflusci.2009.09.005

[30] Mikielewicz, D., Wajs, J., Gliński, M., & Zrooga, A.-B. (2013). Experimental investigation of dryout of SES 36, R134a, R123 and ethanol in vertical small diameter tubes. *Experimental thermal and fluid science, 44*, 556--564. doi:https://doi.org/10.1016/j.expthermflusci.2012.08.018

[31] Ong, C., & Thome, J. (2011). Macro-to-microchannel transition in two-phase flow: Part 2--Flow boiling heat transfer and critical heat flux. *Experimental thermal and fluid science, 35*(6), 873--886. doi:https://doi.org/10.1016/j.expthermflusci.2010.12.003

[32] Park, J., & Thome, J. (2010). Critical heat flux in multi-microchannel copper elements with low pressure refrigerants. *International Journal of Heat and Mass Transfer, 53*(1-3), 110--122. doi:https://doi.org/10.1016/j.ijheatmasstransfer.2009.09.047

[33] Prajapati, Y., Pathak, M., & Khan, M. (2015). A comparative study of flow boiling heat transfer in three different configurations of microchannels. *International Journal of Heat and Mass Transfer, 85*, 711--722. doi:https://doi.org/10.1016/j.ijheatmasstransfer.2015.02.016

[34] Pribyl, D., Bar-Cohen, A., & Bergles, A. (2003). An investigation of critical heat flux and two-phase flow regimes for upward steam and water flow. In *Proceedings of the Fifth International Conference on Boiling Heat Transfer.*

[35] Qi, S., Zhang, P., Wang, R., & Xu, L. (2007). Flow boiling of liquid nitrogen in micro-tubes: Part II--Heat transfer characteristics and critical heat flux. *International journal of heat and mass transfer, 50*(25-26), 5017--5030. doi:https://doi.org/10.1016/j.ijheatmasstransfer.2007.08.017

[36] Qu, W., & Mudawar, I. (2004). Measurement and correlation of critical heat flux in two-phase micro-channel heat sinks. *International Journal of Heat and Mass Transfer, 47*(10-11), 2045--2059. doi:https://doi.org/10.1016/j.ijheatmasstransfer.2003.12.006

[37] Revellin, R., & Thome, J. (2008). A theoretical model for the prediction of the critical heat flux in heated microchannels. *International Journal of Heat and Mass Transfer, 51*(5-6), 1216--1225. doi:https://doi.org/10.1016/j.ijheatmasstransfer.2007.03.002

[38] Revellin, R., Mishima, K., & Thome, J. (2009). Status of prediction methods for critical heat fluxes in mini and microchannels. *International Journal of Heat and Fluid Flow, 30*(5), 983--992. doi:https://doi.org/10.1016/j.ijheatfluidflow.2009.04.006

[39] Rodar, A., & Jensen, M. (2009). A review of the critical heat flux condition in mini-and microchannels. *Journal of Mechanical Science and Technology, 23*(9), 2529--2547. doi:https://doi.org/10.1007/s12206-009-0711-y

[40] Shah, M. (1987). Improved general correlation for critical heat flux during upflow in uniformly heated vertical tubes. *International Journal of Heat and Fluid Flow, 8*(4), 326--335. doi:https://doi.org/10.1016/0142-727X(87)90069-5

[41] Shanks, H., Maycock, P., Sidles, P., & Danielson, G. (1963, Jun). Thermal Conductivity of Silicon from 300 to 1400 K. *Physical Review, 130*(5), 1743--1748. doi:10.1103/PhysRev.130.1743

[42] Singh, S., Kulkarni, A., Duttagupta, S., Puranik, B., & Agrawal, A. (2008). Impact of aspect ratio on flow boiling of water in rectangular microchannels. *Experimental Thermal and Fluid Science, 33*(1), 153--160. doi:https://doi.org/10.1016/j.expthermflusci.2008.07.014

[43] Sui, Y., Lee, P., & Teo, C. (2011). An experimental study of flow friction and heat transfer in wavy microchannels with rectangular cross section. *International journal of thermal sciences, 50*(12), 2473--2482. doi:https://doi.org/10.1016/j.ijthermalsci.2011.06.017

[44] Sui, Y., Teo, C., Lee, P., Chew, T., & Shu, C. (2010). Fluid flow and heat transfer in wavy microchannels. *International Journal of Heat and Mass Transfer, 53*(13-14), 2760--2772. doi:https://doi.org/10.1016/j.ijheatmasstransfer.2010.02.022

[45] Tibirica, C., Czelusniak, L., & Ribatski, G. (2015). Critical heat flux in a 0.38 mm microchannel and actions for suppression of flow boiling instabilities. *Experimental Thermal and Fluid Science, 67*, 48--56. doi:https://doi.org/10.1016/j.expthermflusci.2015.02.020

[46] Wan, Z., Wang, Y., Wang, X., & Tang, Y. (2018). Flow boiling characteristics in microchannels with half-corrugated bottom plates. *International Journal of Heat and Mass Transfer, 116*, 557--568. doi:https://doi.org/10.1016/j.ijheatmasstransfer.2017.09.029

[47] Wang, H.-L., Wu, H.-C., Wang, S., Hung, T.-C., & Yang, R.-J. (2013). A study of mini-channel thermal module design for achieving high stability and high capability in electronic cooling. *Applied thermal engineering, 51*(1-2), 1144--1153. doi:https://doi.org/10.1016/j.applthermaleng.2012.10.007

[48] Wojtan, L., Revellin, R., & Thome, J. (2006). Investigation of saturated critical heat flux in a single, uniformly heated microchannel. *Experimental Thermal and Fluid Science, 30*(8), 765--774. doi:https://doi.org/10.1016/j.expthermflusci.2006.03.006

[49] Wojtan, L., Ursenbacher, T., & Thome, J. (2005). Investigation of flow boiling in horizontal tubes: Part I—A new diabatic two-phase flow pattern map. *International journal of heat and mass transfer, 48*(14), 2955--2969. doi:https://doi.org/10.1016/j.ijheatmasstransfer.2004.12.012

[50] Wu, Z., Li, W., & Ye, S. (2011). Correlations for saturated critical heat flux in microchannels. *54*(1-3), 379--389. doi:https://doi.org/10.1016/j.ijheatmasstransfer.2010.09.033

[51] Xia, G., Tang, Y., Zong, L., Ma, D., Jia, Y., & Rong, R. (2019). Experimental investigation of flow boiling characteristics in microchannels with the sinusoidal wavy sidewall. *International Communications in Heat and Mass Transfer, 101*, 89--102. doi: https://doi.org/10.1016/j.icheatmasstransfer.2019.01.006

[52] Zhang, W., Hibiki, T., Mishima, K., & Mi, Y. (2006). Correlation of critical heat flux for flow boiling of water in mini-channels. *International Journal of Heat and Mass Transfer, 49*(5-6), 1058--1072. doi:https://doi.org/10.1016/j.ijheatmasstransfer.2005.09.004

[53] Kandlikar, S. G. (2010). A scale analysis based theoretical force balance model for critical heat flux (CHF) during saturated flow boiling in microchannels and minichannels. *Journal of heat transfer, 132*(8). doi: https://doi.org/10.1115/1.4001124

List of Figures

List of Tables

Scuola di ingegneria industriale e dell’informazione
Polytechnic of Milan

Piazza Leonardo da Vinci, 32
20133 Milano
P.IVA 04376620151
C.F. 80057930150

https://www.polimi.it

Dipartimento di Energia

Campus Bovisa - Via Lambruschini, 4a - 20156 Milano
Tel. +39 02 2399 3801 – Fax +39 02 2399 3913
PEC pecenergia(at)cert.polimi.it
P.IVA: 04376620151
C.F. 80057930150

https://www.energia.polimi.it

April 2022